# Emerging Materials for Energy Harvesting 11

**Abstract**

Energy harvesting is emerging as a viable method for electronic devices to pull ambient energy from their surrounding environment (e.g., solar power, thermal energy, wind energy, salinity gradients, and kinetic energy, also known as ambient energy) and convert it into electrical energy for stored power. This coveted technology has the potential to serve as an alternative power supply for batteries that are ubiquitous in small, mobile, and autonomous wireless electronic devices, like those used in wearable electronics and wireless sensor networks. The discipline of energy harvesting is a broad topic that includes established methods and materials such as photovoltaics, and thermoelectrics, as well as emerging technologies that convert mechanical energy, magnetic energy, and waste heat to electricity. Innovative materials are vital to the development of all these energy-harvesting technologies. There are several promising micro- and nano-scale energy-harvesting materials (including ceramics, single crystals, polymers, and composites) and technologies currently being developed, such as thermoelectric materials, piezoelectric materials, pyroelectric materials, and magnetic materials. This chapter will review various state-of-the-art materials and enabled devices for direct energy harvesting and conversion, and also highlight the nanostructured materials underlying energy-harvesting principles and devices, in addition to traditional bulk processes and devices as appropriate and synergistic; innovative device-design and fabrication that leads to higher efficiency energy-harvesting or conversion technologies ranging from the cm/mm scale down to MEMS/NEMS (micro- and nano-electromechanical systems) devices; new developments in experimental methods, and device performance measurement techniques.



C. Tong, *Introduction to Materials for Advanced Energy Systems*,
https://doi.org/10.1007/978-3-319-98002-7_11

## 11.1 Generic Energy-Harvesting System

Energy harvesting (also known as power harvesting or energy scavenging or ambient power) is the process by which energy is derived from external sources (e.g., solar power, thermal energy, wind energy, salinity gradients, and kinetic energy, also known as ambient energy), captured, and stored particularly for small, wireless autonomous devices, like those used in wearable electronics and wireless sensor networks. Energy-harvesting devices are usually used to capture small amounts of energy that would otherwise be lost as heat, light, sound, vibration, or movement. The captured energy can be utilized to improve efficiency (e.g., computing costs would be cut significantly if waste heat were harvested and used to help power the computer) and enable new technology (e.g., wireless sensor networks). Energy harvesting also has the potential to replace batteries for small, low-power electronic devices. This has several benefits: (a) Maintenance free—no need to replace batteries; (b) Environmentally friendly—disposal of batteries is tightly regulated because they contain chemicals and metals that are harmful to the environment and hazardous to human health; (c) Opens up new applications—such as deploying energy-harvesting sensors to monitor remote or underwater locations.

All in all, the main purpose of energy harvesting is to transform a present excess energy from the surroundings into a usable form to power a specific application. It is not strictly necessary to produce electricity; a windmill, for example, can be used to convert wind energy into rotational kinetic energy for milling grains or pumping water. The basic function is common to any type of device and involves certain steps that are depicted, for the case where electricity is produced, in the flow chart in Fig. 11.1. The first block is reserved for the ambient source. Vibrations, solar illumination, radio frequency, pressure fluctuations, fluid flows, and thermal gradients can all be used as a starting point. The link between the source and the actual conversion mechanism is represented by the second block. In the case of motion energy harvesting this can be a direct force or an inertial force coupling. Thermal contact would be the link for thermoelectric harvesters. The third block describes the actual principle of transduction being used. This can be any physical principle that transforms a certain form of energy into electricity. A wide range of possibilities are nowadays under investigation, such as motion type harvesters, and piezoelectric, electromagnetic, and electrostatic implementations. The Seebeck effect is the corner stone of thermal harvesting, where temperature gradients are converted into an electric potential and the photovoltaic effect is applicable to light sources of any kind. After transformation into electrical energy, circuitry is needed to extract the generated power from the transducers. It might be necessary to rectify and regulate the output voltage. This is strongly dependent on the used mechanism. A buffer or energy store handles periods of high demand by the load just as well as periods of low supply by the source. These three blocks work together and can be integrated to a certain extent. In other cases, it might not be necessary to include an intermediate energy storage solution. Finally the last link in the chain is the load that consumes the generated power. In a wireless sensor network this could, for example, be a simple temperature sensor with data transmission to a central computer. It

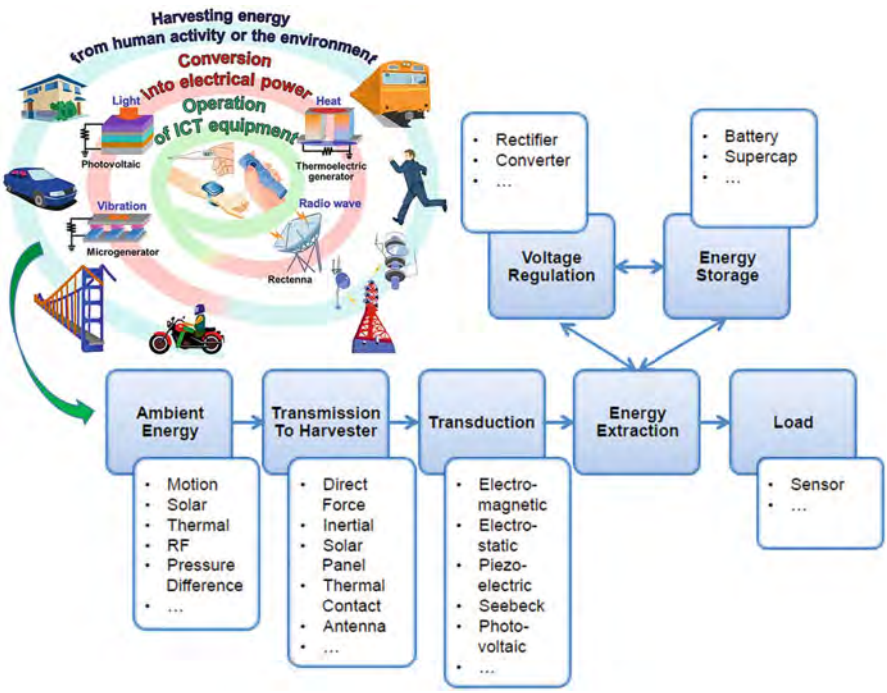


**Fig. 11.1** General operational flow chart for an energy-harvesting system (Modified from Pillatsch (2013). Credit: Imperial College London. Available at https://spiral.imperial.ac.uk/bitstream/10044/1/18112/1/Pillatsch-P-2013-PhD-Thesis.pdf)

should be mentioned that this system constitutes a generic example and that some functionality or blocks can be added and others left out depending on the application. For instance, intermediate energy storage might not always be necessary as for the device, where low-power pulses representing sensor data are transmitted directly. In the case of frequency tuning for resonant vibration harvesters, the electronic system might be more complex and require a feedback loop that acts upon the transduction mechanism in order to adjust to changing operation conditions. Also, it is important not to lose the overview of the entire system when working on one particular building block as each block can be affected by the preceding and following ones. For this reason energy-harvesting platforms can be used to incorporate the entire functionality (Pillatsch 2013).

The need for energy harvesting accompanied with renewable energy, and improved energy efficiency is motivating the discovery of new materials and design of new device structures. For example, nanostructured composite materials are not only promising for thermoelectric, but also in photovoltaics. Nanocomposite materials can enhance the thermal-to-electrical power conversion efficiency. One nanocomposite used is phase change materials (PCM), which were prepared by compositing exfoliated graphite nanoplatelets (xGnP) into paraffin wax. The role of

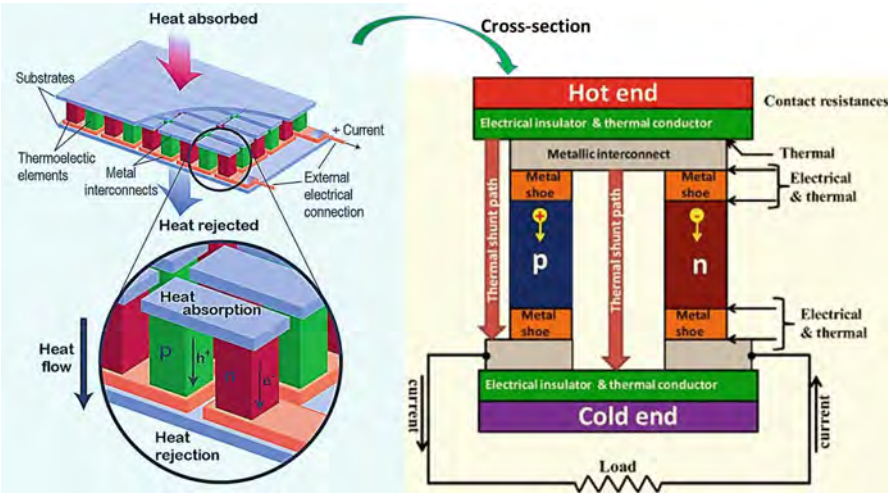


**Fig. 11.2** Thermoelectric module showing the direction of charge flow on both cooling and power generation (Modified with permission from Snyder and Toberer (2008) (Springer Nature), and Aswal et al. (2016) (Elsevier))

new materials in energy harvesting cuts across all of the innovative devices. The need for this enhanced understanding will grow increasingly important as the role of nano-structured materials is enhanced. Energy harvesting covers a cross-cutting discipline. Each of the subfields is important to an understanding of advances across the field as a whole (Radousky and Liang 2012)

## 11.2 Thermoelectric Materials

Thermoelectric (TE) energy converters are of increasing interest as these solid-state devices can transform heat given off from sources such as power plants, factories, motor vehicles, computers, or even human bodies into electric power using the Seebeck effect, as shown in Fig. 11.2 (Snyder and Toberer 2008; Aswal et al. 2016). Thermoelectric system is an environment-friendly energy conversion technology with the advantages of small size, high reliability, no pollutants, and feasibility in a wide temperature range (Zhang and Zhao 2015). Conversely, solid-state thermoelectric devices can also change electrical energy into thermal energy for cooling or heating using the Peltier effect. However, because of their low efficiency, current TE materials have found limited commercial applications. Therefore, the growing need for energy-harvesting power sources is driving a growing interest in developing a new generation of thermoelectric materials (Elsheikh et al. 2014).

### 11.2.1 Characterizations of Thermoelectric Materials

Thermoelectric materials are characterized by the figure of merit ZT (Elsheikh et al. 2014):

$$\mathrm{ZT} = \frac{\alpha^2 \sigma T}{K} \tag{11.1}$$

where $\alpha$ is the Seebeck coefficient, $\sigma$ is the electrical conductivity, and $K$ is the thermal conductivity. The higher the ZT, the more efficient the TE. The complex relationships of these thermoelectric parameters can be expressed as (Zhang and Zhao 2015):

$$\alpha = \frac{8\pi^2 k_B^2}{3eh^2} m^* T \left(\frac{\pi}{3n}\right)^{2/3} \tag{11.2}$$

$$\sigma = ne\mu = \frac{ne^2\tau}{m^*} \tag{11.3}$$

$$K_{\mathrm{to}} = K_{\mathrm{la}} + K_{\mathrm{el}} = K_{\mathrm{la}} + L\sigma T \tag{11.4}$$

where $k_B$ is the Boltzmann constant, $m^*$ is the density of states effective mass, $h$ is the Planck constant, $n$ is the carrier concentration, $e$ is per electron charge, μ is the carrier mobility, $\tau$ is the relaxation time, $K_{\mathrm{to}}$ is the total thermal conductivity, $K_{\mathrm{la}}$ is the lattice thermal conductivity, $K_{\mathrm{el}}$ is the electronic thermal conductivity, and $L$ is the Lorenz number.

The complex parameter relationships make the approach of tuning carrier concentration alone difficult to improve ZT. In particular, $\alpha$ and $\sigma$ generally vary in a reciprocal manner; the electrical conductivity and the Seebeck coefficient are inversely related, so it is not generally possible to increase the thermoelectric power factor above a particular optimal value for a bulk material. However, ideal thermoelectric materials would have a high electrical conductivity to allow the conduction of electricity, which would create a potential difference across the sample, and a low thermal conductivity to maintain the temperature gradient between the hot and cold side. Most traditional materials exhibit a correlation between electrical and thermal conductivity. A material that conducts electricity well, such as a metal, also conducts heat well, and a material that insulates heat, such as glass or ceramic, also insulates electricity. For devices operating at room temperature ($T$~300 K), traditional thermoelectric materials, such as bismuth telluride ($Bi_2Te_3$) and lead telluride (PbTe), possess values of ZT~1. Superlattices and quantum dots-based materials has increased their room temperature ZT to 2–2.4. These improvements in performance are primarily the result of a reduction in lattice thermal conductivity, and the thermoelectric power factor ($\alpha^2\sigma$) is largely unchanged. For practical purposes, a suitable high-performance TE material should have a ZT of 4.4, and the achievement of this goal has remained a formidable challenge (Elsheikh et al. 2014).

#### 11.2.1.1 The Seebeck Coefficient Enhanced with Band Structure Engineering

Generally, most metals possess Seebeck coefficients of 10 μV/K or less, but semiconductor materials are promising for the construction of thermocouples because they have Seebeck coefficients in excess of 100 μV/K. However, achieving ZT > 2 requires thermopower ≥225 μV/K (Elsheikh et al. 2014).

The Seebeck coefficient enhancement in PbTe was first tried by the density-of-states (DOS) distortion through Tl doping. Such a situation can occur when the valence or conduction band of the host semiconductor resonates with the localized impurity energy level. Compared with Na doped PbTe with the same carrier concentration, Tl enhancement is similar in character to that caused by resonant states in PbTe by Tl doping. Indeed, the Mn and Mg alloying in PbTe produced a high ZT of 1.6 at 700 K and 2.0 at 873 K, respectively. The intra matrix band engineering has also been successfully applied to other systems such as the PbSe-SrSe, $Mg_2Si$-$Mg_2Sn$, and the SnTe systems. However, this approach is challenged by the deteriorations of carrier mobility (Zhang and Zhao 2015).

#### 11.2.1.2 Thermal Conductivity Reduced by All-Scale Hierarchical Architectures

A high-quality thermoelectric material must have a high electrical conductivity, a high thermopower, and a low thermal conductivity. Because the first two are determined only by the electronic properties of the material, they are often combined into the quantity $\alpha^2\sigma$, referred to as the "power factor." In contrast, the thermal conductivity in thermoelectrics is the sum of two contributions as shown in Eq. (11.4): electrons and holes transporting heat ($K_{la}$) and phonons traveling through the lattice ($K_{el}$). As $K_{la}$ is determined by the structure, rigidity, atomic masses, and other characteristics of the lattice, reducing lattice thermal conductivity is an effective method to enhance thermoelectric performance. The lattice thermal conductivity can be given by (Zhang and Zhao 2015):

$$K_{la} = 1/3C_v vl \tag{11.5}$$

where the heat capacity ($C_v$) and the phonon velocity ($v$) are constant, so the lattice thermal conductivity is governed by the phonon mean free path (MFP) $l$. When the dimension of inclusions/defects is comparable to the MFP, the phonons will be effectively scattered. Acoustic phonons carry most of the heat in a material, and they have a spectrum of wavelengths and mean free paths (MFP) distribution, including short, medium, and long wavelength phonons, synergistically contributes to the total thermal conductivity. Therefore, all length-scale structures corresponding to the broad spectrum of heat carrying phonons should be the main design principle for high-performance thermoelectric materials. The most important factors that can aid in accomplishing this are (Elsheikh et al. 2014): (a) the use of compounds with complex crystal structures, (b) the presence of heavy atoms weakly bonded to the structures, (c) the existence of inclusions and/or impurities, (d) the formation of solid

solutions and nano-scale precipitates, and (e) the existence of a large number of grain boundaries.

Compounds by substituting the crystal lattice with amorphous (glass-like) structures and phonon-glass electron-crystals (PGEC) have been developed as thermoelectric materials, such as skutterudite materials. A PGEC material would possess electronic properties similar to those normally associated with a good semiconductor single crystal but would have thermal properties akin to those of an amorphous material. The high-performance thermoelectric material would have regions of its structure composed of a high-mobility semiconductor, which provides the electron-crystal electronic structure, interwoven with a phonon glass. The phonon-glass region would be ideal for hosting dopants and disordered structures without disrupting the carrier mobility in the electron-crystal region (Elsheikh et al. 2014).

The introduction of nanostructure has also become a potential tool for reducing thermal conductivity and consequently increasing ZT. Nano-inclusions can be obtained by several approaches, including embedded nano-inclusions, dispersing in situ partially oxidized nanoparticles in matrix, and the endotaxial nanoprecipitates. A general approach for introducing endotaxial nanostructures in a parent matrix is through nucleation and growth of a second phase, which is required to have a low solubility in the solid state, but complete solubility in the liquid state. To get the polycrystallines, the spark plasma sintering (SPS) is a suitable and effective technology to fabricate highly dense and fine-grained thermoelectric materials. In term of developing scalable materials, there are several effective methods of powder processing, including mechanical alloying (MA), rapid melt spinning (MS), and self-propagating high-temperature synthesis (SHS) (Zhang and Zhao 2015).

The utilization of nanostructures has led to the achievement of ZT values of approximately 1–2 or above compared to ~1 and below for bulk materials. The nanostructured $Bi_xSb_{2-x}$ $Te_3$ have been shown to exhibit significantly improved ZT ≈ 1.4 at 100 °C, mostly because of the reduced $K_{la}$. The thermoelectric figure of merit in nanostructured p-type silicon germanium bulk alloys has also been enhanced, due most likely to the increased phonon scattering at the grain boundaries and crystal defects formed by lattice distortion, with some contribution from the increased electron power factor at high temperatures (Joshi et al. 2008; Elsheikh et al. 2014).

#### 11.2.1.3 Electrical Resistivity

The optimum range of electrical resistivity ($\rho$) for a thermoelectric material is from $10^3$ to $10^2$ Ωm. Variations in the electrical resistivity of a semiconductor depend on changes in the carrier concentration and the mean free path of the charge carriers which are reflected/scattered by the surface of the material when they reach it. To achieve low electrical resistivity in semiconductors, the lattice should have nearly infinite conductance at low temperatures, but in reality, the conductivity of semiconductors is very low at low temperatures because of the limited number of free electrons. Moreover, the analysis of the temperature dependence of the electrical

resistivity in intermetallic compounds is a powerful tool for obtaining information regarding the intrinsic properties of these materials. Depending on the temperature range considered, one can draw certain conclusions regarding the scattering of electrons on the thermal excitations of the lattice (Elsheikh et al. 2014).

#### 11.2.1.4 Diffusion Effect

Diffusion is the movement of particles from regions of high concentration to regions of low concentration. Self-diffusion in compound semiconductors is more complex than in elemental semiconductors because of the larger number of possible native point defects that can, in principle, mediate self-diffusion. In addition to vacancies and self-interstitials on the corresponding sublattices, antisite defects must be considered. Homogeneities in thermoelectric materials are affected by the temperature gradient because the optimal properties can only be obtained within a very narrow temperature region for each homogeneous material, which greatly limits the efficient utilization of many dispersed energy sources. However, the diffusion effect depends on the bandgap width and the ratio of electron conductivity to hole conductivity. Heavy carrier doping effectively suppresses the diffusion effect, i.e., it inhibits the increase of thermal conductivity at high temperatures. The undesirable diffusion of thermoelectric materials when placed in a thermal gradient will result in nonhomogeneous and inferior materials, and the importance of diffusion processes is evident at temperatures of approximately 80–90% of the absolute melting point of the materials. A micro-thermoelectric device consists of a bonding layer, electrodes, and thermoelectric thin films. At the interfaces between the metallic electrodes, solder materials, and thermoelectric thin films in a micro-thermoelectric device, diffusion occurs and degrades the performance and reliability of the device. Thus, a Ni layer is usually used as the diffusion barrier in some commercial devices that use bulk thermoelectric materials. However, because of undesirable and unpredictable diffusion phenomena, modern process technologies try to reduce diffusion by decreasing the thermal range experienced by the device during operation (Elsheikh et al. 2014).

#### 11.2.1.5 Oxidizability

Electrically conductive oxide systems have been recognized as potential candidates for thermoelectric materials; these thermoelectric oxides can be used at high temperatures without deterioration of their performance caused by oxidation, and their production costs are comparatively low. Of p-type transparent semiconducting oxide (TSO) materials, $Cu_2O$ is one of the most promising candidates, and because of the effect of the oxygen flow rate during deposition on the properties of $Cu_2O$ films, the oxygen flow rate must be kept low to avoid the over-oxidation of $Cu_2O$ to CuO and to ensure a non-oxidized/non-poisoned metallic copper target in the reactive sputtering environment. The proper control of the amount and flow rate of oxygen during deposition can produce good-quality p-type transparent $Cu_2O$ films with electrical resistivity ranging from $10^2$ to $10^4$ Ω cm, hole mobilities of 1–10 $cm^2$/V-s, and optical band gaps of 2.0–2.6 eV. Measurements of the Seebeck coefficient and electrical resistivity are most likely among the most sensitive means for the

detection of small amounts of diffusive oxidation. However, in some compounds, traces of diffusive oxidation that are visually and chemically undetectable can so severely affect the Seebeck coefficient as to change its sign, and the resistivity can be increased by several decades as a result of this process (Elsheikh et al. 2014).

#### 11.2.1.6 Brittleness

At low temperatures (up to 200 K), single crystals of the Bi–Sb alloys exhibit the best thermoelectric performances, but the brittleness of the single crystals is a problem in practical devices. Development of nanostructured TE materials has been focused on improving their mechanical properties (reduce brittleness and improve machining) and improving their TE properties (figure of merit). Rapid solidification processes (RSPs) such as gas atomization and melt spinning can offer a novel opportunity for modifying the intrinsic brittleness and thermoelectric anisotropy of Bi-Te-based thermoelectric materials by forming a fine-grained and homogeneous microstructure (Elsheikh et al. 2014).

#### 11.2.1.7 Compression and Shear Strength

The average strength (the mean of the strength distribution) and Young's modulus (which characterizes the stress–strain response of a brittle material prior to fracture) are fundamental to understand the mechanical properties of a TE material in a practical device. Enhancement of the mechanical strength of a TE module will render it more robust. The largest improvement must be in the shear strength, which is the weakest point of many TE modules. The compressive strength also must be increased, especially near the perimeter of the module. Such additional compressive strength will be especially useful in preventing damage to the module if, during the assembly process, clamping forces are accidentally applied unevenly to the module. Not only does the brittleness of the material limit the resistance of the device to mechanical and thermal shocks, but the cutting and fabrication of the arms themselves require that the materials used not be too brittle. Nanostructured materials, such as nanoparticles, nanowires, nanotubes, nanopillars, thin films, and nanocrystals, have revealed a host of "ultra-strength" phenomena, which are defined by the stresses in a material component generally increasing to a significant fraction of its ideal strength—the highest achievable stress of a defect-free crystal at zero temperature. However, while thermoelectric modules exhibit relatively high mechanical strength in the compression mode, their shear strength is comparatively low (Elsheikh et al. 2014).

#### 11.2.1.8 Coefficient of Thermal Expansion (CTE)

Thermal expansion is critical, as devices for high-temperature applications will be subjected to extreme temperature fluctuations. This property, defined as the fractional change in length or volume with a unit change in temperature, affects several aspects of the design of thermoelectric devices. Generally, the thermal expansion coefficient $\alpha$ ($\alpha = (\Delta L/L_0)/(T_2 - T_1)$) varies inversely with the melting temperature ($T_m$), and it has been empirically confirmed that the product $\alpha T_m$ is a constant for many substances. This means that a material with high $T_m$ should exhibit low $\alpha$. The

CTE of TE materials is of critical importance because the shear stress is proportional to the temperature gradient, and the larger the heterogeneity in the thermal expansion coefficient of a material is, the larger is the shear stress that will result (Elsheikh et al. 2014).

### 11.2.2 Structures of Thermoelectric Materials

Thermoelectric materials comprise a huge family, including various materials from semimetals, semiconductors, ceramics to polymers, containing various crystalline forms from monocrystals and polycrystals to nanocomposites and covering varying dimensions from bulk, films, and wires to clusters. Figure 11.3 summarizes the reported ZT values of typical thermoelectric materials per publishing years (Zhang and Zhao 2015). According to the optimal working temperature, the thermoelectric materials can be divided into three ranges: $Bi_2Te_3$-based low-, PbTe-based middle-, and SiGe-based high-temperature ranges, with typical temperatures varying from <400 K, 600–900 K, and > 900 K, respectively. To retrospect the history of thermoelectric materials that have been developed for nearly 200 years since the observation of the Seebeck effect in 1821, the development can be divided into three generations according to ZT values. In the first generation, ZT is about 1.0, and the devices can operate at a power conversion efficiency 4–5% (approximately estimated from the maximum ZT), as shown in the left purple part of Fig. 11.3. The second period was ignited by size effects and extends to 1990s, with ZT being pushed to about 1.7, by the introduction of nanostructures; the power conversion efficiency can be expected to be of 11–15%, as shown in the middle blue part of

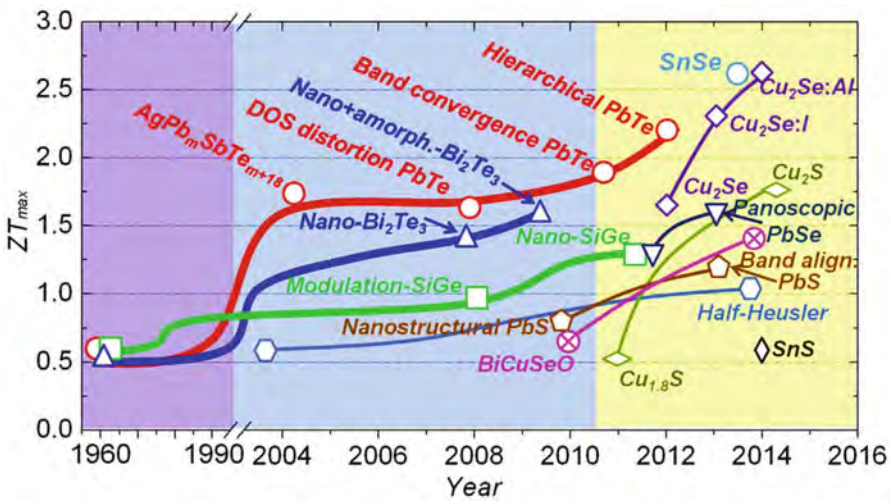


**Fig. 11.3** ZT of the current bulk thermoelectric materials as a function of year (Adapted with permission from Zhang and Zhao (2015) (Elsevier))

Fig. 11.3. The third generation of bulk thermoelectrics has been under development recently, some new concepts and new technologies have pushed ZT to 1.8 and even higher; the predicted device conversion efficiency increases to 15–20%, as shown in the right yellow part of Fig. 11.3. The development history in the thermoelectric also exhibits a trend of pursuing low-cost and earth-abundant characterizations besides high ZTs > 2.0. Advanced approaches to enhance ZT that have emerged include (Zhang and Zhao 2015): modifying the band structure, heavy valence (conduction) band convergence, quantum confinement effects, and electron energy barrier filtering to enhance Seebeck coefficients; nanostructuring and all-scale hierarchical architecturing to reduce the lattice thermal conductivity; and band energy alignment between nano-precipitate/matrix to maintain hole mobility. Most of these approaches aim to maintain a high power factor and/or reduce the lattice thermal conductivities. Alternatively, high performance in thermoelectric materials with intrinsically low thermal conductivity may arise from a large molecular weight, a complex crystal structure, anharmonic, anisotropic bonding, weak chemical bonding, or ion liquid-like transport behavior, and more others (Zhang and Zhao 2015).

### 11.2.2.1 Metal-Based Thermoelectrics

The earliest application of the thermoelectric effect was in metal thermocouples, which have been used to measure temperature and radiant energy for many years. Most state-of-the-art metallic thermoelectric (TE) materials contain heavy elements Bi, Pb, Sb, or Te and exhibit maximum figure of merit, ZT~1–2. However, these materials are mostly toxic and unstable at high temperatures (1000 K). Therefore, metal oxides that exhibit good TE performance are in high demand because metal oxides are environmentally friendly and essentially stable at high temperatures (Fig. 11.4a). For example, $(Ni_{1-x}M_x)Mn_2O_4$ (M = Zn and Mg, $x = 0$, 0.1, and 0.2) has developed with increased activation energy for electrical conduction above a certain temperature (450 °C). Hence, high-performance TE materials based on

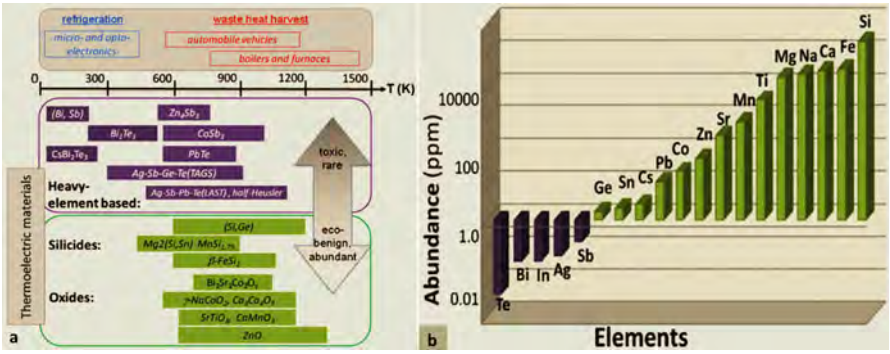


**Fig. 11.4** Schematic comparison of various thermoelectric (TE) materials for applications of waste heat harvest and refrigeration, in terms of the temperature range of operation and the abundance and environmental friendliness of constituent elements (**a**). The abundance of elements used in TE materials, the elements represented by dark colored columns are, 1 ppm (**b**) (Adapted with permission from He et al. (2011) (Cambridge University Press))

abundantly available (Fig. 11.4b) and nontoxic elements with high chemical and thermal stability are crucial for any viable large-scale applications. As shown in Fig. 11.4a, oxides are particularly suitable for high-temperature power generation in air (He et al. 2011). In the low-temperature region, the absolute value of the thermoelectric power is increased by Mg substitution, and the thermoelectric powers change sign from negative to positive as the temperature increases. In addition, phonon-glass electron-crystal PGEC materials, such as clathrates and filled skutterudites, have been developed. Clathrates are periodic solids in which tetrahedrally coordinated atoms form cages that surround a metal atom. Clathrate I materials have the general formula $A_8E_{46}$, with A = Na, K, or Ba and E = Al, Ga, In, Si, Ge, or Sn. Clathrates II and III have idealized formulas of $A_{24}E_{136}$ and $A_{30}E_{172}$, respectively, and exist with the same A and E elements. The low thermal conductivities for semiconducting clathrates are attributed to resonant scattering of the acoustic heat-carrying phonons by the guest atoms. The localized low-frequency vibration mode of the guest atoms is expected to cut through the acoustic branches, which decreases the number of acoustic phonon modes and effectively limits the heat transport, i.e., the enhanced vibration of the guest atoms A causes a flattening of the phonons bands, lowering the velocity of the phonons, which significantly contributes to the low thermal conductivity of these materials. However, a few studies have investigated clathrate structures, and all have reported ZT <1 (Elsheikh et al. 2014).

Moreover, systems with the phonon mean free path larger than the charge carrier mean free path can exhibit an enhanced thermoelectric efficiency. This can be realized in amorphous thermoelectrics. This ground-breaking idea was accomplished in Cu–Ge–Te, $NbO_2$, In–Ga–Zn–O, Zr–Ni–Sn, Si–Au, and Ti–Pb–V–O amorphous systems. Naturally, amorphous thermoelectrics give rise to extensive phonon scattering, which is still a challenge for crystalline thermoelectrics. A bright future is expected for these materials (Music et al. 2016).

In addition, functionally graded materials make it possible to improve the conversion efficiency of existing thermoelectrics. These materials have a non-uniform carrier concentration distribution and in some cases also solid solution composition. In power generation applications the temperature difference can be several hundred degrees and therefore devices made from homogeneous materials have some part that operates at the temperature where ZT is substantially lower than its maximum value. This problem can be solved by using materials whose transport properties vary along their length, thus enabling substantial improvements to the operating efficiency over large temperature differences. This is possible with functionally graded materials as they have a variable carrier concentration along the length of the material, which is optimized for operations over specific temperature range (Rowe 2005).

#### 11.2.2.2 Ceramic Thermoelectric Materials

Ceramic thermoelectric materials have been widely explored for high-temperature application in energy conversion systems, including metal oxides, Ti sulfides, and Mn silicides, which are usable in air atmosphere at 300–1200 K, for cascade-type

modules. Oxide compounds such as $NaCo_2O_4$, $LaCoO_3$, $(ZnO)_mIn_2O_3$, $BaSnO_3$, $BaPbO_3$, $Ca_3Co_4O_9$, $Sr_{1-x}Nd_xTiO_3$, and $Bi_2Ca_2Co_2O_x$ are promising candidates for thermoelectric materials because of their transport properties and their physical and chemical stability. The addition of titanate nanotubes (TNTs) (2 vol%) fabricated via the pressureless sintering method has been found to enhance the ZT value of Nb-doped $SrTiO_3$ polycrystalline ceramic to approximately 0.14 at 900 K. $(Ca_{1-x}Sr_x)_3Co_4O_9$ polycrystalline has been fabricated by using spark plasma sintering method to substitute Ca by Sr, and the figure of merit ZT achieves 0.22 at 1000 K for the composition $(Ca_{0.995}\ Sr_{0.005})_3Co_4O_9$. However, the fabrication of modules based on oxide materials make it a difficult task and different from that of conventional thermoelectric modules (Elsheikh et al. 2014).

Some layered oxide materials are thought to have ZT~2.7 at 900 K. If the layers in a given material have the same stoichiometry, they will be stacked so that the same atoms will not be positioned on top of each other, impeding phonon conductivity perpendicular to the layers. Other members of this family include ZnO, $MnO_2$, and $NbO_2$, and so on (Rowe 2005).

Furthermore, calcium cobaltite ($Ca_3Co_4O_9$) basically shows good TE performance at high temperatures in air and appears to be the best p-type material at the moment. It is already installed in a commercial TE module for high-temperature energy harvesting. Calcium manganate ($CaMnO_3$) seems to be the best n-type material for high-temperature energy harvesting, while indium oxide-based compounds are another candidate n-type materials, although they are somewhat inferior to calcium manganate due to high vapor pressure of indium oxide at high temperatures. Calcium manganate is chosen for n-type TE elements in a commercial module. Strontium titanate ($SrTiO_3$) also shows good TE performance at high temperatures in a reducing atmosphere, but it degrades rapidly above 700 K in air. Accordingly, nanostructured ceramics of STO, especially 3D superlattice ceramics with 2DEG GBs, are proposed for low-temperature applications, and the simulation work has shown its possibility to exceed TE performance of the conventional bulk bismuth telluride material at room temperature. Development of a new process to realize 3D superlattice with millimeter order size is urgently required. Higher manganese silicide ($MnSi_x$) as *p*-type and titanium sulfide ($TiS_2$)-related compounds as *n*-type materials for mid-temperature energy harvesting are proposed to be good candidates for the future (Koumoto et al. 2013).

#### 11.2.2.3 Polymer-Based Organic Thermoelectric Materials

Polymer-based organic thermoelectric materials are very attractive because they are light, flexible, and suitable for room-temperature applications and because they generally require relatively simple manufacturing processes (i.e., spin coating, inkjet printing or 3D printing) compared to semiconductor-based thermoelectrics. Polymers are intrinsically poor thermal conductors, which make them ideal for use as thermoelectrics, but their low electrical conductivity, Seebeck coefficient, and stability have hampered their use in thermoelectric applications. However, compared to inorganic TE materials, organic or polymer TE materials exhibit several inherent advantages, such as potentially low cost because of the abundance of carbon

resources, simple synthesis in general, abundant electron-energy bands through modulation, simple processing into versatile forms, high energy density, and low k, which may be of great importance for their potential TE applications (Elsheikh et al. 2014).

Some electrically conducting organic materials may have a higher figure of merit than existing inorganic materials. Seebeck coefficient can be even millivolts per Kelvin but electrical conductivity is usually low, resulting in small ZT values. Quasi-one-dimensional (Q1D) organic crystals are formed from linear chains or stacks of molecules that are packed into a 3D crystal. Under certain conditions some Q1D organic crystals may have ZT~20 at room temperature for both p- and n-type materials. This has been credited to an unspecified interference between two main electron-phonon interactions leading to the formation of narrow strip of states in the conduction band with a significantly reduced scattering rate as the mechanism compensate each other, yielding high ZT (Casian and Sanduleac 2013).

That is, the physical and chemical properties of certain polymers are tunable within a fairly large range of modifications of their molecular structures. The ionic conducting polymers, such as poly (3,4-ethylenedi oxythiophene):poly(styrene-sulfonate) (PEDOT: PSS), which possess high electrical conductivity and intrinsically low thermal conductivity, are considered to be the most promising novel organic TE materials. In a two-component nanocomposite, the selection of a conducting polymer and an inorganic thermoelectric material may yield high thermoelectric power and high electrical conductivity of the material. Because these properties are dependent on the particle size and morphology, it is interesting to map the relation between the structural and electrical properties of the material. Nanocomposites/hybrids/heterostructures of inorganic thermoelectrics with conducting polymers have been investigated based on conducting polymers such as polyaniline (PANI), polythiophene (PTH), and poly (3,4-ethylenedioxythiophene):poly(styrenesulfonate) (PEDOT:PSS), as well as other polymers such as polyacetylene (PA), polypyrrole (PPY), polycarbazoles (PC), and polyphenylenevinylene (PPV); these materials appear to have great potential for producing relatively low-cost and high-performance TE materials. In polymer and polymer–inorganic TE nanocomposites, the value of the Seebeck coefficient typically ranges from 4088 to 1283 μV/K, the electrical conductivity ranges from $10^7$ to $10^4$ S/cm, and the thermal conductivity ranges from 0.02 to 1.2 W/m-K. However, it has been demonstrated that the transport properties of conducting polymers are greatly influenced by the process of doping with various materials (Elsheikh et al. 2014).

#### 11.2.2.4 Semiconductors

Since the late 1950s, semiconducting thermoelectric devices has been applied for terrestrial cooling and power generation and later for space power generation because of their competitive energy conversion compared to other types of small-scale electric power generators. Semiconductor thermoelectric power generation, which is based on the Seebeck effect, has very interesting capabilities with respect to conventional power-generation systems. During the 1990s, there was a heightened interest in the field of thermoelectrics driven by the need for more efficient materials

for electronic refrigeration and power generation. Because of the use of semiconductor materials for thermoelectric applications, there has been a considerable effort to improve the figures of merit (ZT) of these materials to greater than three to make them commercially viable. Semiconductor materials are promising for the construction of thermocouples because they have Seebeck coefficients in excess of 100 $\mu VK^{-1}$, and the only way to reduce k without affecting $\alpha$ and $\sigma$ in bulk materials, thereby increasing ZT, is to use semiconductors of high atomic weight, such as $Bi_2Te_3$ and its alloys with Sb, Sn, and Pb. A high atomic weight reduces the speed of sound in the material and thereby decreases the thermal conductivity. A solid-state or semiconductor electronics component, for example, can perform well and reliably for many years when it is operating at or near the ambient temperature. Intermetallic compounds such as $Mg_2X$ (X = Si, Ge, Sn) and their solid solutions are semiconductors with the antifluorite structure and have been proposed as good candidates for high-performance thermoelectric materials because of their superior features such as large Seebeck coefficients, low electrical resistivities, and low thermal conductivities. However, the best-ZT materials are found to be heavily doped, small-band-gap semiconductors (Elsheikh et al. 2014).

Silicon-germanium alloys are currently the best thermoelectric materials around 1000 °C and are therefore used in some radioisotope thermoelectric generators (RTG) (notably the MHW-RTG and GPHS-RTG) and some other high-temperature applications, such as waste heat recovery. Usability of silicon-germanium alloys is limited by their price and mid-range ZT (~0.7).

#### 11.2.2.5 Nanomaterials and Superlattices

In addition to nanostructured $Bi_2Te_3/Sb_2Te_3$ superlattice thin films, other nanomaterials also show potential in improving thermoelectric properties, such as PbTe/PbSeTe quantum dot superlattice. It exhibits an enhanced *ZT* (approximately 1.5 at room temperature) that was higher than the bulk *ZT* value for either PbTe or PbSeTe (approximately 0.5). Compared with normal skutterudites, nanostructured skutterudites have reduced thermal conductivity, caused by grain boundary scattering. *ZT* values of ~0.65 and >0.4 have been achieved with $CoSb_3$-based samples; the former values were 2.0 for Ni and 0.75 for Te-doped material at 680 K and latter for Au-composite at $T > 700$ K. Even greater performance improvements can be achieved by using composites and by controlling the grain size, the compaction conditions of polycrystalline samples, and the carrier concentration (Szczech et al. 2011).

Due to the unique nature of graphene, it is possible to develop a thermoelectric device based on it with an extremely high Seebeck coefficient. One theoretical study suggests that the Seebeck coefficient might achieve a value of 30 mV/K (Hossain et al. 2015).

Superlattices - nano structured thermocouples, are considered a good candidate for better thermoelectric device manufacturing, with materials that can be used in manufacturing this structure. Their production is expensive for general-use due to fabrication processes based on expensive thin-film growth methods. However, since the amount of thin-film materials required for device fabrication with superlattices is

so much less than thin-film materials in bulk thermoelectric materials (almost by a factor of 1/10,000) the long-term cost advantage is indeed favorable. Superlattice structures also allow the independent manipulation of transport parameters by adjusting the structure itself enabling research for better understanding of the thermoelectric phenomena in nanoscale, and studying the phonon-blocking electron-transmitting structures—explaining the changes in electric field and conductivity due to the materials nano-structure. Many strategies exist to decrease the superlattice thermal conductivity that are based on engineering of phonon transport. The thermal conductivity along the film plane and wire axis can be reduced by creating diffuse interface scattering and by reducing the interface separation distance, both which are caused by interface roughness. In nature, roughness is caused by the mixing of atoms of foreign elements. Artificial roughness can be created using various structure types, such as quantum dot interfaces and thin-films on step-covered substrates (Zhang et al. 2012).

Reduced phonon-scattering interface structures often also exhibit a decrease in electrical conductivity. One approach to overcome the decrease in electrical conductivity in reduced phonon-scattering structures is to increase phonon reflectivity and therefore decrease the thermal conductivity perpendicular to the interfaces. This can be achieved by increasing the mismatch between the materials in adjacent layers, including density, group velocity, specific heat, and the phonon-spectrum. Interface roughness causes diffuse phonon scattering, which either increases or decreases the phonon reflectivity at the interfaces. A mismatch between bulk dispersion relations confines phonons, and the confinement becomes more favorable as the difference in dispersion increases. Attempts to Localize long wavelength phonons by aperiodic superlattices or composite superlattices with different periodicities have been made. In addition, defects, especially dislocations, can be used to reduce thermal conductivity in low-dimensional systems (Zhu and Ertekin 2014).

The Seebeck coefficient can change its sign in superlattice nanowires due to the existence of minigaps as Fermi energy varies. This indicates that superlattices can be tailored to exhibit n or p-type behavior by using the same dopants as those that are used for corresponding bulk materials by carefully controlling Fermi energy or the dopant concentration. With nanowire arrays, it is possible to exploit semimetal-semiconductor transition due to the quantum confinement and use materials that normally would not be good thermoelectric materials in bulk form. Such elements are, for example, bismuth. The Seebeck effect could also be used to determine the carrier concentration and Fermi energy in nanowires. In quantum dot thermoelectrics, unconventional or nonband transport behavior (e.g., tunneling or hopping) is necessary to utilize their special electronic band structure in the transport direction. It is possible to achieve $ZT > 2$ at elevated temperatures with quantum dot superlattices, but they are almost always unsuitable for mass production. However, in superlattices, where quantum-effects are not involved, with film thickness of only a few micrometers (μm) to about 15 μm, $Bi_2Te_3/Sb_2Te_3$ superlattice material has been made into high-performance microcoolers and other devices. The performance of hot-spot coolers is consistent with the reported ZT~2.4 of superlattice materials at 300 K (Shah 2018).

Nanocomposites are promising material class for bulk thermoelectric devices, but several challenges have to be overcome to make them suitable for practical applications. It is not well understood why the improved thermoelectric properties appear only in certain materials with specific fabrication processes. SrTe nanocrystals can be embedded in a bulk PbTe matrix so that rocksalt lattices of both materials are completely aligned (endotaxy) with optimal molar concentration for SrTe only 2%. This can cause strong phonon scattering but would not affect charge transport. In such case, ZT~1.7 can be achieved at 815 K for p-type material (Biswas et al. 2011).

### 11.2.3 Applications of Thermoelectric Materials for Renewable Energy

Thermoelectric (TE) modules comprise arrays of thermoelectric (TE) junctions, which are connected electrically in series and thermally in parallel. The TE junctions, in turn, consist of p- and n-type thermoelectric materials, which are selected from the range of materials based primarily on their physical thermoelectric performance. Auxiliary to the basic array of TE modules are components that contribute to the overall efficiency of the module, such as heat sinks, which absorb heat from the hot side, and cooling fins or cooling systems, which dissipate heat from the cool side. Typically, a single module may produce power in the range of 1–125 W and may be modularly connected to produce power up to 5 kW. The maximum temperature gradient between the hot and cold side can be as high as 70 °C. Given the nature of TE modules as solid-state devices with no moving parts, they are durable and reliable, with over 100,000 h of operating lifetimes, and have a simple structure. They may operate in two modes (Elsheikh et al. 2014): as thermoelectric generators (TEGs), generating electricity from a temperature gradient, or as thermoelectric coolers (TECs), converting a direct current into a temperature gradient.

Solar thermoelectric generators (STEGs) were initially designed and optimized for space applications because of their advantages of reliability and long lifetimes as well as their ability to capture high levels of incident solar radiation in extraterrestrial regions; however, much of the recent interest in these systems has been focused on residential solar-thermal-energy harvesting. The STEG may be described as consisting of a TEG and a thermal collector. Solar heat can be absorbed by the thermal collector and then concentrated and conducted over the thermoelectric generator using a fluid pipe or some other means. Subsequently, the thermal resistance of the thermoelectric generator will lead to a temperature difference that is proportional to the heat flux from the absorber of the thermal collector to the fluid. As a result, electric power will be generated by the thermoelectric generator, and this power will be proportional to the temperature difference. Moreover, the evacuated-tube heat-pipe solar collectors had a significant effect on the TEG by increasing the thermal efficiency by approximately 55%, which may increase the performance to above 1%. A novel hybrid solar thermoelectric (HSTE) system uses a thermosyphon

to passively transfer heat to a bottoming cycle to determine the overall performance in a temperature range of 300–1200 K for solar concentrations of 1–100 suns and various thermosyphon and thermoelectric materials with a geometry resembling an evacuated-tube solar collector. Bismuth telluride, lead telluride, and silicon germanium thermoelectrics were studied with copper/water, stainless-steel/mercury, and nickel/liquid-potassium thermosyphon/working-fluid combinations. The system contained a parabolic trough mirror that concentrated solar energy onto a selective-surface-coated thermoelectric to generate electrical power, and a thermosyphon adjacent to the back side of the thermoelectric maintained the temperature of the cold junction and carried the remaining thermal energy to a bottoming cycle. This HSTE system demonstrated that ideal efficiencies as high as 52.6% can be achieved at a solar concentration of 100 suns and a bottoming-cycle temperature of 776 K. However, the performance of a solar thermoelectric generator is primarily limited by the thermoelectric materials used to construct it; bismuth telluride is a favorable low-temperature thermoelectric material that exhibits advantageous properties and can reache a maximum of ZT 1 at low temperatures in the range of 25–225 °C, while filled skutterudite is a good medium-temperature thermoelectric material that can be operated over a wide temperature range 25–525 °C. Moreover, the total conversion efficiency for solar energy of a solar thermoelectric generator based on a multistage thermoelectric module could be as high as 10%. With the continuous emergence of new thermoelectric materials, solar thermoelectric generators using multistage and hybrid-generation-system (HGS) thermoelectric modules will have good application prospects (Elsheikh et al. 2014).

Many new types of thermal-energy sensors based on the Peltier effect or Seebeck effect of thermoelectric modules have been developed, such as sensors for power ultrasound effects, cryogenic heat-flux sensors, water-condensation detectors, fluid-flow sensors, and infrared sensors. These sensors generally rely on the conversion of heat into electrical signals or vice versa. Infrared (IR) sensors, which operate on the principle that any mass radiates heat, allow the detection of heat using the Seebeck effect; the absorption of heat causes a specific temperature rise, which subsequently produces a Seebeck voltage. The main sensor parameters are the responsivity, which is given by the ratio of the sensor voltage to the incoming radiation power; the time constant; and the noise voltage. Most thermoelectric IR sensors are able to operate in the range of 7–14 μm (Elsheikh et al. 2014). A sensor system combining a novel pressure-stable thermoelectric flow and an impedimetric sensor for monitoring chemical conversion in microfluidic channels was developed, for instance. Both sensor chips were optimized for hydraulic diameters of 1 mm and exhibit a high chemical, temperature, and pressure stability. However, in terms of size and light weight, the most effective structure for thermoelectric sensors is the thin-film structure (Leonov 2011; Elsheikh et al. 2014).

Advanced autonomous power systems that can be operated continuously and independently of the sun and are capable of providing electric power from a few watts to hundreds of kilowatts for 7–10 years are required for extraterrestrial exploration vehicles. For example, the solar brightness on Mars and Jupiter is as weak as 45% and 4%, respectively, and it is negligible on other planets. As a result,

the solar option is suitable only for robotic and spacecraft missions that are limited in their time scope of operation and require only a few watts of electrical power (10 W). Radioisotope thermoelectric generators (RTGs) have been used by the United States to provide electrical power for spacecraft since 1961. The required electrical output power levels can be achieved by the appropriate selection of a number of general purpose heat-source (GPHS) modules incorporated in an RTG system. A GPHS module is a composite carbon body that houses a total of four fuel pellets and acts as an aero-impact shell. The isotope fuel for the GPHS-RTG is in the form of plutonium dioxide ($^{238}PuO_2$) at approximately 80% density. For power conversion by the GPHS-RTG, thermoelectric junctions have been used, such as SiGe junctions. SiGe unicouples partially convert the heat generated by the radioactive decay of $^{238}Pu$ in the $^{238}PuO_2$ fuel pellets that are encapsulated in the general-purpose heat-source (GPHS) modules. Previously, lead telluride was used as the thermoelectric converter for lower powered RTGs operated at a maximum hot junction temperature of 865 K to produce a power of 2.7 We. Because of the deleterious effects of oxygen on these materials, silicon germanium thermoelectric elements were later adopted for high-powered RTGs operated at high temperatures of up to 1275 K. Their sublimation rates and oxidation effects, even at these higher temperatures, can be controlled by the use of sublimation barriers around the elements and an inert cover gas within the generator during ground operation. In 1976, the Lincoln Experimental Satellite (LES) 8/9 was the first spacecraft to use the new "4150 We multi-hundred watt (MHW) RTG," which employed 312 SiGe-alloy thermoelectric elements per RTG. Recently, skutterudite alloys with ZTs ranging from 0.92 to 1.48 in the temperature range from 300 to 973 K have been developed at the Jet Propulsion Laboratory (JPL) in Pasadena, California, and are being considered for use in Advanced Radioisotope Power Systems (ARPSs) to support NASA's planetary exploration missions. The use of skutterudite unicouples in the bottom array with SiGe unicouples in the top array has been proposed for cascaded thermoelectric modules (CTMs) for use in radioisotope power systems (RPSs) to generate electric power of 108 We and to achieve a net decrease of 43% in the required amount of $^{238}PuO_2$. However, an operational issue with skutterudite-based unicouples is the sublimation of antimony from the legs near the hot junction at 973 K. Such sublimation could change the thermoelectric properties of the material and degrade the unicouples' performance over time. The use of TEGs in commercial aerospace vehicles, which is expected to reduce fuel consumption by 0.5%, is also being explored by Boeing Research & Technology. As a rough estimate, this fuel savings, if implemented solely in the USA, would save passenger and cargo airlines more than $12 million every month and reduce global carbon emissions by 0.03% (Elsheikh et al. 2014).

## 11.3 Piezoelectric Materials

Piezoelectric effect is a unique property of certain crystal materials where they will generate an electric field or current if subjected to physical stress. The phenomenon was first discovered in 1880 when Pierre and Jacques Curie demonstrated that when

specially prepared crystals (such as quartz, topaz, and Rochelle salt) were subjected to a mechanical stress they could measure a surface charge. After that, the same effect was observed in reverse, where an imposed electric field on the piezoelectric materials will put stress on its structure. One of the first applications of the piezoelectric effect was an ultrasonic submarine detector developed during the First World War. A mosaic of thin quartz crystals glued between two steel plates acted as a transducer that resonated at 50 MHz. By submerging the device and applying a voltage they succeeded in emitting a high-frequency "chirp" underwater, which enabled them to measure the depth by timing the return echo. This was the basis for sonar and the development encouraged other applications using piezoelectric devices both resonating and non-resonating such as microphones, signal filters, and ultrasonic transducers. However many devices were not commercially viable due to the limited performance of the materials at the time. The continued development of piezoelectric materials has led to a huge market of products ranging from those for everyday use to more specialized devices.

### 11.3.1 Fundamentals of Piezoelectricity

The process whereby the piezoelectric effect takes place is based on the fundamental structure of a crystal lattice. Crystals generally have a charge balance, where negative and positive charges precisely cancel each other out along the rigid planes of the crystal lattice. When this charge balance is disrupted by applying physical stress to the crystals, the energy is transferred by electric charge carriers, creating a current in the crystal. With the converse piezoelectric effect, the applying of an external electric field to the crystal will unbalance the neutral charge state, which results in mechanical stress and the slight readjustment of the lattice structure. Therefore, piezoelectricity is the linear interaction between the mechanical and electrical properties of the dielectric materials. For electrical properties, the relationship between the electric displacement ($D_i$) and the electric field ($E_j$) can be interpreted as (Wang et al. 2015a)

$$D_i = \sum_{j=1}^{3} \varepsilon_{ij} E_j \tag{11.6}$$

where the coefficient $\varepsilon_{ij}$ is the permittivity of the dielectric materials. The permittivity coefficient is a second-rank tensor represented by a $3 \times 3$ matrix. However, the matrix is symmetric ($\varepsilon_{ij} = \varepsilon_{ji}$), and there are at most six independent coefficients. For mechanical properties, the relationship between stress and strain under small deformations can be interpreted as (Wang et al. 2015a, b).

$$T_{ij} = \sum_{k,l=1}^{3} c_{ijkl} S_{kl} \tag{11.7}$$

where $c_{ijkl}$ is the elastic stiffness of the material. Equation (11.7) can also be interpreted reversely as (Wang et al. 2015a, b)

$$S_{ij} = \sum_{k,l=1}^{3} s_{ijkl} T_{kl} \tag{11.8}$$

where $s_{ijkl}$ is the elastic compliance of the materials. Because the stiffness and compliance coefficients relate to the second rank tensor stress and strain, they are fourth-rank tensors. However, due to the symmetric stress and strain ($T_{ij} = T_{ji}$, $S_{ij} = S_{ji}$), the number of $c_{ijkl}$ can be reduced to 36. In reduced notation, the piezoelectric constitutive equation can be interpreted as (Falconi et al. 2012)

$$D_i = \varepsilon_{ij}^{T} E_j + d_{iJ} T_j \tag{11.9}$$

$$S_I = d_{Ij} E_j + S_{IJ}^{E} T_j \tag{11.10}$$

where the superscripts $T$ and $E$ mean the coefficients are at constant stress and electric field, respectively. The $d_{iJ}$ in Eqs. (11.9) and (11.10) is the piezoelectric strain/charge constant.

Piezoelectric materials are anisotropic dielectrics of special type, where both fields the electrical and the elastic are coupled. Some of them (for instance ceramic) have ferroelectric properties, but the rest of them (as quartz) display no ferroelectric behavior. A dielectric material supports charge without conducting it to a significant degree. The main property of a dielectric material is that it has no free electrical charges, but when an external electrical field is applied the electric dipoles are being created due to the interaction of the electrical field with the dielectric structure. The dipole moment is a vector with direction from the negative to the positive pole. Because of dielectric polarization, positive charges are displaced towards the external field and negative charges shift in the opposite direction. The polarization of piezoelectric material has its specific peculiarities in comparison with polarization of ordinary dielectrics. When a piezoelectric is placed under a mechanical stress, the geometry of the atomic structure of the crystal changes, such that ions in the structure separate, and a dipole moment is formed. For a net polarization to develop, the dipole formed must not be canceled out by other dipoles in the unit cell. Therefore the piezoelectric atomic structure must be non-centrosymmetric. When a piezoelectric material is loaded electrically then the electrical dipoles appear, dipole moment is formed and this results in deformation. The polarization is linear and electrical dipoles nucleate only after electrical or mechanical load. The other types of piezoelectric materials are with ferroelectric properties, i.e., spontaneous polarization and electric dipoles exist in their structure even in the absence of electrical field. The piezoelectric effect in ferroelectric is strongly dependent on its atomic structure.

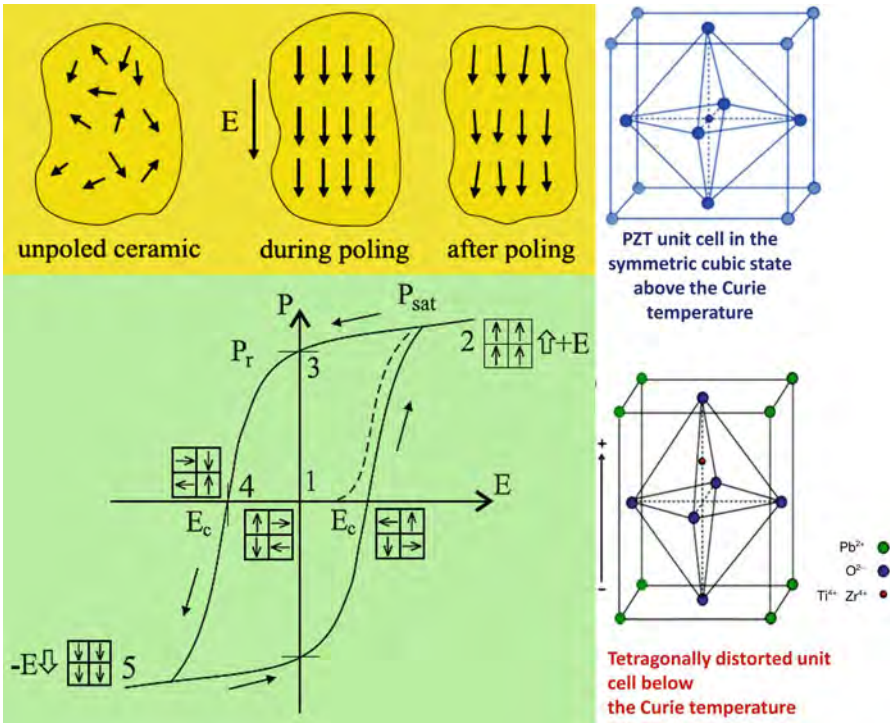


**Fig. 11.5** Hysteresis curve for polarization of piezoelectric material, and domain structure of ferroelectric materials and their behavior during poling process

Depending on the type of a crystal, a compressive stress can increase or decrease the polarization, or sometimes have no effect at all. If a mechanical stress is applied to the ferroelectric, then there are domains which will experience an increase in dipole moment and some which will experience a decrease in dipole moment. Overall, there is no net increase in polarization, as shown in Fig. 11.5 (upper portion). This makes the ferroelectric useless as a piezoelectric unless it is put through some additional processing. This process is called poling. An electric field is applied to the ferroelectric as it passes through its Curie temperature, so that its spontaneous polarization develops and it is aligned in a single direction. All of the domains in the piezoelectric have a dipole moment pointing in that direction, so there is a net with approximately the same polarization (Fig. 11.5, upper portion). When the electric field is removed, most of the dipoles are locked in a configuration of near alignment (Fig. 11.5, upper portion). The full alignment is only possible in a single crystal and in a polycrystalline material there exists still a polarization distribution. The material now has a remanent polarization. The maximum possible value of the remanent polarization is called saturation polarization, i.e., this is the horizontal part of the hysteresis curve in Fig. 11.5 (lower portion). The distinguishing feature of PEM with ferroelectric properties is that the direction of the spontaneous polarization can be reversed by

an applied electric field, yielding a hysteresis loop, as shown in Fig. 11.5 (lower portion). The nonlinear behavior of the polarization with respect to the applied electrical field consists of three stages which are characterized by (Dineva et al. 2014): (a) reversible domain motion; (b) growth of new domains; and (c) new domains reaching the limit of their growth and reaching the saturation polarization.

Figure 11.5 (lower portion) shows a typical hysteresis curve created by applying an electric field to a piezoelectric ceramic element until the maximum (saturation) polarization $P_{\text{sat}}$ is reached, reducing the field to zero determines the remanent polarization $P_{\text{r}}$ reversing the field attains a negative maximum (saturation) polarization and negative remanent polarization, and re-reversing the field restores the positive remanent polarization. When the electric field is the coercive field $E_{\text{c}}$ there is no net polarization due to the mutual compensation of the polarization of different domains. Therefore, PEM is a special type of anisotropic dielectrics where electrical and mechanical fields are coupled due to both the existence of the specific asymmetric atomic structure of the lattice and the existence of spontaneous polarization at the microstructure level; The effective usage of both the ferroelectric properties of the piezoelectric ceramics together with the poling process during their manufacture make these materials a basic element in the modern industrial applications (Dineva et al. 2014).

### 11.3.2 Type of Piezoelectric Materials

Piezoelectric materials can be natural or man-made. Several typical piezoelectric materials, including both natural and synthetic materials, are listed in Table 11.1. Among them, piezoelectric ceramics, crystals, and polymers have been most developed and useful piezoelectric materials. Piezoelectric ceramics usually refer to polycrystalline materials that consisted of irregular collective small grains and are prepared through the solid-state reaction and sintering process. Under the poling electrical field, the disordered spontaneous polarization in piezoelectric ceramics can be realigned and keep the remnant polarization after the removal of external field. As a result, the piezoelectric ceramics can exhibit macropiezoelectric property (Wang et al. 2015a, b). There are the following families of man-made ceramics with crystal structure as perovskite (Dineva et al. 2014): Barium titanate ($BaTiO_3$); Lead titanate ($PbTiO_3$); Lead zirconate titanate ($Pb[Zr_x\ Ti_{1-x}]O_3$, $0 < x < 1$)—more commonly known as PZT; Potassium niobate ($KNbO_3$); Lithium niobate ($LiNbO_3$); Lithium tantalate ($LiTaO_3$), etc. and other lead-free piezoceramics. The general chemical formulae of perovskite crystal structure is $ABO_3$, where A is a larger metal ions, usually lead Pb or barium Ba, B is a smaller metal ion, usually titanium Ti or zirconium Zr, which shows the crystal structure of a piezoelectric ceramic ($BaTiO_3$) at temperature above and below Curie point.

To prepare a piezoelectric ceramic, fine powders of the component metal oxides are mixed in specific proportions, then heated to form a uniform powder. The powder is mixed with an organic binder and formed into structural elements having the desired shape (disks, rods, plates, etc.). The elements are subsequently fired

**Table 11.1** Typical piezoelectric materials (Dineva et al. 2014)

| Category | Typical materials |
|---|---|
| Natural crystals | Berlinite ($AlPO_4$), sucrose, quartz, Rochelle salt, topaz, and tourmaline-group minerals |
| Natural materials | Bone, tendon, silk, wood, enamel, dentin, DNA, and viral proteins |
| Synthetic crystals | Gallium orthophosphate ($GaPO_4$), langasite ($La_3Ga_5SiO_{14}$), and diisopropylammonium bromide (DIPAB) |
| Synthetic ceramics | $BaTiO_3$, $PbTiO_3$, $Pb(Zr,Ti)O_3$, $KNbO_3$, $LiNbO_3$, $LiTaO_3$, $Na_2WO_3$, ZnO, $Ba_2NaNb_5O_5$, $Pb_2KNb_5O_{15}$, and so forth |
| Lead-free piezoceramics | $(K,Na)NbO_3$, $BiFeO_3$, $Bi_4Ti_3O_{12}$, $Na_{0.5}Bi_{0.5}TiO_3$, and so forth |
| Polymers | Polyvinylidene fluoride (PVDF) |
| Organic nanostructures | Self-assembled diphenylalanine peptide nanotubes (PNTs) |
| Piezocomposites | Piezo-polymer in which the piezoelectric material is immersed in an electrically passive matrix; $BaTiO_3$ fibers reinforcing a PZT matrix; multilayer PDMS cellular structures coated with PTFE films and stretchable gold electrodes |

according to a specific time and temperature program, during which the powder particles sinter and the material attains a dense crystalline structure. The elements are cooled, then shaped or trimmed to specifications, and electrodes are applied to the appropriate surfaces. Above a critical temperature, the Curie point, each perovskite crystal in the fired ceramic element exhibits a simple cubic symmetry with no dipole moment; it is in the so-called paraelastic phase. At temperatures below the Curie point, however, each crystal exhibits a tetragonal or rhombohedral symmetry leading to a dipole moment; this phase of the material is called ferroelectric phase. When electric field of about $10^6$ V/m is applied to the ferroelectric polycrystal as it passes through its Curie temperature, so that its spontaneous polarizations develop, all polarization vectors are aligned in a more or less uniform direction. This process leading to a macroscopic net polarization is so-called poling. Initially there exists a uniform distribution of all direction, i.e., no macroscopic net polarization. After poling, a distribution around the poling direction leads to a macroscopic net polarization. Now, at this stage, when a mechanical stress is applied, the polarization will increase or decrease and the ceramic will have typical piezoelectric behavior (Dineva et al. 2014).

Piezoelectric crystals, which refer to single-crystalline materials, are usually unsymmetrical in structure and therefore exhibit piezoelectric property. There are 32 crystal classes which are divided into the following seven groups (Dineva et al. 2014): triclinic, monoclinic, orthorhombic, tetragonal, trigonal, hexagonal, and cubic. These groups are also associated with the elastic nature of the material where triclinic represents an anisotropic material, orthorhombic represents an orthotropic material, and cubic are in most cases isotropic materials. Only 20 of the 32 classes allow piezoelectric properties. Ten of these classes are polar, i.e., show a spontaneous polarization without mechanical stress due to a nonvanishing electric

dipole moment associated with their unit cell. The remaining ten classes are not polar, i.e., polarization appears only after applying a mechanical load.

The piezoelectric ceramics exhibit high piezoelectric constant and permittivity and can be prepared into designed architectures, which makes them suitable for the application in high-power energy transducer and wideband filters. However, the poor mechanical quality factor, high electrical loss, and low stability of the piezoelectric ceramics limited their application in high-frequency devices. Comparatively, the natural piezoelectric crystals such as quartz exhibit lower piezoelectric properties and dielectric constant. Moreover, they are limited in size due to the cuts of crystals. However, the mechanical quality factor and stability of quartz crystals are relatively higher than ceramics. Therefore quartz crystals are always used in high-frequency filters, transducers, and other standard frequency controlling oscillators. Besides the quartz crystals, the high-quality perovskite piezoelectric single crystals such as the $Pb(A_{1/3}B_{2/3})O_3$–$PbTiO_3$ ($A = Zn^{2+}$, $Mg^{2+}$; $B = Nb^{5+}$) with much higher piezoelectric constant ($d_{33} \sim 2600$ pC/N), electromechanical coupling coefficient ($k_{33} \sim 0.95$), and strain (>1.7%) have also been obtained since 1997. These single crystals are new-generation piezoelectric materials for high-performance piezoelectric devices and systems including ultrasound medical imaging probes, sonars for underwater communications, and sensors/actuators. However, the size and shape of the piezoelectric single crystals are difficult to be preciously controlled during the growth process, which limit the practical application in many fields such as the microscaled actuators and composite metamaterials (Wang et al. 2014).

Furthermore, the piezoelectric polymers such as polyvinylidene fluoride (PVDF) possess high flexibility, low density, and resistance as well as relatively higher piezoelectricity voltage constant ($g$). Unlike the piezoelectric ceramic and crystals, the intertwined long-chain molecules in polymers attract and repel each other when an electric field is applied. PVDF has exhibited great potential in the application of acoustic ultrasound measurements, pressure sensors, and ignition/detonations. However, the relatively low piezoelectric strain constant ($d$) of PVDF limited the application in transducers (Wang et al. 2015a, b).

Piezocomposite materials are an important update of existing piezoceramic. They can be (a) piezo-polymer in which the piezoelectric material is immersed in an electrically passive matrix (for instance, PZT in epoxy matrix); and (b) piezocomposites that are composite materials made by two different ceramics (for example, $BaTiO_3$ fibers reinforcing a PZT matrix) (Dineva et al. 2014). In addition, composite piezoelectric rubber has been developed through composite polymeric and metallic microstructures with embedded bipolar charges. For instance, multilayer PDMS cellular structures coated with PTFE films and stretchable gold electrodes are fabricated and implanted with bipolar charges. The composite structures show elasticity of 300–600 kPa and extreme piezoelectricity of $d_{33} > 2000$ pC/N and $d_{31} > 200$ pC/N. For a working volume of 2.5 cm × 2.5 cm × 0.3 mm, 10% (or 2.5 mm) stretch results in effective $d_{31}$ of >17,000 pC/N. It is estimated that electric charge of >0.2 μC can be collected and stored per breath (or 2.5 cm deformation) with this kind of composite piezoelectric rubber bands (with spring constants of ~200 N/m). They can be mounted on elastic

waistbands to harvest the circumferential stretch during breathing, or on pads around joints to harvest the elongation during limb motion.

Furthermore, the wearable piezoelectric structures can be spread, stacked, and connected to charge energy storages and power micro devices (Wang et al. 2014).

As a result, piezoelectric materials have been widely used in the industrial, manufacturing, automotive industry, and medical instruments as well as information and telecommunication fields, and so forth. According to the operation mode of the piezoelectric devices, the application of piezoelectric materials can be classified as follows (Wang et al. 2015a, b; Priya et al. 2017):

(a) Sensors.
Through the direct piezoelectric effect, the piezoelectric materials can be used for the detection of pressure variations in longitudinal, transversal, and shear modes. The most commonly used application of piezoelectric sensors is in the sound form, such as the piezoelectric microphones, piezoelectric pickups in acoustic-electric guitars, and detection of sonar waves. Moreover, the piezoelectric sensors can also be used with high-frequency field such as the ultrasonic medical imaging or industrial nondestructive testing. In addition, the piezoelectric sensors were also employed in piezoelectric microbalance and strain gauges.

(b) Actuators.
On contrary to piezoelectric sensors, the working of actuators is usually based on the reverse piezoelectric effect to induce tiny changes in the width of the piezoelectric materials by applying high electric fields. Due to the relatively high precision of the width changes, the piezoelectric actuators are always used in accurate positioning. For example, the piezoelectric motors with high accuracy have already been used in optical devices, transportation and aerospace techniques, robots, medical devices, biology, and nanomanipulation fields, such as the atomic force microscopes (AFM), scanning tunneling microscopes (STM), autofocusing camera lens, inkjet printers, CT/MRI scanners, and X-ray shutters.

(c) Frequency Controlling Devices.
Crystal oscillator is an electronic oscillator circuit that uses the mechanical resonance of a vibrating piezoelectric crystal to create an electrical signal with a very precise frequency. The frequency can be used to provide a stable clock signal for digital integrated circuits. Moreover, the piezoelectric materials have also been used in high-frequency resonators and filters, such as the surface acoustic wave devices and film bulk acoustic resonators.

(d) High voltage and power sources trough energy harvesting.
By applying the external mechanical stimulates, the piezoelectric ceramic or crystals can generate potential differences with thousands of volts in amplitude. Therefore, piezoelectric materials can be used as high voltage and power sources. The most commonly application is the piezoelectric ignition/sparkers such as the cigarette lighters. Moreover, the piezoelectric materials have been employed for energy-harvesting applications. Table 11.2 shows some of the common sources of mechanical energy that can be harnessed through

**Table 11.2** Sources of energy available in the surrounding which are/can be tapped for generating electricity (Priya et al. 2017)

| Human body | Vehicles | Structures | Industrial | Environment |
|---|---|---|---|---|
| Breathing, blood pressure, exhalation, body heat | Aircraft, UAV, helicopter, automobiles, trains | Bridges, roads, tunnels, farm house structures | Motors, compressors, chillers, pumps, fans | Wind, solar, temperature gradient, daily temperature |
| Walking, arm motion, finger motion, jogging, swimming, eating, talking | Tires, tracks, peddles, brakes, shock absorbers, turbines | Control-switch, HVAC systems, ducts, cleaners, etc. | Conveyors, cutting and dicing, vibrating mach. | Ocean currents, acoustic waves, EM waves, RF signal |

piezoelectrics. For example, the energy from human movements and vehicle movements in public places can be harvested and converted into electricity for lighting the lamps. Recently, the microscale energy harvesters were developed for harvesting the small scale mechanical energies by using the piezoelectric nanomaterials, which is called "piezoelectric nanogenerators." The nanogenerators can be used for charging the batteries or directly driving some low-power microdevices.

### 11.3.3 Advances in Piezoelectric Energy Harvesting

Piezoelectric energy harvesters can be categorized by the targeted energy sources, such as ambient vibrations, impact or shock stress, fluid flow, and human motion. Regardless of the various energy sources, the basic working principle is the same—the environment applies a stress on piezoelectric material and by the direct piezoelectric effect, the input mechanical energy is converted in to electrical energy. Piezoelectric generators produce high voltages and low currents, and require no voltage source to operate. Piezoelectric energy harvesters generally have bimorph or unimorph cantilever beam structures (Fig. 11.6a, b). In addition, MEMS technologies have been applied towards the development of integrated energy harvesters, and many piezoelectric MEMS energy harvesters have been developed. At the MEMS-scale, bimorph cantilever are less manufacturable with existing microfabrication processes. As a result, MEMS cantilevers mostly have a unimorph configuration. A seismic mass is usually attached at the tip of the cantilever to adjust the resonant frequency to the available environmental frequency, normally below 100 Hz. As shown in Fig. 11.6c, two piezoelectric modes, $d_{31}$ or $d_{33}$, are commonly used in piezoelectric micro devices. The relative directions of the electric field and the strain distinguish them: $d_{31}$ when the electric field is perpendicular to the input strain, $d_{33}$ when they are parallel. Conventional MEMS piezoelectric devices/actuators have $d_{31}$ configuration in which a piezoelectric layer is sandwiched between top and bottom electrodes (Priya et al. 2017).

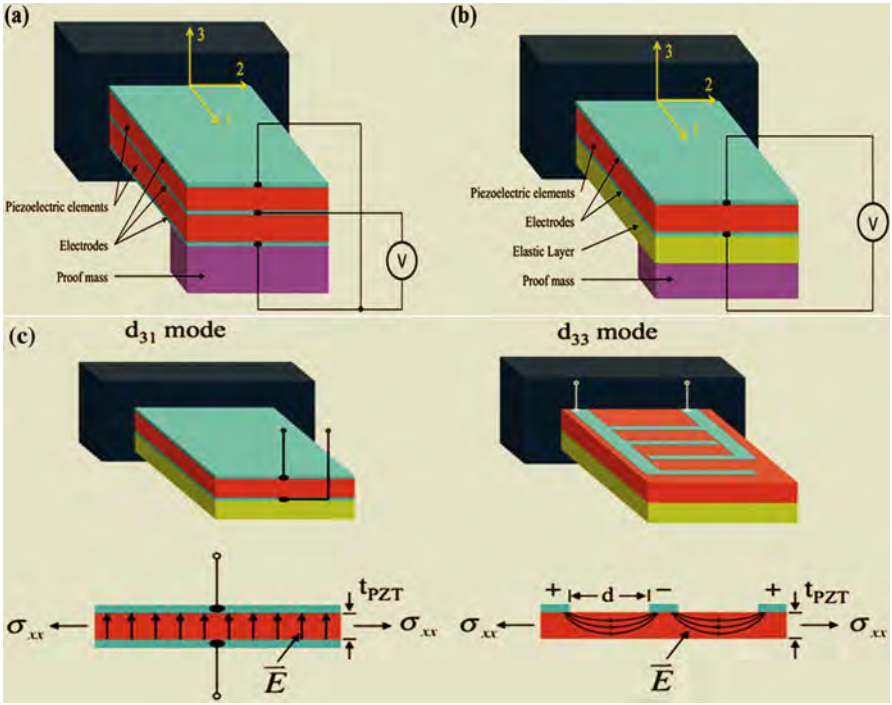


**Fig. 11.6** Basic structure of piezoelectric energy harvesters: (**a**) Bimorph structure, (**b**) unimorph structure, and (**c**) two modes of piezoelectric conversion of input mechanical strain depending on the relative direction of the stress $\sigma$xx (or strain) and the electric field, E (Adapted with permission from Priya et al. (2017) (Walter De Gruyter and Company))

#### 11.3.3.1 Grain Textured and Epitaxial Piezoelectric Films

Bulk PZT ceramics have plethora of dielectric and piezoelectric properties which can be controlled using doping. Lead-based relaxor-lead titanate compounds so-called relaxor ferroelectrics include $Pb(Zn_{1/3}Nb_{2/3})O_3$–$PbTiO_3$(PZN–PT), $Pb(Mg_{1/3}Nb_{2/3})O_3$–$PbTiO_3$(PMN–PT), and $Pb(Y_{½}\ Nb_{1/2})O_3$–$PbTiO_3$(PYN–PT) and exhibit large electromechanical coupling coefficients which makes these materials more attractive option for microactuator and micro-sensor applications. For device miniaturization it is important to grow films using these materials. PZT thin films are deposited with variety of methods such as sputtering, chemical solution deposition (i.e., sol-gel), MOCVD, and laser ablation processes. Since piezoelectric properties of these materials are strongly dependent on film quality and growth orientation, thus, the control of growth orientation is highly desired with (001) texturing. Additionally, the composition of the piezoelectric material plays a crucial role in deciding the piezoelectric properties of films. The most simple and direct solution towards enhancing the output power at the fixed size of a device is to increase the piezoelectric and electromechanical coupling coefficient. Grain texturing has been shown to be an effective method for improving the magnitude of physical constants in piezoelectrics

by achieving a domain engineered state. In the vicinity of the morphotropic phase boundary (MPB), a rhombohedral composition oriented along the <100> direction is known to exhibit optimum magnitudes of electromechanical coefficients. In addition, the piezoelectric properties can be tuned through interfacial stress. For instance, ~90% enhancement of ferroelectric and piezoelectric properties in MPB composition PZT thick films by tailoring the magnitude of residual stress by choosing substrates with different coefficients of thermal expansion. The enhanced piezoelectric properties were attributed to the fact that the c-domains parallel to the thickness direction were easy to form under in-plane compressive stress. This technique of inducing a compressive stress in the films is quite appealing, as it can be easily implemented in the fabrication of MEMS components (Kim et al. 2012; Priya et al. 2017).

Epitaxial PZT thin films with c -axis orientation are also ideal materials for MEMS energy harvesters because the c -axis orientation of the tetragonal PZT results in large piezoelectric properties and a low dielectric constant. However, epitaxial substrates, such as MgO and $SrTiO_3$, are usually not suitable for unimorph cantilevers because of their brittleness and difficulty of microfabrication. One solution is to transfer the epitaxial PZT films onto flexible cantilevers, made with polymer, stainless steel or Ni foils, etc. (Kim et al. 2012).

Figure 11.7 shows fabrication process of high-efficiency piezoelectric energy harvesters using c-axis oriented PZT thin films by radio-frequency (RF)- sputtering, which were transferred onto stainless steel (Morimoto et al. 2010). The c-axis oriented PZT thin films were grown on (100) MgO single crystals with an epitaxial (001) Pt bottom electrodes. Reciprocal lattice space maps before and after transfer process clearly showed spotty diffractions of the (204) PZT, indicating that the transfer process did not degrade the crystal structure of the epitaxial PZT film. After the PZT film was bonded to 50-μm-thick stainless steel sheets with epoxy resin, the MgO substrate was etched out in phosphoric acid. The relative dielectric constant $\varepsilon_r$ of the transferred films on stainless steel was as low as 166, while the piezoelectric coefficients $e_{31,f}$ of the transferred PZT films was around $-6$ C/m$^2$. The thickness and length of stainless steel cantilever was 50 μm and 18.5 mm, respectively. Because of the thin dimension of the metal cantilever, the first resonance was found to occur at 126 Hz. The maximum output electric power of 5.3 μW was obtained across a load resistance of 50 kΩ. The output power increases monotonically with the acceleration, reaching 244 μW at 50 m/s$^2$. The flexible metal cantilever enables considerable reduction of the resonant frequency and offers enhanced toughness compared with brittle Si-based cantilevers (Priya et al. 2017).

In addition, relaxor ferroelectric single crystals, such as PMN-PT and PZN-PT, show about ten times larger piezoelectric coefficient than that of conventional PZT ceramics. The epitaxial PMN-PT thin films grown on $SrTiO_3$-buffered miscut Si substrate by off-axis sputtering have demonstrated excellent piezoelectric coefficient $e_{31,f}$ ($-27$ C/m$^2$). Because of the large electromechanical coupling coefficient $k_{31}$ (or figure of merit: $e_{31,f}^2/\varepsilon_r$) of PMN-PT epitaxial thin films, this system is quite

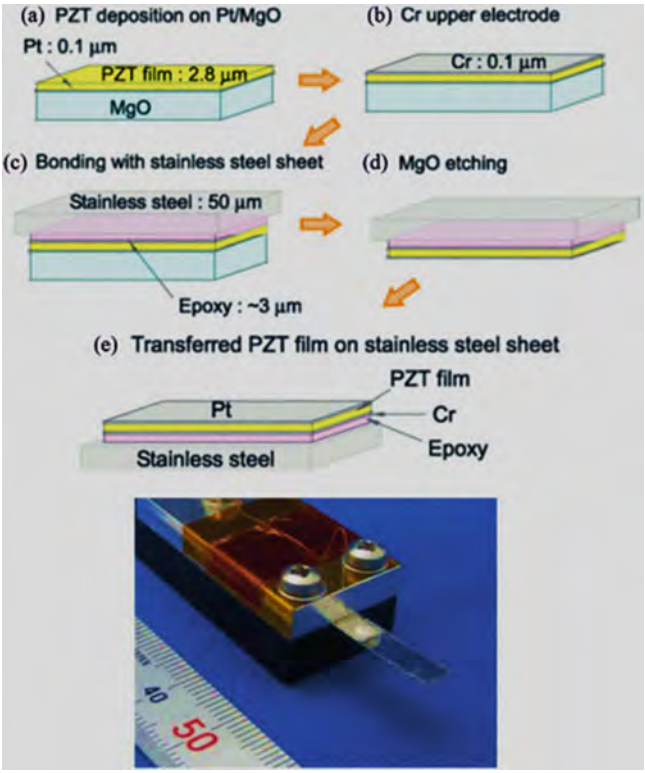


**Fig. 11.7** Fabrication process flow and photograph of transferred epitaxial PZT thin films on stainless steel cantilever (Modified with permission from Morimoto et al. (2010) (Elsevier))

promising towards improving the performance of current MEMS energy harvesters (Priya et al. 2017).

#### 11.3.3.2 Lead-Free Piezoelectric Films

For powering medical implants and human use of energy harvesters, lead-free piezoelectric material is desirable. Potassium sodium niobate ($K_xNa_{1-x}NbO_3$), abbreviated as KNN, is considered as a most promising lead-free piezoelectric material owing to its higher Curie temperature and higher ferroelectric orthorhombic—ferroelectric tetragonal transition temperature. The piezoelectric properties of KNN-based compositions are directly correlated to the fraction of orthorhombic (O) and tetragonal (T) phase as shown in Fig. 11.8a. One of the strategies for achieving higher piezoelectric response has been to modulate the composition such that O/T transition lies close to room temperature. Another strategy adopted for designing lead-free compositions is based upon the trend between atomic weight ratio of A to B sites ($R_w = W_a/W_b$) and longitudinal piezoelectric constant $d_{33}$ as shown in Fig. 11.8b. It can be observed that $1/R_w$ for KNN ceramics (for Na/K ratio of 0.5) is similar to $R_w$ for PZT ceramics at MPB composition and both of these

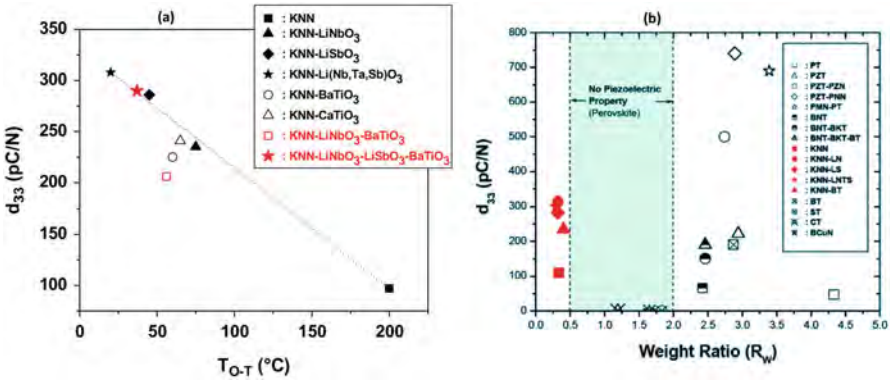


**Fig. 11.8** Lead-free piezoelectric films (Modified with permission from Priya et al. (2017) (Walter De Gruyter and Company)): (**a**) Variation of longitudinal piezoelectric coefficient with O–T transition temperature in KNN system, and (**b**) variation of longitudinal piezoelectric coefficient as a function of weight ratio in bulk perovskites

materials exhibit high piezoelectric response. Piezoelectric compositions show large response when RW for A-site heavy perovskites and $1/R_w$ for B-site heavy perovskites is higher than 2.0 (Ahn et al. 2009; Priya et al. 2017).

The fabrication process of these lead-free piezoelectric materials in thin-film form is still under development, and it is expected that these materials will be utilized in the design of MEMS energy harvesters in the near future. For instance, KNN thin films deposited by RF magnetron sputtering showed large transverse piezoelectric properties comparable to those of PZT thin films (Shibata et al. 2011). Because KNN and PZT thin films have almost same dielectric and piezoelectric properties, the KNN film performs comparably to the PZT film with respect to power generation (Priya et al. 2017).

#### 11.3.3.3 Aluminum Nitride (AlN) as a MEMS Compatible Piezoelectric Films

AlN is a piezoelectric material with wurtzite structure. The properties of AlN-based films are highly process dependent. Aluminum nitride has a band gap of 6.2 eV with lattice parameter of $a = 13.112$ Å and $c = 4.982$ Å. It is a potential candidate for UV light emission and SAW devices due to large acoustic wave (SAW) velocity. AlN films have been deposited using chemical vapor deposition (CVD), plasma assisted CVD, metalorganic CVD, reactive DC-magnetron sputtering, plasma assisted molecular beam epitaxy (MBE), laser-induced chemical vapor deposition, and pulsed laser deposition. Most of these techniques required a high processing temperature (1000 °C) to obtain the best crystal quality and texture in the deposited thin films. However, high-quality growth at low temperature is desired to ensure the compatibility with IC technology. In this regard, different process techniques have been developed. In addition to (0001)–orientation, it is also observed that tuning of the ion energy and flux of the bombarding ions ($Ar^+$, $N^{2+}$) is equally important. AlN films have a much higher phase velocity and chemical stability in comparison to the

ZnO films. However, AlN has lower piezoelectric coupling and it is difficult to control the growth of AlN films. Even though, significant progress has been made towards incorporating the AlN films in energy-harvesting applications with compatible CMOS process, such as micomachined AlN cantilevers (Kim et al. 2012), [001] textured AlN cantilevers (Priya et al. 2017), corrugated AIN cantilever structures (Ting-Ta et al. 2011), AlN thin film based MEMS energy harvester with high power density (Andosca et al. 2012). Since the Young's modulus of AIN (345 GPa) is about four times that of PZT, the thickness of AIN for maximum power output is about three times smaller than that of PZT (Priya et al. 2017).

#### 11.3.3.4 Piezoelectric Thick Films by Powder/Granule Spray in Vacuum Process

The powder spray in vacuum process so-called aerosol deposition (AD) is a unique ceramic film deposition technology that is able to fabricate highly dense thick films (submicron to several hundred μm) at room temperature. This process utilizes high kinetic energy of ejected aerosol consisting of a mixture of fine ceramic particles and carrier gas from a nozzle. The process has unique advantages compared to other thin/thick film deposition processes such as high deposition rate (over several tens μm/min depending on the deposition area), low processing temperature, composition control, high adhesion strength between substrate and film, as well as micropatterning of ceramic thick films during deposition (Zhou et al. 2011).

Due to its low temperature processing, low sinterability ceramic thick films such as KNN-based lead-free piezoelectrics and $PbTiO_3$ ceramics with full density can be deposited on various types of substrates. Figure 11.9 shows ferroelectric/piezoelectric property modulation of AD-PZT film according to the variation of residual stress level. By generating high compressive residual stress in the PZT thick films, the piezoelectric properties can be enhanced by ~2 times. All these advantages are highly attractive for MEMS-based piezoelectric device applications. In addition, optimization of deposition rate and uniformity in large area films have been conducted by the granule spray in vacuum process (GSV). Figure 11.10 shows the typical microstructure of patterned highly dense PZT thick films for MEMS ultrasonic transducers by GSV. The deposition rate of the PZT thick film by GSV was 1.4 μm/min in the area of 1440 $cm^3$. That is over two orders of faster rate than that of the other thin film processes. The film was very uniform. Directly patterned highly dense 11 μm thick PZT film was fabricated on 6 in. (152.4 mm) $Si/SiO_2/Ti/Pt$ wafer by GSV, and the films were not damaged during post processes including back-DRIE process (Priya et al. 2017).

#### 11.3.3.5 Nonlinear Resonance-Based Energy-Harvesting Structures

Most of the vibration energy harvesters usually use a linear cantilever resonator structure to amplify small ambient vibration. While such structures are easy to model, design, and build, they typically have a narrow bandwidth. In contrast, nonlinear resonators have different dynamic response and greatly increase the bandwidth by hardening or softening the resonance characteristic of the beam structure. In addition, it has been found that nonlinear resonating beams can extract

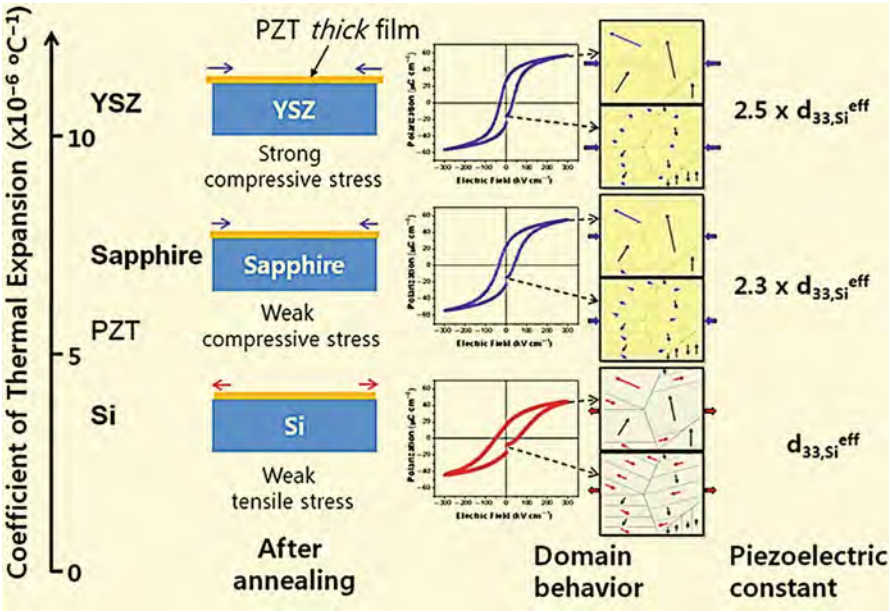


**Fig. 11.9** Conceptual diagram of high piezoelectric performance in PZT thick films grown on various substrates; the stresses were controlled by the thermal expansion mismatch between substrates and PZT films (Adapted from Han et al. (2011) (AIP Publishing), used in accordance with the Creative Commons Attribution (CC BY) license (https://creativecommons.org/licenses/by/4.0/).)

more electrical energy than that of linear resonating beams when external vibration source has variable frequency. Nonlinearity may come from magnetic force or constrained mechanical structures. The magnetic forces between the magnets and the iron create a nonlinear spring, whose nonlinearity is determined by the strength of the magnets and the size of the air gap between the magnets and the iron stator. Due to the mutual attractions, the ferromagnetic beam has three equilibrium positions (statically bistable configuration), and the vibration mode has the form of the bistable Duffing resonance. Electromagnetic energy harvesters have shown hardening or softening resonance characteristics. However, magnet-based beams require assembly of hard magnets, which is expected to be costly as the size of the device shrinks (Priya et al. 2017).

Nonlinear resonance could be better achieved by a monolithically fabricated MEMS structures. Efforts have been made to achieve wide bandwidth piezoelectric energy harvester by exerting an axial compression and forming a buckled configuration, to make a bistable oscillator. Moreover, a monolithic MEMS-based nonlinear resonant piezoelectric micro energy harvester has achieved an ultra-wide bandwidth of >>20% of the center frequency and generated power more than 22 μW (Hajati and Kim 2011). Unlike a linear resonance system, where the electrical damping cannot exceed the mechanical damping, it has been shown that electrical damping in a nonlinear resonance system could surpass the mechanical damping, extracting much higher output power than that of the linear systems. The nonlinear impedance serves

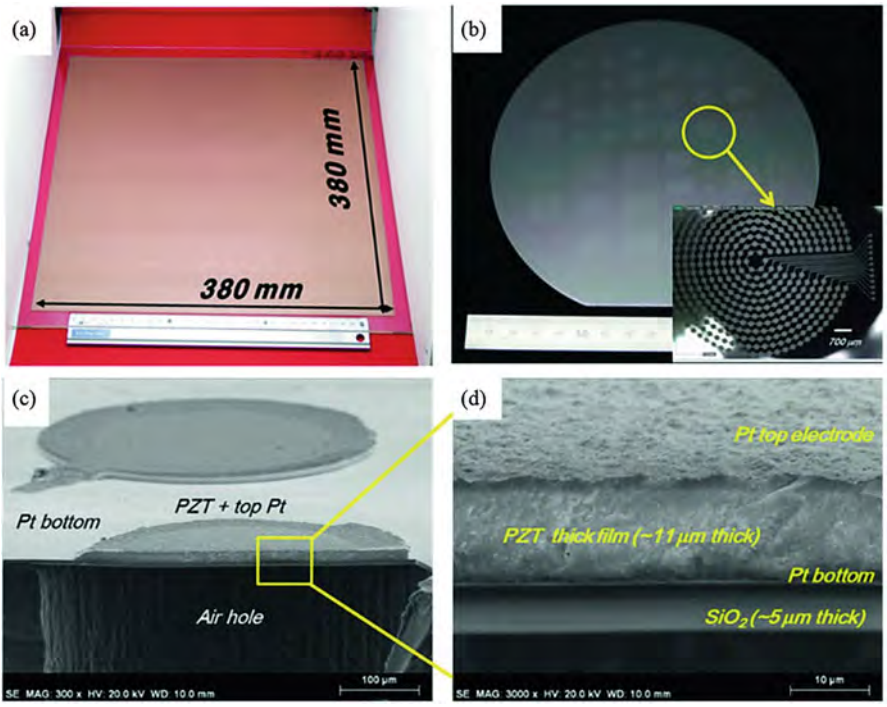


**Fig. 11.10** Typical microstructure of patterned highly dense PZT thick films for MEMS ultrasonic transducers by GSV (Adapted with permission from Priya et al. (2017) (Walter De Gruyter and Company)): (**a**) Large area PZT deposition by GSV process. (**b**) 6 in. Si/$SiO_2$/Ti/Pt wafer with directly patterned PZT thick film. (**c**, **d**) Cross-sectional SEM micrographs of piezoelectric MEMS ultrasonic device by GSV

as a negative feedback and stabilizes the deflection when the electrical damping changes. This is why the power bandwidth of nonlinear systems can be much wider than that of linear systems at equivalent beam dimensions (Priya et al. 2017).

Bistable nonlinear resonant beams not only widen the power bandwidth but also lower the working frequency range and input vibration amplitude of energy harvesters. Electromechanical lumped model predicts both stiffening and softening frequency responses for the inter-well and intra-well oscillations of bistable systems. The softening frequency response generates much higher power than mono-stable configuration at lower frequencies, providing opportunity for MEMS harvesters to be operated at low frequency and low g input vibrations. With MEMS-scale multi-layer buckled plate, at least 50 μW power could be generated below 100 Hz frequency and 0.2 g acceleration (Fig. 11.11). The presence of nonlinearity based on magnetic interaction or buckled beams has a significant influence on the performance of energy harvesters. The bandwidth of nonlinear energy harvester was increased by bistable effect; however, it is obvious that the frequency response to input vibration was more complicated as compared to linear case. The instability of frequency response makes it difficult to precisely modulate the bandwidth and tune

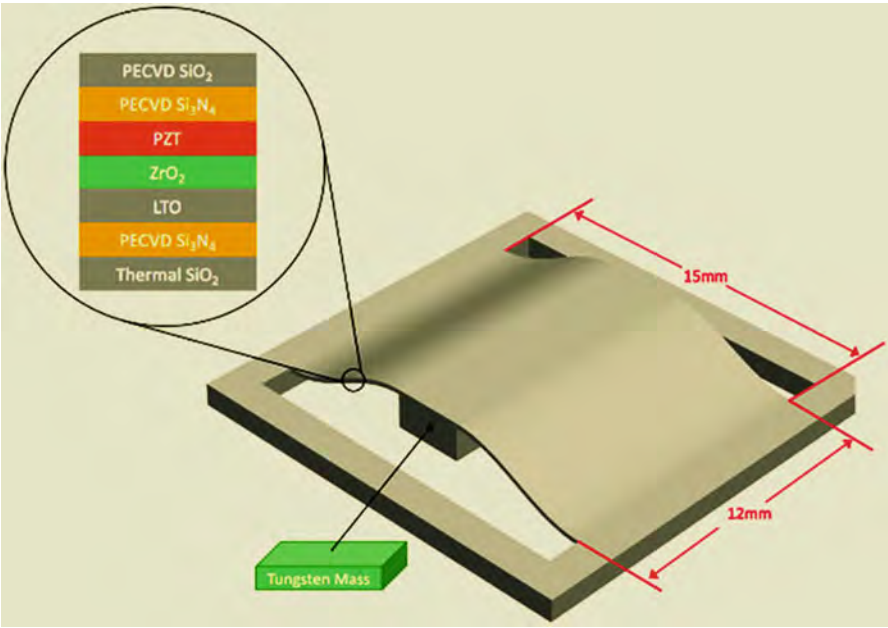


**Fig. 11.11** Schematic view of a bistable beam energy harvester (Modified from Xu and Kim (2015) (IOP Publishing), used under the terms of the Creative Commons Attribution 3.0 license)

the resonance frequency of the energy harvester in realistic environment. Therefore, although nonlinearity can provide a solution for widening the bandwidth, it will require additional control features to exploit the enhancement in the output power (Xu and Kim 2015; Priya et al. 2017).

#### 11.3.3.6 Low-Frequency Energy-Harvesting Structures

Microscale low-frequency energy harvester has been mainly dominated by inductive or electromagnetic devices. However, the miniaturization of such devices is limited by the size of the magnet used as the inertial mass and the size of the coil that can be fabricated on the MEMS scale. Consequently, for MEMS scale energy harvester, piezoelectricity is the transduction of choice and especially due to its compatibility with cleanroom-based silicon micromachining techniques. At mm-scale, piezoelectric mechanism provides the best output power density at low frequencies as compared to other possible mechanisms for vibration EH. However, piezoelectric-based energy harvester presents a fundamental challenge at the small dimensions since the resonance frequency of the structure increases (kHz range) as the dimension decreases. This challenge should be overcome in order to become compatible with the practical applications.

The most commonly used approach for reducing the natural frequency involves the addition of a large inertial tip mass to the free end of a simple single cantilever beam structures. Other methods involve the use of increased effective surface area cantilevers such as spirals (Deterre et al. 2013; Priya et al. 2017).

The use of tip masses severely affects the structural integrity and durability of the harvesters while the increased effective surface area designs exhibit torsion (causing voltage cancellation effect) in the very important first vibration mode. Therefore, it is of great importance to create a more effective method by developing uniquely shaped cantilevers, such as arc-based cantilevers which exhibit low natural frequencies; circular Zigzag structure that permits inertial mass free attainment of low frequencies. In addition, a set of new tip mass free vibration energy structures have been developed, which are capable of attaining resonant frequency of less than 100 Hz with less torsion than spiral designs and with a smaller foot print than zigzag or meandering structures, as shown in Fig. 11.12 (Varghese 2013; Apo 2014). This design, termed as arc-based cantilever (ABC), has achieved <100 Hz resonant operation both on the Si MEMS platform and with bulk piezo material as compared to traditional cantilevers. The arc-based cantilever is a continuous cantilever that can be divided into purely circular arc segments, thereby making it a low-frequency structure with dominant bending characteristic in the first (or fundamental) frequency mode. As shown in Fig. 11.12a, two arc-based micro-cantilevers (S-shaped, C-shaped) were designed based on the well-known linear configurations (simple and zigzag.) In addition to the metal micromilling (Fig. 11.12b) such structures were also fabricated and demonstrated using a silicon micromachining

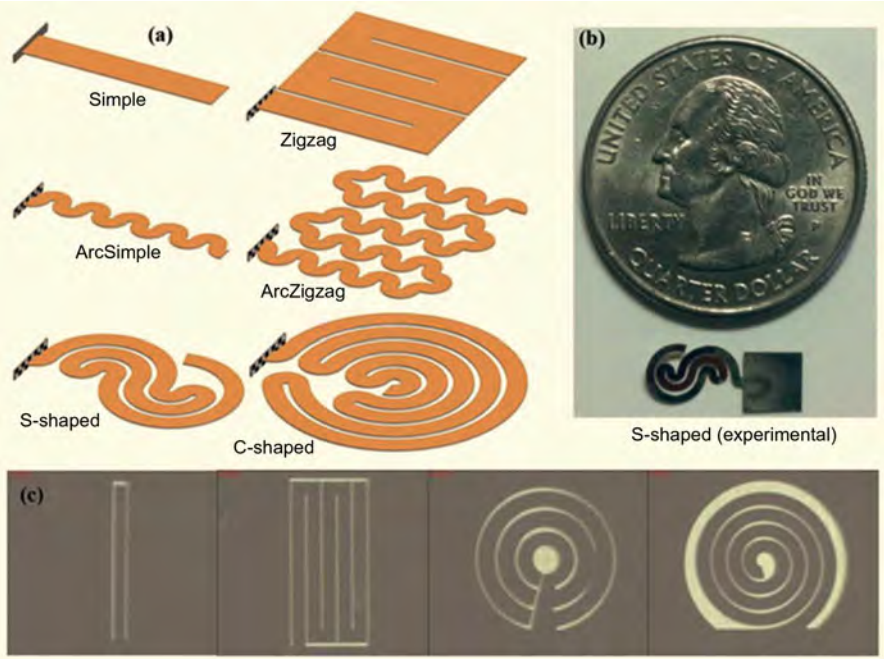


**Fig. 11.12** Arc-based microcantilevers (Adapted with permission from Priya et al. (2017) (Walter De Gruyter and Company)): (**a**) Design development of the cantilevers, (**b**) micromilled S-shaped cantilevers, (**c**) as fabricated silicon MEMS cantilever structures

process (Fig. 11.12c). All the arc-based cantilevers were shown to resonate below 100 Hz and they exhibited dominant bending behavior in the fundamental mode. These designs therefore provide a foundation for the development of standalone arc-based micro-cantilevers which can be used for energy harvesting, actuation, and sensing applications (Priya et al. 2017).

#### 11.3.3.7 Flexible and Stretchable Piezoelectric Devices

Advances in fabrication techniques and device designs, together with the emergence of high-performance inorganic piezoelectric materials enable the construction of piezoelectric devices in formats that are thin, flexible, and, in some cases, mechanically stretchable. The results allow straightforward miniaturization of lightweight, compliant electromechanical systems suitable for mounting on nearly any type of surface, with performance characteristics that can match those of conventional, rigid devices. Such technologies leverage the ability of piezoelectric materials to interconvert mechanical and electrical forms of energy. Electrical power can be generated from vibrations associated with operating machinery, movements of the human body, and environmental sources, such as waves, wind, and others. Similarly, application of electric fields to piezoelectric materials yields well-controlled mechanical forces for actuation in robotics, biomedical devices, and metrology tools. These dual functions in piezoelectrics, together with an increasingly broad set of material choices and device designs, provide the basis for diverse applications in biomedicine, defense technology, nano-devices, microelectromechanical systems (MEMS), personal electronics, and mechanical energy harvesters (MEHs). Figure 11.13 summarizes a range of examples, achieved in some cases by using nanoscale inorganics and in others with emerging classes of organic piezoelectrics (Wang 2008; Dagdeviren et al. 2016).

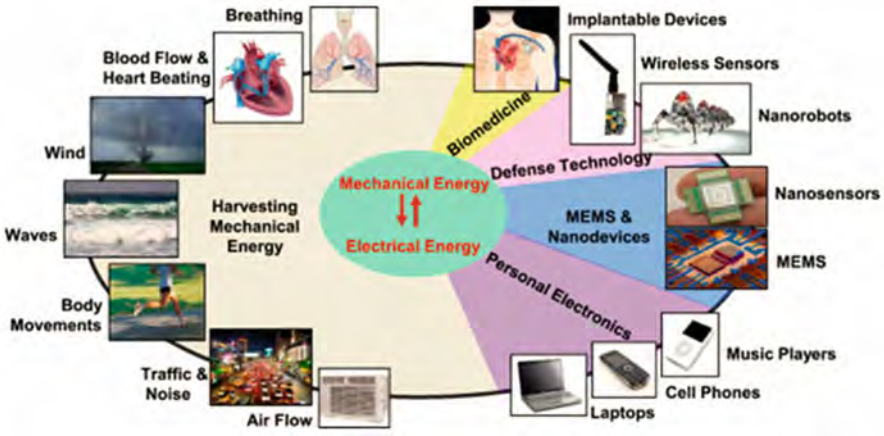


**Fig. 11.13** Possible sources of energy for harvesting (left) and opportunities use of this energy in sensing and actuation (right) that can be considered for flexible/bendable piezoelectric devices (Adapted with permission from Wang (2008) (John Wiley and Sons))

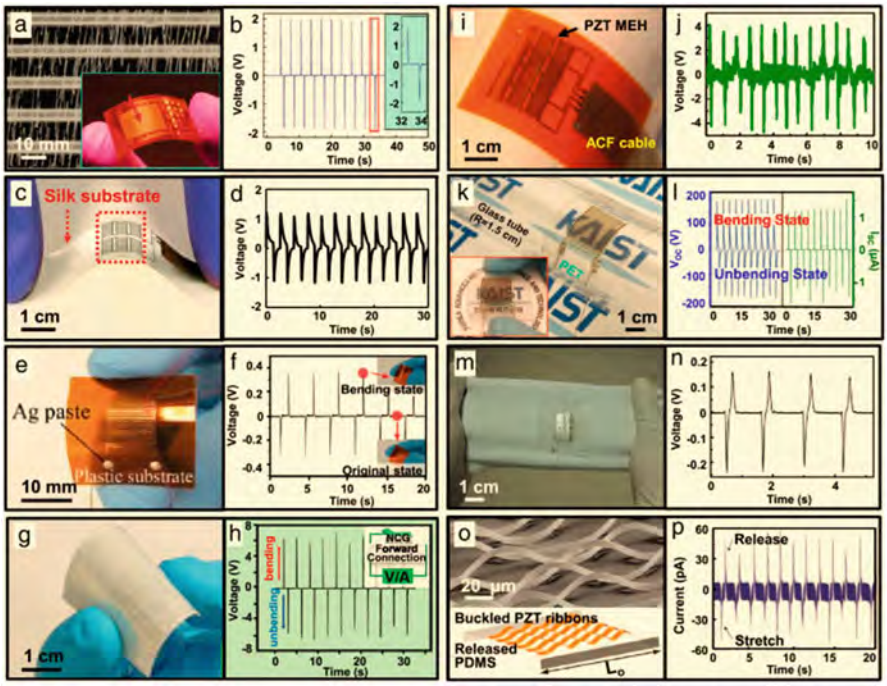


**Fig. 11.14** Flexible and stretchable MEHs with various piezoelectric materials (Adapted with permission from Dagdeviren et al. (2016) (Elsevier)): (**a**) SEM image of horizontally aligned ZnO NWs on a plastic substrate with an inset of the resultant device. (**b**) Output voltage from a ZnO NWMEH during bending/unbending. (**c**) Photograph of a biocompatible ZnO MEH under compression. (**d**) Output voltage from a ZnO MEH during bending/unbending. (**e**) MEH based on a thin film of $BaTiO_3$. (**f**) Output voltage from a $BaTiO_3$ MEH during bending/unbending. (**g**) MEH based on nanowires of $BaTiO_3$. (**h**) Output voltage from a $BaTiO_3$ nanowire MEH during bending/unbending. (**i**) MEH based on nanoribbons of PZT. (**j**) Output voltage from a PZT nanowire MEHs during motions while mounted on a bovine right ventricle. (**k**) MEH based on a large-area, thin film of PZT released by LLO, an inset showing the resultant device manually bent. (**l**) Output voltage from a LLO-transferred thin-film PZT MEH during bending/unbending. (**m**) MEH formed using textile-based PZT. (**n**) Output voltage from a textile-based PZT MEH under the stretching and releasing motions. (**o**) SEM image (top) and schematic diagram (bottom) of a stretchable MEH based on wavy PZT nanoribbons. (**p**) Output current of a stretchable, PZT-based MEH under stretching motions

Among the many applications for piezoelectric technologies, those that involve interfaces with the human body represent an area of rapid development. Inorganic piezoelectric materials, appropriately configured into flexible/stretchable formats, are preferred due to their high piezoelectric coefficients. Figure 11.14 shows a range of different types of devices capable of harnessing electrical energy from mechanical energy resources each with potential applications in biomedicine. Classes of biointegrated, flexible mechanical energy harvesters involve ZnO, as nanoscale effect on ZnO NWs enhances the effective piezoelectric constant compared to that of bulk forms and provides flexibility to the MEH structure. Images associated with a

device that incorporates horizontally aligned ZnO NWs appear in Fig. 11.14a. Under alternating bending/unbending motions with peak strains of 0.1% and strain rates of 5% $s^{-1}$, devices with active areas of 1 $cm^2$ generate peak voltages of ~2.0 V (Fig. 11.14b) and currents of ~100 nA, sufficient to operate a commercial LED. ZnO is particularly unique because it dissolves in biofluids, with biocompatible end products. As a result, the devices based on ZnO film built with other bioresorbable materials such as magnesium for the electrodes and interconnects, and silk fibroin for the substrates yield completely bioresorbable devices (Fig. 11.14c). Examples include devices with areas of 1 × 2.5 $cm^2$ that are capable of generating voltages and currents of 1.14 V (Fig. 11.14d) and 0.55 nA, respectively, under a peak strain of 0.056%. Envisioned uses are in biodegradable electronic implants for internal wound care, pain management, temporary cardiac pacing, and others. By comparison to ZnO, perovskite piezoelectric materials such as $BaTiO_3$ are appealing due to their higher piezoelectric constants. The use of soft lithography and transfer printing techniques facilitate the integration of $BaTiO_3$ MEHs into thin film formats on substrates of interest, as shown in Fig. 11.14e. In this configuration, the MEHs (areas of 1 $cm^2$) are flexible while maintaining their high piezoelectric properties and are capable of generating peak output voltages and currents of 0.4 V (Fig. 11.14f) and 12 nA, respectively, under peak strains of 0.55% and strain rates of 1.6% $s^{-1}$. Another example involves the incorporation of $BaTiO_3$ NWs synthesized via hydrothermal methods into PDMS (Fig. 11.14g). Here, increasing the NW composition (greater than 20 wt.%) degrades the electromechanical coupling and leads to low output voltages. With an optimum amount (20 wt.%) of NWs and an area of 3 × 4 $cm^2$, this type of MEH can achieve peak output voltages of 7.0 V (Fig. 11.14h) and currents of 360 nA under peak strains of 0.33%. PZT is another perovskite material, of interest due to its high piezoelectric constant. Flexible devices that use arrays of PZT nanoribbons in optimized architectures for deployment on large-scale animal models (e.g., cow, sheep, and pig) provide sources of electrical power for implants such as cardiac pacemakers. MEHs with areas of 2 × 2.5 $cm^2$ mounted onto epicardial sites of the beating heart of a bovine (cow) model are shown in Fig. 11.14i. Here, the value of h and the plane-strain bending stiffness parameters are arranged in such a way to achieve high system flexibility while producing optimal amounts of electrical power. For instance, under peak strains of 0.35%, output voltages can reach ~3.7 V. Different power outputs are also observed as a result of affixing the MEH onto different locations of heart, such as the free wall, right and left ventricles, consistent with the anatomy and the nature of motions associated with beating. The open circuit voltage for the case of the right ventricle reaches ~4 V (Fig. 11.14j). A mechanically stacked collection of five such MEHs yields an average power density of 1.2 $\mu W/cm^2$, which is sufficient to operate a cardiac pacemaker. A key design consideration is that these MEHs have minimal bending stiffnesses, to minimize mechanical loads on the heart, thereby avoiding arrhythmic behaviors associated with device-induced physical constraints. Similar devices can harness mechanical energy from the natural motions of other organs, such as lung and diaphragm. Other similar in vivo experiments have also been demonstrated to capture the mechanical energy from diaphragm and heart of small

animals (i.e., rats) with ZnO NW and PMN-PT-based MEHs. Further improvements in performance are possible via the use of uniform, large-area films of PZT (Fig. 11.14k) released by laser lift-off (LLO). The LLO process minimizes the structural damage on the PZT thin film, as a result of immediate recrystallization after vaporization by laser irradiation. With device areas of $1.5 \times 1.5$ cm$^2$, the output voltages can reach ~200 V under bending deformations (peak strain of 0.386% and strain rate of 2.32% s$^{-1}$), as shown in Fig. 11.14l. Slight human finger motions, in fact, can light as many as 100 blue LEDs simultaneously. Compared to flexible platforms, stretchable mechanics can increase the breadth of options for applications, particularly in wearable devices that cover large areas of internal organs. One stretchable example employs a textile composed of PZT fibers formed by electrospinning in Fig. 11.14m. By virtue of the electrospinning process, PZT fibers have enhanced piezoelectric properties and high flexibility. In a device example with an area of $1.5 \times 0.8$ mm$^2$ stretching/releasing motions create output voltages of ~0.24 V (Fig. 11.14n) and currents of 2.5 nA. An enhanced output can be achieved by optimizing the thickness and the hardness of the PDMS, which is the interface layer that bonds the PZT textiles and the fabrics. A different stretchable platform based on PZT involves transfer printing of PZT nanoribbons-onto prestrained PDMS substrates to create wavy structures as in Fig. 11.14o. Periodic stretching/releasing motions to peak strains of 8% yield currents of ~50 pA from a system that consists of ten PZT nanoribbons (Fig. 11.14p). Here, the wavy structures not only enhance the piezoelectric constant, but they also can accommodate tensile strains that are several orders of magnitude larger than those that induce fracture in otherwise similar ribbons in flat geometries. Such systems provide promising platforms for wearable energy harvesting where reversible stretchability is essential to operation (Park et al. 2014; Dagdeviren et al. 2016).

The flexibility and/or stretchability of piezoelectric sensors and actuators afford new measurement capabilities on various curvilinear and soft surfaces. Figure 11.15a–p shows examples of piezoelectric sensors and actuators design for the skin and other tissues. In sensing modes based on the direct piezoelectric effect, such devices can detect and measure various physical deformations, ranging from those associated with touch to those induced by pulsatile blood flow. Figure 11.15a shows a flexible sensor built using arrays of ZnO NWs on ultrathin aluminum foil substrate (18 μm) to detect human eye blinking. Although the skin deformations are small, sensors ($5 \times 13$ mm$^2$) generate easily measurable voltages of 0.2 V and currents of 2 nA as seen in Fig. 11.15b. Piezoelectric materials can also be used in touch sensors, as demonstrated by devices based on ZnO NWs and a capping layer of $BaTiO_3$ (Fig. 11.15c). In this example, a single touch point-cell has an active area of $1 \times 1$ cm$^2$. The combination of these materials balances the high flexibility, modest piezoelectric constant in the ZnO NWs with the comparatively brittle, high piezoelectric performance of the $BaTiO_3$. As shown in Fig. 11.15d, the addition of $BaTiO_3$ capping layer enhances the sensitivity by increasing the signal response from 50 mV to ~3.3 V under a normal force of 17 N applied via a linear motor. In this configuration, the sensor can also differentiate forces applied by a human finger, as a flexible touch sensor. Even the small deflections of single cells can be detected,

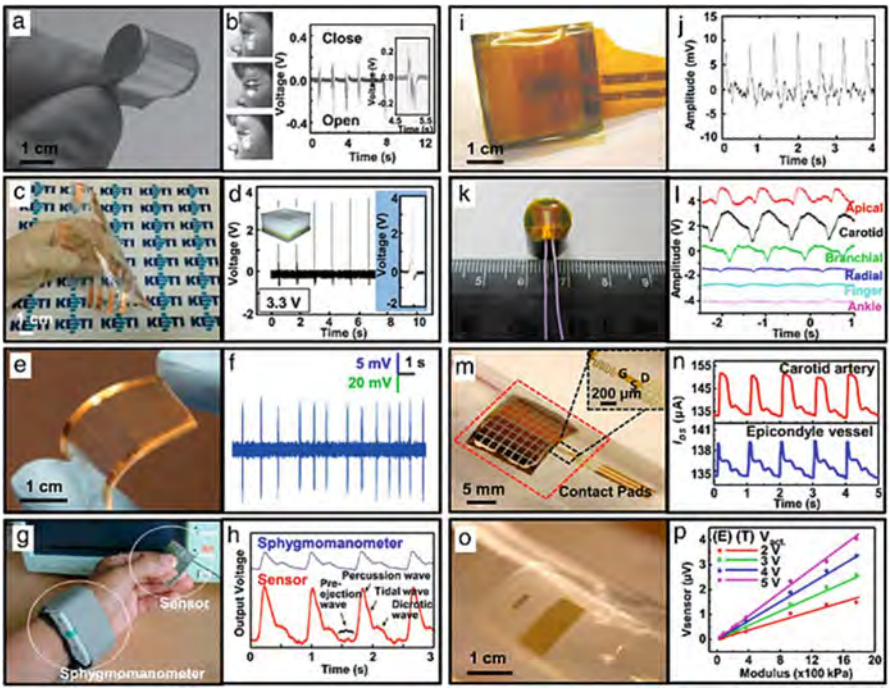


**Fig. 11.15** Various piezoelectric sensors and actuators in flexible and stretchable formats (Adapted with permission from Dagdeviren et al. (2016) (Elsevier)): (**a**) A flexible active sensor made of ZnO NW arrays grown on ultrathin aluminum foil. (**b**) Output voltage from this device, driven by the blinking of the eye. (**c**) Touch sensor based on ZnO NWs and $BaTiO_3$ capping layers. (**d**) Voltage response of the touch sensor. (**e**) A flexible PZT nanoribbon designed to monitor cellular deformations. (**f**) The corresponding voltage response of PZT nanoribbons under cellular deformation. (**g**) AlN pressure sensor and sphygmomanometer to measure blood pressure pulse waves from the wrist. (**h**) Pulse waveform signals generated using this AlN pressure sensor and sphygmomanometer. (**i**) Piezoelectric membrane sensor based on PZT. (**j**) Voltage response of the sensor attached to the wrist, measuring pressure pulse waves. (**k**) Flexible piezoelectric tactile sensor. (**l**) Diverse pulse amplitude and waveforms detected by this flexible tactile sensor at various regions of the human body. (**m**) Photograph of a PZT pressure sensor wrapped on a cylindrical glass support with an inset image of stretchable conducting traces. (**n**) Current responses measured from the carotid artery and epicondyle vessel. (**o**) Array of stretchable PZT actuators and sensors on a polymer substrate wrapped on a cylindrical glass support. (**p**) Output voltage as a function of the substrate modulus recorded at four actuation voltages

where PZT nanomaterials can capture nanoscale deflections (∼1 nm) induced by forces imparted at the cellular scale. Figure 11.15e shows PZT nanoribbons printed onto a silicone substrate (an area of ∼1 × 2.5 $cm^2$) via transfer printing. Here, a standard whole-cell patch-clamp method induced mechanical deformations in individual PC12 cells. The voltage response (∼10 mV) of a PZT sensor shown in Fig. 11.15f demonstrates the device capability in detecting cellular deformations (∼1 nm). Additional sensing modalities involve measurements of pressure pulse waveforms due to blood flow. Examples with the sensors composed of AlN film,

formed via low-temperature reactive sputtering, offer ability to detect pressures of ~0.9 kPa, well within the sensitivity of the human finger to sense texture and shape (10–40 kPa). AlN is well suited for this application because it has high thermal and chemical stabilities. Compared AlN to a commercial Sphygmomanometer, as shown in Fig. 11.15g, the pulse waveforms generated from the sensor at the fingertips, between the thumb and middle finger, are comparable to those collected at the wrist using a sphygmomanometer at a stress level of 10 kPa (Fig. 11.15h). This sensor can also detect tidal and pre-ejection waves that are critical for monitoring health and wellness. Another example uses stainless steel (SS) foil with thickness of 38 μm as the bottom electrode and substrate, with a layer of PZT (thickness of 70 μm) encapsulated with polyimide (Fig. 11.15i). The PZT film, which exhibits a piezoelectric constant ($d_{33}$) of 37 pm/V at 10 kHz, allows detection of the mechanical displacements of the skin due to blood flow to generate pulse wave signals as shown in Fig. 11.15j. In a similar example, PZT deposited onto a SS substrate by sol–gel processes with high temperature sintering (650 °C) and poling at high electric field (~0.71 MV/m) yields a sensor with useful levels of performance (Fig. 11.15k). Mounting this type of PZT sensor on a plastic element allows sensing of bio-motions of various regions of the human body, such as carotid, brachial, radical artery, finger, and ankle artery. Figure 11.15l shows the associated pressure waveforms. The use of correct sets of materials, the engineering of device layouts, the integration of required electrical components and associated serpentine conducting traces allow construction of stretchable sensors. An example is shown in Fig. 11.15m. This device consists of PZT nanoribbons with a total area of ~22 $mm^2$ and serpentine connections provides system stretchability up to 30%. This type of sensor has fast response time (~0.1 ms) and high sensitivity (~0.005 Pa), and can be applied in various ways on human subjects. In this configuration, the NMP was engineered to be closer to the middle of PZT nanoribbons to minimize the bending-induced in-plane strain. As a result, the sensor can measure pressure accurately on any body parts that have curvatures larger than a few millimeters. Additionally, the use of soft substrates enhances the mechanics due to complex and three-dimensional deformations, and result approximately in a hundred fold enhancement in the sensitivity. This high sensitivity allows use in determining PWV for arterial stiffness measurement by placing the sensors at two different locations of human body. Figure 11.15n presents some relevant data on two different sites, such as the carotid artery and epicondyle vessel, with 2-min intervals and on three different human bodies. The resulting PWV of ~5.4 $ms^{-1}$ is similar to that measured using conventional tonometry. In addition to sensing, mechanical actuation can be an important feature in biomedical devices. An example of a unique device platform includes ultrathin architectures of piezoelectric sensors and actuators, exploiting both direct and indirect piezoelectric mechanisms, combined with serpentine configurations of metal traces for electrical connections to measure the mechanical properties (e.g., elastic modulus) of soft tissues and organ systems. Figure 11.15o shows seven actuators (lateral dimensions of 200 × 1000 $\mu m^2$) and six sensors (lateral dimensions of 100 × 500 $\mu m^2$) that are made of PZT nanoribbons in capacitor type geometries sandwiched between two layers of electrodes. Here, bending onto curvy body parts

has little effect on device operation since the NMP lies close to the middle of PZT nanoribbon.

In this conformal modulus sensor (CMS) system, applying a sinusoidal voltage to an actuator mounted on the skin induces mechanical motions in the device structures and the underlying skin, which can then be detected by adjacent sensors. The voltage responses of these sensors provide information about the electromechanical coupling between the actuators and sensors, presenting ways to determine the mechanical modulus of the near surface region of the skin. The relationships between the sensor voltage output and modulus at 1 kHz can be seen in Fig. 11.15p. The results show consistent linear proportionality between the modulus values of the substrates, for values between 30 and 1800 kPa, and associated sensor output voltages under various actuation voltages. The modulus can be determined from the actuator voltage, the sensor output voltage, the material properties and geometries of the device layers. In addition, the system exhibits capabilities to detect changes in the elastic modulus of skin across the body due to dermatologic malignancies, which generally are stiffer than healthy tissues. The same system can also be used to measure the modulus values of various biological tissues, such as the heart and the lung. As existing methodologies (e.g., torsion, traction, and nanoindentation) to measure the mechanical properties of soft biological tissues are invasive and lack of microscale spatial resolution, the dual features to actuate and sense in a thin, conformal platform offer promising capabilities for fast, accurate, noninvasive diagnostics based on stiffness (i.e., human skin or other organs) (Qi et al. 2011; Dagdeviren et al. 2016).

**INDEPTH: Emerging Applications of Liquid Crystals**

Liquid crystals (LCs) have attracted intense research interest because of their orientational order, the existence of strong dipoles and easily polarizable groups, the rigidness of the long axis, anisotropic features in the structural, optical, electrical, and magnetic properties, as well as their easy response to electric, magnetic, and surface forces. LCs are ubiquitous in diverse applications, ranging from displays to electronics, sensors, lasers, and optical computing in human being daily life. For example, ferroelectric LCs that possess a variety of advantages, such as a permanent electric polarization, high flexibility, and fast response time, have been the basis for noble field effect transistors (FETs), memory cells, and optical switching device applications. In particular, among FET-based nonvolatile memory devices, the ferroelectric FET, an important type of memory cells without a storage capacitor, is significantly attractive for memory and switch applications, because of the wide range of its interesting features, including small cell size, nondestructive read-out, low-power consumption, good retention, and fast response time. Another example of emerging applications based on LCs is holography, which is an ideal technology to realize three-dimensional

(continued)

(3D) dynamic images by changing the refractive index. Moreover, arrays of carbon nanotubes (CNTs)/nanofibers have been used to locally modulate the refractive index of the LC medium at low operation voltages. In addition, it is possible to achieve technological advances and revolution into a rapidly growing multidisciplinary field involving displays, electronics, and energy harvesting to integrate displays into a self-powered system with piezoelectric power generators, for instance. In particular, ZnO nanowire-based piezoelectric power generators exhibited highly promising piezoelectric performance for a self-powered source, due to its dimensionality and piezoelectric semiconducting properties containing non-toxicity, eco-friendliness, and geometrical versatility (Sohn et al. 2014).

## 11.4 Pyroelectric Materials

Energy harvesting can give rise to self-powered, maintenance-free devices with an almost inexhaustible source of energy. Devices from the millimeter scale down to the microscale have been manufactured, with an average power in the 10 μW–10 mW range, such as piezoelectric generators, thermoelectric microgenerators, photovoltaic devices, and electromagnetic microgenerators. At small scale, pyroelectric materials are better suited for the conversion of thermal energy into electrical energy compared to thermoelectric devices, since they require temporal temperature gradient ($dT/dt$) instead of a spatial temperature gradient ($dT/dx$), which is more difficult to realize at micro/nanoscale. Many pyroelectric materials are stable up to a very high temperature (~1200 °C), which provides an advantage over thermoelectrics for harvesting energy from high-temperature sources. Furthermore, methods to convert stationary spatial gradients to transient temperature gradients facilitates development of hybrid energy harvesters based on both thermoelectric and pyroelectric effects or radiation and pyroelectric effect. In addition, devices based on pyroelectric energy harvesting require low or no maintenance since unlike piezoelectric energy-harvesting devices, they do not include any moving parts. Alongside experimental implementation and developments, different theoretical and numerical approaches have been attempted for optimization of pyroelectric energy harvesting using mass, momentum, and energy equations for guiding future experimental efforts (Lingam et al. 2013).

### 11.4.1 The Pyroelectric Effect

Pyroelectricity is defined as the temperature-dependent spontaneous polarization in certain anisotropic crystals. This effect refers to the generation of an electric current/potential in materials with non-centrosymmetric crystal structure when subjected to a

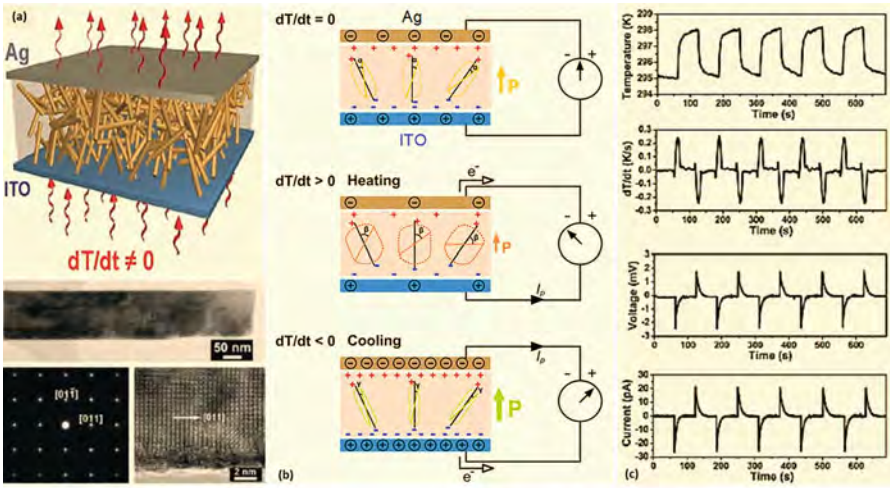


**Fig. 11.16** The mechanism of the pyroelectric nanogenerator based on the primary pyroelectric effect (Modified with permission from Wang et al. (2012) (Elsevier)): (**a**) Schematic diagram of the structure of pyroelectric nanogenerator, TEM image of a single $KNbO_3$ NW, the corresponding SAED pattern of the NW, and the corresponding HRTEM image of the NW; (**b**) schematic diagrams of the pyroelectric nanogenerator with negative electric dipoles under room temperature heated and cooled conditions. The angles marked in the diagrams represent the degrees to which the dipole would oscillate as driven by statistical thermal fluctuations; (**c**) the output voltage and current of the device under the cyclic change in temperature

temporal temperature gradient (*dT*/*dt*) (Fig. 11.16). Pyroelectricity is exhibited by crystals belonging to the polar classes 1, 2 m, 2 mm, 3, 3 m, 4, 4 mm, 6, and 6 mm. Pyroelectric materials have a unique polar axis along which spontaneous polarization exits. The unit cell of pyroelectric materials has a dipole moment, and the dipole moment per unit volume of the material is called the spontaneous polarization. A change in temperature causes the net dipole moment and hence the spontaneous polarization to change. The pyroelectric coefficient $p$ is defined as the differential change in spontaneous polarization $P$ caused by a change in temperature $T$. In the most general form, for a stress-free material in an open circuit condition, the change in polarization due to change in temperature is expressed as follows (Lingam et al. 2013):

$$\frac{\partial P_x}{\partial T} = \frac{\partial P_{x_0}}{\partial T} + \frac{\partial (d_{xkl}\sigma_{kl})}{\partial T} \tag{11.11}$$

The first term on the right-hand side of Eq. (11.11) is the permanent polarization, and the second term represents the piezoelectric-induced polarization. Change in the polarization causes change in surface-bound charges, and hence redistribution of free charges in the material to compensate for the change in surface-bound charges.

This results in a pyroelectric current flow in the external circuit. If the circuit is open, the free charges simply remain in the electrodes and an electric potential is generated. The constraints in the definition of the pyroelectric coefficient are constant electric field E and constant elastic stress $\sigma$. Constant stress means that the crystal is not clamped, but completely free to expand or contract thermally. When the crystal is rigidly clamped under constant strain $\varepsilon$, to prevent expansion or contraction, a change in temperature causes a change in electric displacement signifying the primary pyroelectric effect. The second contribution, the secondary pyroelectric effect, is a result of crystal deformation. Thermal expansion causes a strain that alters the electric displacement via a piezoelectric process. The total pyroelectric effect is the sum of the primary and secondary pyroelectric effects. The pyroelectric coefficient, $p$, can be expressed as (Lee et al. 2016):

$$p = \frac{d\rho}{dT} \tag{11.12}$$

where $\rho$ is the spontaneous polarization and $T$ is the temperature. The electric current generated by the pyroelectric effect is expressed as (Lee et al. 2016):

$$I = \frac{dQ}{dt} = \mu p A \frac{dT}{dt} \tag{11.13}$$

where $Q$ is the induced charge, $\mu$ is the absorption coefficient of radiation, $A$ is the surface area, and $dT/dt$ is the rate of temperature change. Therefore, when pyroelectric materials are heated or cooled ($dT/dt > 0$, or $dT/dt < 0$), the overall polarization in the dipole moment is decreased or increased, which causes current to flow in the circuit. Usually, ferroelectric materials such as lead zirconate titanate (PZT), $BaTiO_3$, P(VDF–TrFE), and $KNbO_3$, and some piezoelectric materials which have spontaneous polarization, such as ZnO and CdS, are used to fabricate pyroelectric generators. Coupling a pyroelectric to an external structure which undergoes large thermal deformations is also a potential approach to enhance harvested energy (Bowen et al. 2014).

In addition, tertiary pyroelectricity, due to non-uniform heating, is also possible since non-uniform heating generates shear stresses that result in polarization through the piezoelectric effect. In this case the current generated is dependent on the magnitude of the temperature gradient. Secondary and tertiary effects are therefore potential routes for enhancing thermal harvesting along with heat transfer enhancement or proper materials selection or new materials development. By harvesting the waste thermal energy, pyroelectric nanogenerators have potential applications such as environmental monitoring, temperature imaging, medical diagnostics, and personal electronics (Bowen et al. 2014; Lee et al. 2016).

### 11.4.2 Pyroelectric Materials and Selection for Energy Harvesting

Pyroelectric materials currently find widespread use in thermal detectors and sensors, where the choice of the pyroelectric material is mainly determined by figure of merit (FOM), detector size, availability, durability, environment in which the material has to operate, thermal radiation levels to be detected, purpose for which the detector is employed, maximum ambient temperature of operation, and the range over which stable operation is required. An appropriate selection of pyroelectric materials is not only to improve the sensor performance but also to cater to specific sensor applications. For pyroelectric materials, Curie temperature is the critical point where a nonpolar material undergoes a structural transformation; below this critical point, the material exhibits an intrinsic, permanent electrical polarization, usually along a certain crystallographic axis. Table 11.3 presents matrices for the ten pyroelectric crystal classes and two pyroelectric Curie groups. Table 11.4 presents a summary of pyroelectric coefficient of various materials at room temperature (Lingam et al. 2013).

1. Triglycine sulfate (TGS)—$(NH_2CH_2COOH)_3H_2SO_4$: TGS constitutes a large family of isomorphous compounds. The compounds based upon TGS have provided some of the highest pyroelectric figures of merit ($5.5 \times 10^4$ $Cm^{-2}$ $K^{-2}$). TGS possesses a Curie temperature of 49 °C; above this temperature, it exists as centrosymmetric class 2 m, and below this temperature, it is a polar point group 2 with the polar axis along the monoclinic *b* axis. Since the glycine groups are polar

**Table 11.3** Matrices for the 10 pyroelectric crystal classes and two pyroelectric Curie groups (Newnham 2005)

| Point group | Pyroelectric metrics |
|---|---|
| 1 | $(p_1\ p_2\ p_3)^T$ |
| 2 | $(0\ p_2\ 0)^T$ |
| *m* | $(p_1\ 0\ p_3)^T$ |
| *mm*2, 3, 3*m*, 4, 4*mm*, 6, 6*mm*, ∞, ∞*m* | $(0\ 0\ p_3)^T$ |

**Table 11.4** Pyroelectric coefficient of various materials at room temperature, units $\mu C/m^2K$ (Lang 2005; Newnham 2005)

| Material | Experimental value | Secondary coefficient | Primary coefficient |
|---|---|---|---|
| Triglycine sulfate TGS (2) | −270 | −330 | 60 |
| $LiNbO_3$ (3 m) | −83 | +12.8 | −95.8 |
| $LiTaO_3$ (3 m) | −176 | −1 | −175 |
| $Pb_5Ge_3O_{11}$(3) | −95 | +15.5 | −110.5 |
| $BaTiO_3$ (∞ m) | −200 | +60 | −260 |
| $PbZr_{0.95}Ti_{0.05}O_3$ (∞ m) | −268 | +37.7 | −305.7 |
| ZnO (6 mm) | −9.4 | −2.5 | −6.9 |
| CdSe (6 mm) | −3.5 | −0.56 | −2.94 |
| CdS (6 mm) | −4.0 | −1.0 | −3.0 |

in nature, the reversal is largely associated with the rotation of the glycine group about the crystallographic *a*-axis. Despite its high performance, TGS has attracted limited interest for harvesting applications, possibly due to its low Curie temperature. It is also water soluble, hygroscopic, and relatively low strength (Bowen et al. 2014). TGS pyroelectric crystals are primarily used in single element detectors where sensitivity of detection of temperature change is of prime importance (Whatmore 1986; Sahraoui et al. 2003.)

2. Polyvinylidene fluoride (PVDF): PVDF is a ferroelectric polymer, which exhibits a strong piezoelectric effect. PVDF molecules have a repeat unit of $–CH_2–CF_2–$, which take up a number of stable configurations based on the polymers treatment. The polar unit configuration of the material crystal exhibits pyroelectric effect. PVDF has a Curie temperature up to 180 °C, but the polar properties degrade when it is heated above 80 °C. It finds applications in large area detectors for laser pulse monitoring and also single element devices such as intruder alarms. Large PVDF thin films are available commercially at low cost for use in detectors (Whatmore 1986; Wooldridge et al. 2010).
3. Lithium tantalate ($LiTaO_3$): $LiTaO_3$ is an oxygen octahedral crystal consisting of layers of oxygen ions arranged in hexagonal close packing. It is used in single crystal form grown using the Czochralski method and exhibits a moderate pyroelectric effect. $LiTaO_3$ possesses a Curie temperature of 665 °C. $LiTaO_3$ finds applications in pyroelectric detectors, and widespread usage in one-dimensional (1D) commercial detector arrays. $LiTaO_3$ has drawbacks such as high thermal diffusivity, which reduces its minimum resolvable temperature difference at high spatial frequencies. One of the solutions used to resolve this problem is the use of ion beam reticulation to separate detector elements (Whatmore 1986; Geuther and Danon 2005).
4. Non-ferroelectric pyroelectrics include the wurtzite-based materials such as AlN, GaN, CdS, and ZnO which have relatively low pyroelectric coefficients compared to the ferroelectric materials. Since these materials are not ferroelectric, they are often used in single crystal form, such as epitaxially grown films, or as highly orientated structures to achieve the desired polarization. These materials do, however, exhibit higher thermal conductivities compared to the ferroelectric materials allowing a more rapid change in temperature due to changes in ambient temperature (Bowen et al. 2014).

   GaN is a natural pyroelectric with polarization in the *c*-axis. GaN exhibits a strong pyroelectric effect at temperature above 300 °C, whereas $LiTaO_3$ and $PbTiO_3$ exhibit the property below 300 °C, and hence GaN finds applications in high-temperature environments. The pyroelectric coefficient of thin GaN films was reported to be $\sim 10^4$ V/mK (Bykhovski et al. 1996; Yu et al. 2005).

   ZnO is also a wurtzite-structured natural pyroelectric crystal with polarization in the *c*-axis. Most applications utilizing ZnO as the primary material use it in the thin film form. ZnO thin film has exhibited a conversion of thermal radiation ten times larger than GaN films. ZnO possesses a Curie temperature of 430 °C and a pyroelectric coefficient of $4 \times 10^4$ V/mK was observed from experiments

conducted on a bundled arrays of nanowires (Jagadish and Pearton 2011; Yang et al. 2012a, b).

5. Perovskite-based pyroelectrics: Perovskite is a large family of oxygen octahedral crystals with the general formula $ABO_3$. The perovskite structure undergoes deformation to give rhombohedral, tetragonal, or orthorhombic structures. In Lead Zirconate- and Lead Titanate-based structures, dopants are used to improve the pyroelectric properties of these ceramic-based pyroelectrics. Lead Titanate ($PbTiO_3$) possesses a high Curie temperature of 490 °C and a high polarization rate. The preferred method of manufacturing devices is by deposition of thin film layers rather than machining from bulk (Whatmore 1986; Lingam et al. 2013).

   The lead zirconate titanate (PZT) family remains a widely used commercial ceramic due to its relative ease of fabrication in polycrystalline form and good piezoelectric properties, with a range of "hard" and "soft" composition with tailored properties. This family of material has therefore attracted interest for pyroelectric-harvesting applications. For instance, improved pyroelectric properties have been achieved in compositionally graded $PbZr_{1-x}Ti_xO_3$, including high pyroelectric-harvesting FOM. Lanthanum-doped PZT relaxor ferroelectrics have also been used for harvesting applications where doping increases resistivity and coupling coefficients (Bowen et al. 2014).

   Lead magnesium niobate—lead titanate (PMN-PT) single crystals are being explored for transducer applications. The $(1\text{-}x)Pb(Mg_{1/3}Nb_{2/3})O_3\text{–}xPbTiO_3$ ((1-*x*PMN-*x*PT) system is a family of relaxor-based ferroelectric compositions which are of interest for transducer devices due to their ultra-high piezoelectric and pyroelectric coefficients. The morphological phase boundary (MPB) for PMN-*x*PT spans from ($x$ =) 30 to 38 mol% and this range is characterized by a monoclinic phase in coexistence with a rhombohedral (up to 32 mol%) or tetragonal phase (32 to 38 mol%). These crystals have a relatively low Curie temperature (121°), which can limit the material to relatively low temperature operation. Due to their single crystal nature, the materials are relatively expensive and can be formed in limited shapes. The high FOM and range of phase transitions associated with these materials have led to interest in this material for a number of pyroelectric-harvesting applications (Bowen et al. 2014).

6. Additional lead-free materials: Lead-free materials are of interest for environmental and health concerns. Manganese doped bismuth sodium titanate-barium titanate (BNT-BT) single crystal is a potential pyroelectric energy-harvesting material, since the compositions possess excellent piezoelectric and pyroelectric coefficients and high Curie temperatures (TC > 200 °C). BNT-based ceramics can be difficult to pole due to their high electrical conductivities and dielectric loss and to overcome these shortcomings they are often doped. For example, the composition Mn: BNT-BT is a $94.6Bi_{0.5}Na_{0.5}TiO_3\text{-}5.4BaTiO_3$ single crystal doped with Mn and the <111> orientation of this crystal possesses the highest pyroelectric coefficient and figure of merit of lead-free ferroelectric materials. In addition to BNT, $Ba_{0.65}Sr_{0.35}TiO_3$ (BST) thin films have also been examined specifically for improved energy-harvesting FOMs (Bowen et al. 2014).

A family of potassium sodium niobate-based materials, $(K_{0.5}Na_{0.5})NbO_3$ (KNN), have been discovered as a high-performance substitute for lead-based piezoelectric materials. KNN has piezoelectric performance approaching commercially available lead-based materials such as PZT and PMN-PT ceramics. The KNN-LT $[\{(K_{0.5}Na_{0.5})_{0.96}–Li_{0.04}\}(Nb_{0.8}Ta_{0.2})O_3]$ and KNN-LTS $[\{(K_{0.5}Na_{0.5})_{0.96}–Li_{0.04}\}(Nb_{0.84}Ta_{0.1}Sb_{0.06})O_3]$ compositions have improved characteristics compared to pure KNN. Nano-scale $KNbO_3$ has been considered for pyroelectric harvesting (Yang et al. 2012a, b).

In comparison, the best performing materials for FOM are TGS followed by PMN-25PT <111>, Mn:BNT-BT <111>, SBN, $LiTaO_3$, PMN-25PT ceramic, PZT ceramic and Mn:BNT-BT <111>, respectively. From the lead-free materials, co-polymers of PVDF and BNT-based bulk ceramics have better performance compared to the KNN family. The non-ferroelectric pyroelectric materials (e.g., ZnO, GaN, AlN) have lower FOMs compared to the ferroelectrics. However, the FOMs do not include information regarding the operating temperature which, for ferroelectrics, in often related to the Curie temperature. Polymer-based PVDF materials are generally at lower temperatures (<100 °C) compared to the ferroelectric ceramics where the doped PZT family are of interest for higher temperatures. In addition, composite materials are also attracting interest in an effort to combine high-activity ceramic ferroelectrics with a flexible and low-permittivity matrix; these have been examined for pyroelectric detectors but the "composite" approach certainly offer avenues for creating interesting materials for harvesting applications (Bowen et al. 2014).

### 11.4.3 Pyroelectric-Harvesting Devices

Pyroelectric materials have found applications in an array of fields. The most prominent fields are energy harvesting and applications in sensors. For energy harvesting, they convert the thermal energy to electricity, and in sensors, they are used as sensing elements to detect heat (or indirectly motion) signals by conversion into an electric signal. Pyroelectric energy harvesting has been demonstrated in thin films, nanowires, and nanofibers. In particular, thin films offer a large surface area for enhanced thermal exchange and larger electrodes, and hence larger current output (Lingam et al. 2013).

#### 11.4.3.1 Nanostructured and Micro-scale Materials and Devices

For pyroelectric harvesters the operating frequency of the device is often small (typically much less than 1 Hz). In fluid-based systems the frequency of operation is limited by heat transfer between the pyroelectric and the working fluid that is oscillating between hot and cold sources. At the nano-scale, energy transfer by thermal radiation between two semi-infinite solids is almost instantaneous and can be enhanced by several orders of magnitude from the conventional Stefan–Boltzmann law if their separation is a distance smaller than a characteristic

wavelength, given by Wien's displacement law. For example, a device using 60/40 porous poly (vinylidene fluoride-triuoroethylene) was predicted to have a 0.2% efficiency and a 0.84 $mWcm^{-2}$ electrical power output for the cold (273 K) and hot sources (388 K). A pyroelectric plate made from 0.9PMN-PT composite thin films achieved a higher efficiency (1.3%) and a larger power output (6.5 $mWcm^{-2}$) for a temperature oscillation amplitude of 10 K at a temperature of 343 K at a relatively high frequency of 5 Hz (Bowen et al. 2014).

A simple approach to improve the rate of temperature change and increase the pyroelectric current is to reduce the thickness of the pyroelectric, such as using thin films. Figure 11.17 illustrates a flexible hybrid energy cell for simultaneously harvesting thermal, mechanical, and solar energies. A ZnO-poly(3-hexylthioohene) hetero-junction solar cell was used for harvesting solar energy while a PVDF-based pyroelectric and piezoelectric nano-generator was built on its bottom surface for harvesting thermal and mechanical energies, with a pyroelectric coefficient of ~44 $\mu Cm^{-2}\ K^{-1}$. Using a lithium ion battery to store the harvested energy the device could drive

LED devices. Pyroelectric "nano-generators" have also been fabricated based on ZnO nanowire arrays; a higher pyroelectric voltage and current coefficients were obtained for the nano-generator compared to bulk and film material due to the preferred orientation of the ZnO nanowire array. The power of the pyroelectric generator was used to charge a lithium ion battery and a single output pulse could charge a LCD (Fig. 11.17). Lead-free $KNbO_3$ nanowire/PDMS polymer with Ag and indium tin oxide (ITO) electrodes as a flexible nano-generator have also been fabricated where the output could be tuned by the electric field due to changes in ferroelectric domain orientation (Bowen et al. 2014; Yang and Wang 2015).

At the micro-scale, the etching of pyroelectric surfaces and etching the electrode structure can improve energy-harvesting performance. A meshed top electrode and trenched pyroelectric can improve the responsivity of the PZT. A vortex-like electrode with a deep structure produced by sandblasting can improve the harvested power by 11% compared to a fully covered electrode. The size of the pyroelectric element has also been used to tailor the phase transition temperatures in ferroelectric nanowires, enabling a "giant" pyroelectric response. Nanowires have already demonstrated to show enhanced piezoelectric and thermoelectric properties compared to their bulk counterparts. These enhancements are often due to lower defect density in the nanowire form compared to the bulk form, which may also contribute to the pyroelectric enhancement. In addition to nanowires, nanofibers are also attractive for pyroelectric energy harvesting. Nanofibers are often mechanically soft and can be readily incorporated into flexible devises. Nanofibers are mostly fabricated using electrospinning technique. In this technique, a high DC voltage between the liquid in a syringe and a collector spins nanofibers in diameters from several tens of nanometers to several microns (Lingam et al. 2013; Bowen et al. 2014).

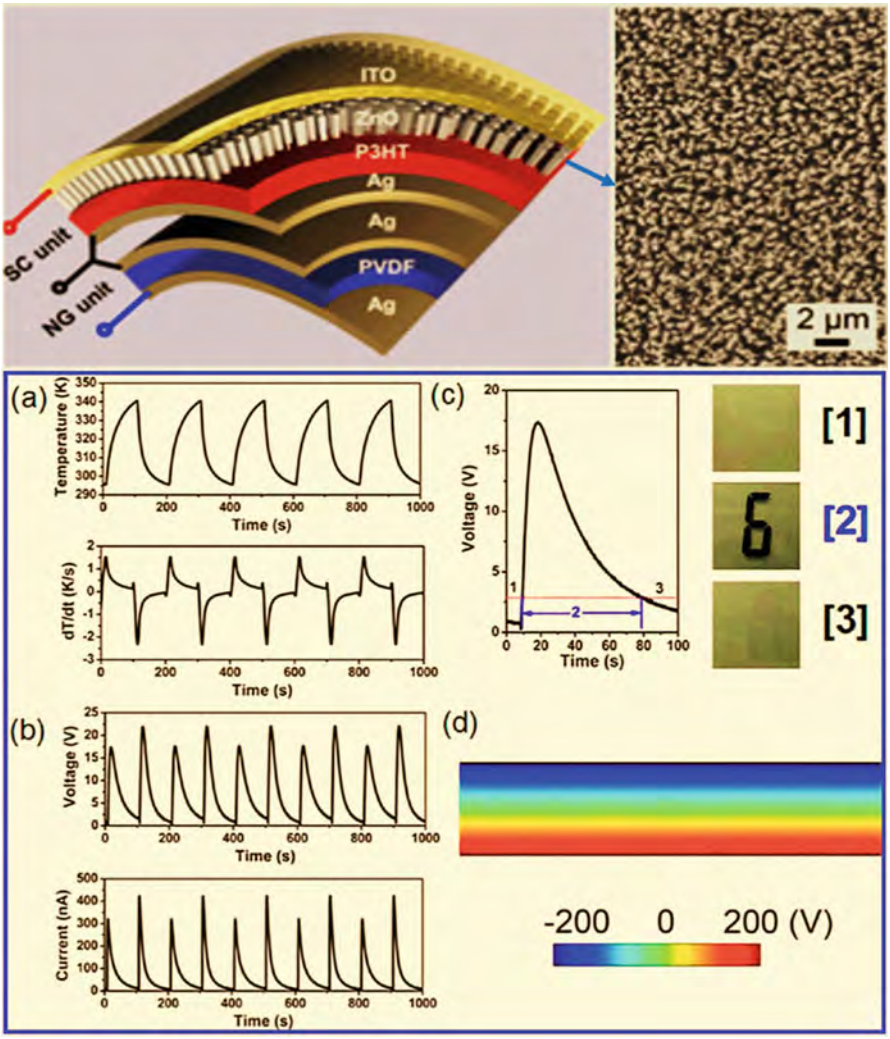


**Fig. 11.17** PZT thin-film pyroelectric generator (Modified with permission from Bowen et al. (2014) (Royal Society of Chemistry); Yang and Wang (2015) (Elsevier)): (**a**) Cyclic change in temperature and differential temperature (dT/dt). (**b**) Output voltage and current of the generator after rectification by a full wave bridge circuit. (**c**) Enlarged single output voltage peak, where it is used to drive a LCD in the region "2." (**d**) Calculated electrical potential distribution across the PZT film

### 11.4.3.2 Hybrid Generators

Since all pyroelectrics are piezoelectric, both pyroelectric and piezoelectric harvesting have been combined. The generation of an electric current under short circuit conditions or an electric potential in open circuit conditions as a result of the change in polarization with a temperature change has analogies with piezoelectric harvesting. Due to their similarities, there is interest for developing potential hybrid

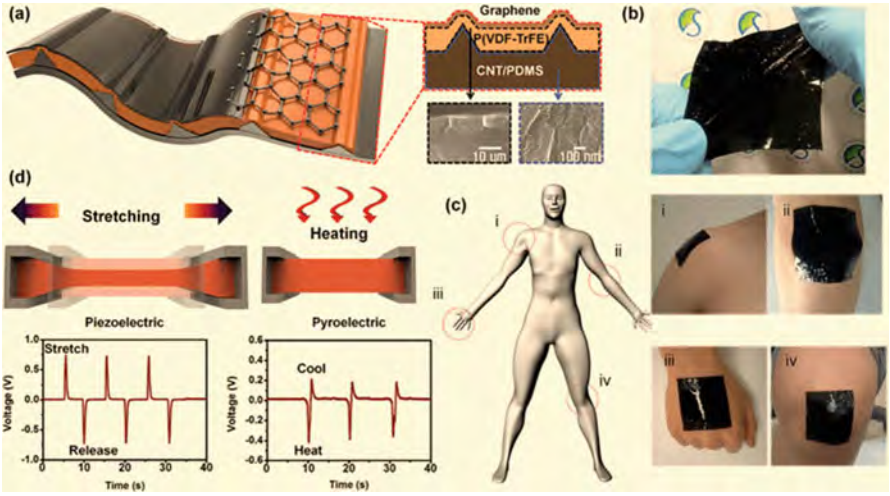


**Fig. 11.18** Hybrid piezoelectric–pyroelectric nano-generator (Modified with permission from Lee et al. (2014) (WILEY-VCH Verlag GmbH & Co)): (**a**) Schematic of stretchable structure of the nano-generator, (**b**) image of device, (**c**) location of devices on body, (**d**) piezoelectric output on application of strain and pyroelectric output on changing temperature

piezoelectric–pyroelectric-harvesting systems, whereby a combination of temperature change and stress is applied (Bowen et al. 2014).

Figure 11.18 shows a stretchable, hybrid piezoelectric–pyroelectric nano-generator based on a micropatterned piezoelectric P(VDF-TrFE) polymer, micropatterned PDMS carbon nanotube (CNTs) composite, and graphene nanosheets. The PDMS-CNT was used to make the device flexible and also serve as a robust electrode on the base of the device. Graphene was used as a top flexible electrode to allow a fast temperature gradient on the device due to its high thermal conductivity. The use of piezoelectric–pyroelectric-harvesters potentially offers an interesting method of enhancing power (Bowen et al. 2014).

### 11.4.3.3 Pyroelectric Systems and Active Oscillators

The pyroelectric generator is modeled as a current source with a capacitor and a resistor in parallel. The current is generated within the pyroelectric element with the change in temperature. However, one of the main problems of pyroelectric energy harvesting is a heating process followed by a cooling process, which produces charge accumulation in different directions. One way to mitigate this problem is to use a full bridge diode rectifier circuit. With it, spatial temperature gradients can be converted into required transient temperature for pyroelectric energy harvesting. Figure 11.19 shows a micro heat engine that acts as a thermal energy shuttle between a heat sink and a heat source. In this configuration, an oscillating thermal field is created across a pyroelectric generator. Using this micro thermomechanic–pyroelectric energy generator (μTMPG), 3 μW power could be harvested for a temperature difference of 79.5 K from pyroelectric generators. With similar methods, hybrid

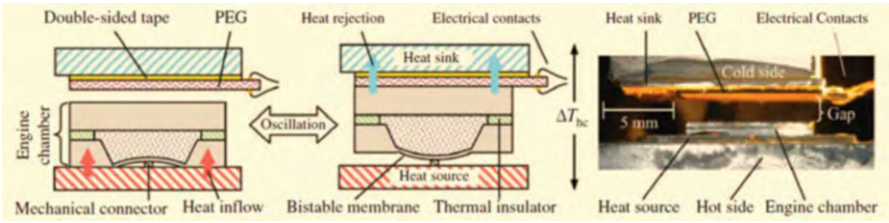


**Fig. 11.19** Illustration of the μTMPG technique for converting stationary spatial temperature gradient into transient temperature gradient (Adapted from Lingam et al. (2013) (Taylor & Francis), used under the Creative Commons Attribution License http://creativecommons.org/licenses/by/3.0/)

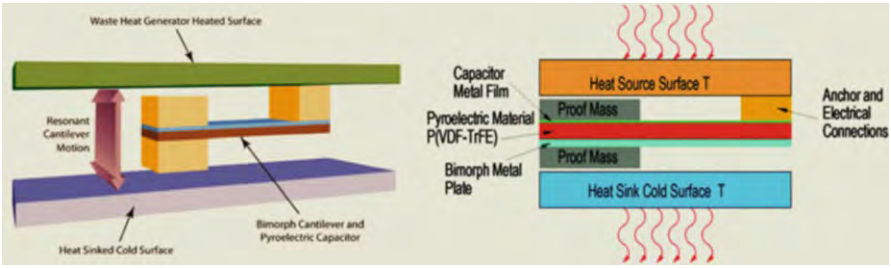


**Fig. 11.20** Pyroelectric bimorph cantilever showing the cantilevered capacitor thin film layers. The energy harvester consisting of a bi-material cantilever which alternately contacts hot and cold surfaces and generates a current in the pyroelectric capacitor (Modified from Hunter et al. (2011) (SPIE), Development of MEMS based pyroelectric thermal energy harvesters, Proc. SPIE 8035, Energy Harvesting and Storage: Materials, Devices, and Applications II, 80350V (17 May 2011); doi: https://doi.org/10.1117/12.882125. Credit: US Oak Ridge National Laboratory)

energy-harvesting devices could be developed that operate for both thermoelectric and pyroelectric energy harvesting (Lingam et al. 2013).

Figure 11.20 shows MEMS-based cantilever harvesting system based on a thermally cycled pyroelectric capacitor that acts as a bimorph cantilever. The bimorph operates between two surfaces, one heated by waste heat and the other is a cold heat sink. Proof masses are placed at the cantilever tip to ensure good thermal contact to the hot and cold surfaces. When the cantilever is heated it deforms due to a thermal expansion mismatch between the bimorph layers that leads to it contacting the cold surface, making the structure cool and deform in the reverse direction and then making contact to the hot surface. This cyclic deformation leads to the cantilever alternately contacting the hot and cold surfaces at the resonant frequency of the cantilever to generate a pyroelectric current. The use of a MEMS approach means that large arrays of devices could be used to increase power and this interesting approach allows the device to potentially operate at high frequencies, up to 20 Hz or higher (Hunter et al. 2011; Bowen et al. 2014).

Another approach to increase operating frequency uses liquid-based switchable thermal interfaces to convert a spatial temperature gradient into temporal temperature oscillations; the system operates in an Olsen type cycle. As shown in Fig. 11.21, a plate with a pyroelectric material oscillates up and down between a high-

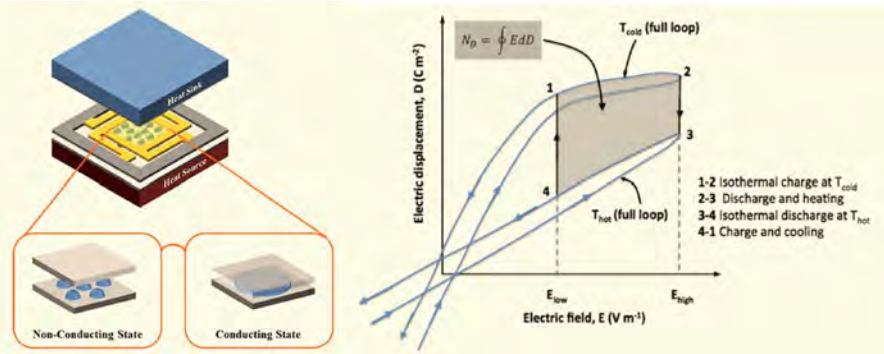


**Fig. 11.21** Pyroelectric energy-harvesting module operating in an Olsen type cycle. Electrode assembly containing a pyroelectric material is actuated up and down and makes alternating thermal contact with the heat source (hot side) and sink (cold side) via switchable thermal interfaces (Modified with permission from Bowen et al. (2014) (Royal Society of Chemistry))

temperature source and a cold heat sink and repeatedly makes thermal contact to undergo temperature oscillations. In the thermally conducting state, the pyroelectric is pressed against the hot or cold surface using a linear actuator and liquid droplets at the interface deform to make them merge into a continuous thin liquid layer of low thermal resistance. In the non-thermally conducting state, the pyroelectric material is physically separated from the hot and cold surfaces and the liquid on the pyroelectric interface exists as discrete droplets. By creating a hydrophilic pattern on the surfaces the rupture distance was reduced, thus reducing the distance required and increasing the operating frequency (Bowen et al. 2014).

## 11.5 Magnetostrictive and Multiferroic Magnetoelectric Materials

Advances in integrated circuits, sensors, and actuators have led to decreased power consumption to a point where energy-harvesting (EH) systems can be used to supply sufficient power to these circuits and wireless devices. The multifunctional properties of multiferroics enable the design of electromagnetic energy-harvesting devices for various sensing, transduction, and memory applications. Muliferroic materials are characterized by two or more ferroic orders, such as ferroelectric, ferromagnetic, or ferroelastic, and the interactions between these order parameters, as shown in Fig. 11.22. In multiferroic magnetoelectric (ME) materials, coupling occurs between the magnetic and electric subsystems. This enables the control of dielectric polarization $P$ by a magnetic field $H$ (direct ME (DME) effect: $\Delta P = \alpha_H \Delta H$) and the manipulation of magnetization $M$ by an electric field $E$ (converse ME (CME) effect: $\mu_0 \Delta M = \alpha_E \Delta E$), with $\mu_0$ denoting the vacuum permeability. The ME response is quantified in terms of the ME coupling coefficient ($\alpha_H$ or $\alpha_E$), which represents the coupling efficiency between the electric and magnetic fields. This is considered as the figure of merit for the strength of ME coupling. Multimode energy-

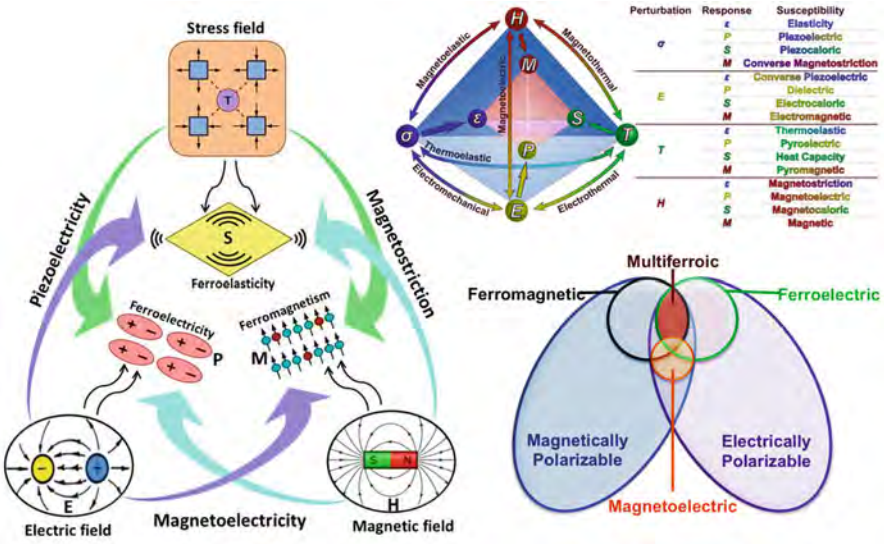


**Fig. 11.22** Schematic illustrating magnetic-elastic-electric couplings in multiferroic materials (Modified with permission from Palneedi et al. (2016) (MDPI) under the Creative Commons Attribution (CC-BY) license. Here, *M* is magnetization, *S* is mechanical strain, and *P* is dielectric polarization

harvesting devices with various configurations have been developed to combine electromagnetic and piezoelectric mechanism. However, under small magnetic fields, the power generated from the electromagnetic energy harvester is limited. An alternative method to harvest magnetic energy is by utilizing magnetoelectric composite. By selecting high-performance piezoelectric and magnetostrictive materials and by optimizing the composite structure, it is expected that a high-efficiency magnetoelectric (ME) transducer with large voltage output under low magnetic field can be obtained. However, to obtain the maximum ME voltage output, an optimized magnitude of DC magnetic bias is needed which presents another challenge in implementation. Alternative approaches have been suggested for magnetoelectric energy harvester that rely on the combination of high-permeabililty magnetostrictive material laminated with piezoelectric plate. However, in these combinations, solenoid and/or permanent magnet is required, which dramatically increases the size and increases the electromagnetic noise. Therefore, different approach such as self-biased ME energy harvester consisting of Ni-MFC laminate and magnetostrictive Ni cantilever has been developed (Zhou et al. 2013, Palneedi et al. 2016).

### 11.5.1 Magnetostrictive Materials

Magnetostrictive materials refer to those exhibiting magnetostrictive effects that are found in ferromagnetic materials. Magnetostrictive effects consist of two mechanisms: the Joules effect and the Villari effect. The former implies that rotation

**Table 11.5** General piezoelectric and magnetostrictive materials used as constituents of ME composites (Palneedi et al. 2016)

| Piezoelectric phase | Magnetostrictive phase |
|---|---|
| *Lead-based:* | *Metals:* |
| $Pb(Zr,Ti)O_3$ (PZT) | Fe, Co, Ni |
| $Pb(Mg_{1/3}Nb_{2/3})O_3$-$PbTiO_3$ (PMN-PT) | *Alloys:* |
| $Pb(Zn_{1/3}Nb_{2/3})O_3$-$PbTiO_3$ (PZN-PT) | FeNi-based |
| $Pb(Mg_{1/3}Nb_{2/3})_y$ $(Zr_xTi_{1-x})_{1-y}O_3$ (PMN–PZT) | FeCo-based |
| $Pb(In_{1/2}Nb_{1/2})O_3$-$Pb(Mg_{1/3}Nb_{2/3})O_3$-$PbTiO_3$ (PIN-PMN-PT) | CoNi-based |
| *Lead-free:* | $Ni_2MnGa$ |
| $BaTiO_3$ (BTO)-based | Permendur (FeCoV) |
| $(K_{0.5}Na_{0.5})NbO_3$ (KNN)-based | Galfenol (FeGa), FeGaB |
| $Na_{0.5}Bi_{0.5}TiO_3$ (NBT)-based | Samfenol ($SmFe_2$) |
| *Others:* | Terfenol-D ($Tbi_{1-x}Dy_xFe_2$) |
| AIN | Fe-based metallic glasses (FeBSi, FeBSiC, FeCoB, FeCoSi, FeCoSiB, FeCuNbSiB) |
| ZnO | |
| $(Sr, Ba)Nb_2O_5$ | *Ceramics:* |
| $Ba_{1-x}Sr_xTiO_3$ (BSTO) | $Fe_3O_4$ |
| $Bi_{1-x}Sr_xTiO_3$ (BST) | $Zn_{0.1}Fe_{2.9}O_4$ (ZFO) |
| $La_3Ga_{5.5}SiO_{14}$ (LGS) | $La_xSr_yMnO_3$ (LSMO) |
| $La_3Ga_{5.5}Ta_{0.5}O_{14}$ (LGT) | $La_xCa_yMnO_3$ (LCMO) |
| Polyurethane (PU) | Ferrites or doped Ferrites (e.g., $NiFe_2O_4$ (NFO), $CoFe_2O_4$ (CFO), Li ferrite, Cu ferrite, Mn ferrite) |
| Polyvinylidene difluoride (PVDF) | |

of moments to align with an applied field generates strains, while the latter implies that applied stresses cause magnetic moments to rotate, thus changing the magnetization for energy harvesting. Table 11.5 shows various piezoelectric and magnetostrictive materials commonly used for synthesizing ME composites. Enhanced piezoelectric and ferroelectric properties can be achieved in ceramics through (a) composition selection (ideally near morphotropic phase boundary (MPB) or polymorphic phase transition (PPT)) and modification (by doping); and (b) microstructure design (via domain engineering and texturing). Among piezoelectric materials, PZT-based ceramics have been widely employed to fabricate the ME composites due to their low cost, high piezoelectric response, and flexibility in modifying the composition to achieve desired properties for targeted applications. For the magnetic component in ME composites, Terfenol-D with high magnetostriction and Metglas (amorphous Fe-alloy) with high magnetic permeability have been the most used materials. Besides magnetic properties, factors such as the processing temperatures, electrical resistance of the material, magnitude of the bias field, phase

connectivity have been considered in choosing the magnetostrictive materials (Palneedi et al. 2016; Narita and Fox 2018).

**INDEPTH: Electromagnetic Energy Harvesters**
The principle used in the electromagnetic transduction is the generation of current in a conductor in a magnetic field. The conductor typically takes form of a coil, and electricity is generated by the relative motion of the conductor and a permanent magnet. The amount of electricity generated depends on the strength of the magnet, the velocity of the movement, and the number of coil windings. The requirement of a large number of windings with low resistance gives a huge limitation for making a MEMS energy harvester with electromagnetic transduction. The planar processes used in silicon microtechnology limit the amount of windings one can achieve, unless a complicated stacking configuration is developed. The wires can be made using thin film deposition techniques. However this will lead to a very high resistance, since it will be difficult and costly to deposit a metal film of more than 1 μm in thickness. Another major problem is that the magnetic field might interfere with the device one wish to power. Electromagnetic energy harvesters are often characterized by high current, low voltage, and low optimal resistive load (Xu 2012).

### 11.5.2 Magnetoelectric Materials

The magnetoelectric effect (ME) denotes any coupling between the magnetic and the electric properties of a material. For example, a dielectric material moving through an electric field would become magnetized. A material where such a coupling is intrinsically present is called a magnetoelectric. Single phase magnetoelectrics are chemically homogenous and isotropic compounds. They exhibit intrinsic ME coupling but require the coexistence of magnetic moments and electric dipoles with long-range ordering. From a fundamental point of view, the coupling between the magnetic and polar sublattices in single phase ME compounds is fascinating. However, due to the mutual exclusion of ferromagnetism and ferroelectricity, only few monolithic ME materials such as $Cr_2O_3$ and $BiFeO_3$ exhibiting non-zero coupling at room temperature have been found so far. Most of the single phase materials possess either low permittivity or low permeability at room temperature and thus exhibit weak ME coupling which hinders their applications. For example, $BiFeO_3$, the archetype of single phase ME compounds, displays good ferroelectricity but weak ferromagnetic properties above room temperature (Palneedi et al. 2016; Narita and Fox 2018).

ME composites consist of physically separated magnetic and electric order phases. These composites show coupling with orders of magnitude larger than those found in single phase materials at room temperature. ME coupling in

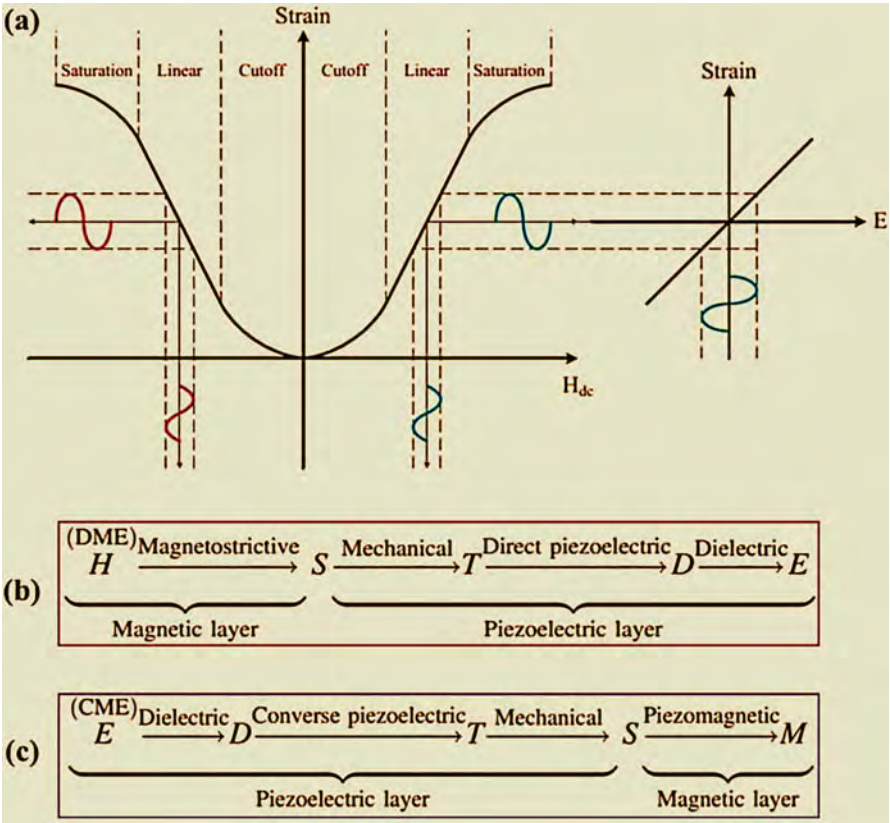


**Fig. 11.23** Schematic representation of the (**a**) ME effect utilizing the product property; (**b**) DME effect and (**c**) CME effect in composites. Here, $H$ is magnetic field, $S$ is mechanical strain, $T$ is mechanical stress, $D$ is electric displacement, $E$ is electric field, and $M$ is magnetization (Modified with permission from Palneedi et al. (2016) (MDPI) under the Creative Commons Attribution (CC-BY) license)

composites occurs extrinsically in three different ways mediated through (i) strain, (ii) charge carrier, and (iii) spin exchange. Among these mechanisms, the strain-mediated ME coupling has been widely studied, while the investigations on the other two mechanisms are still in early stages. The strain-mediated ME effect in composites is a product tensor property and results from the elastic coupling between the piezoelectric and magnetostrictive components, as illustrated in Fig. 11.23. In DME coupling, the applied magnetic field generates strain in the magnetic layer via the magnetostriction effect, and this strain is transferred to the piezoelectric layer resulting in an electric displacement or a dielectric polarization through the piezoelectric effect. In CME coupling, an external electric field induces strain in the ferroelectric layer due to the inverse piezoelectric effect, and the strain transferred to the magnetic layer produces a magnetization change or domain reorientation by the piezomagnetic effect (Palneedi et al. 2016).

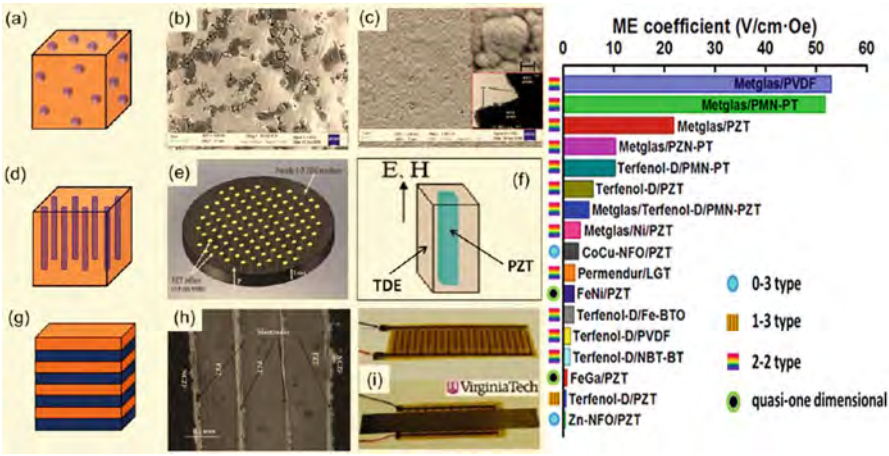


**Fig. 11.24** Bulk ME composites with different phase connectivity (Modified with permission from Palneedi et al. (2016) (MDPI) under the Creative Commons Attribution (CC-BY) license): (**a**–**c**) 0–3 connectivity; (**d**–**f**) 1–3 connectivity; and (**g**–**i**) 2–2 connectivity

ME composites have been commonly prepared with 0-3, 1-3, and 2-2 connectivity, as shown in Fig. 11.24a, d, and g, respectively. Here, the numbers represent the connectivity of the magnetic and piezoelectric phases, respectively. In the 0-3 particle-matrix composites, magnetic particles are embedded in the piezoelectric matrix. 1-3 cylinder-matrix composites are formed by embedding magnetic fibers/rods/tubes/wires in the piezoelectric matrix. The particles (in the 0-3 composite) and fibers (in the 1-3 composite) can be either randomly dispersed or periodically aligned. A 2-2 laminate composite consists of alternating magnetic and piezoelectric layers. Such laminates can be prepared in different shapes and geometries, including disks, squares, rectangles, and rings, with different dimensions. They can be arranged as unimorphs and bimorphs as well as bilayered and multilayered structures. Further, for all of these composites, the volume fraction and dimensions of the constituents can be altered to tailor the properties of the composite. The 2-2 composites preserve the physical characteristics of individual phases, and they are comparatively simpler to fabricate. These composites can be poled to a higher degree since the piezoelectric and the low-resistivity magnetic phases are separated. The 2-2 layered composites exhibit higher ME responses compared to the 0-3 and 1-3 composites. There have been other composite structures, such as 3-2 structured composite consisting of a $(Ni_{0.6}Cu_{0.2}Zn_{0.2})Fe_2O_4$ [NCZF] phase with 2D connectivity dispersed in a 0.8Pb $(Zr_{0.52}Ti_{0.48})O_3$–0.2Pb$(Zn_{1/3}Nb_{2/3})O_3$ [PZNT] matrix; quasi-one-dimensional ME composite by inserting a magnetostrictive wire (FeNi/FeGa/FeCoV) into a PZT tube where the tube-wire interface bonding was made with silver paste. In comparison, 2-2 composite structure has inherent advantages in terms of fabrication and performance (Gillette et al. 2014; Palneedi et al. 2016).

As device design trends towards miniaturization and multifunctionality, thin film conformations are highly desired for application in integrated magnetic/electric

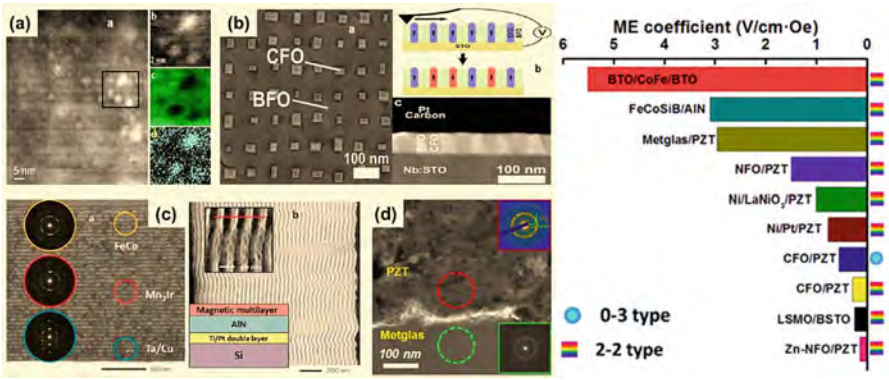


**Fig. 11.25** Film-based ME composites with (**a**) 0–3 connectivity, (**b**) 1–3 connectivity, (**c**, **d**) 2–2 connectivity (Modified with permission from Palneedi et al. (2016) (MDPI))

devices. In film-based ME composites, optimized interface coupling can be achieved through the direct bonding of components. Moreover, large electric fields can be comfortably applied to thin films since they require relatively smaller bias voltages than those needed for bulk samples. This extends the scope of thin films for devices which have limitations on their operating voltages. The greater freedom and flexibility in the fabrication of film-based ME composites render their property tuning, through interfacial coupling and strain engineering, control of crystal structure and orientation, grain size, and layer thickness, as well as chemical modification with a wide range of substituents, etc. Composite films can also facilitate the understanding of the physical phenomena involved in ME effects at lower dimensions, and thus enable the design of new types of magnetoelectrics with novel phase structures. Figure 11.25 shows some examples of ME composite films using various film deposition methods. Some of these methods can yield excellent thin film epitaxial growth with atomic scale thickness control and coherent interfaces. However, most ME composite films show very low ME properties due to reduced electromechanical parameters as a consequence of substrate clamping (Yan and Priya 2015; Palneedi et al. 2016).

More ME composites have been developed, such as broadband ME with piezoelectric anisotropy, ME composites with textured piezoelectric ceramics, self-biased ME composites, and ME nanocomposites with core/shell arrangement in the form of nanoparticles, nanowire arrays, and nanotubes. Other 1D composite structures with random and Janus-type arrangements have also been prepared with different wet chemical synthesis methods, as shown in Fig. 11.26. For example, $CoFe_2O_4/BaTiO_3$ core/shell nanoparticles (Fig. 11.26a) was fabricated using a combination of solution processing and high-temperature calcination. Ferrite/perovskite oxide core/shell nanostructures can be formed in multiferroic systems such as $Fe_3O_4/PbTiO_3$, $\gamma$-$Fe_2O_3/PbTiO_3$, $\gamma$-$Fe_2O_3/Pb(Zr,Ti)O_3$, $CoFe_2O_4/BaTiO_3$, $CoFe_2O_4/PbTiO_3$, and $CoFe_2O_4/Pb(Zr,Ti)O_3$ using a combined hydrothermal and annealing process. Ordered arrays of $NiFe_2O_4$/PZT core/shell nanowires (Fig. 11.26b) was synthesized with a method involving the combination of a modified sol-gel process,

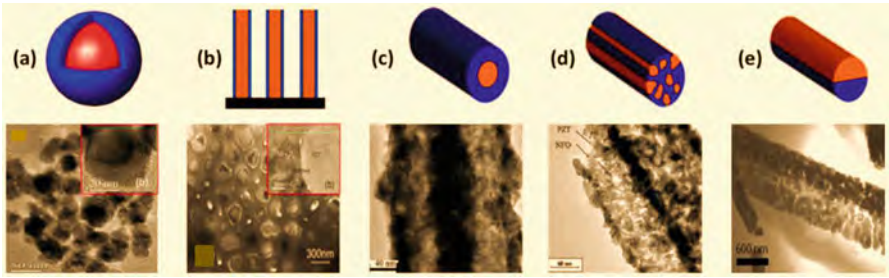


**Fig. 11.26** Biphasic ME composites with different types of arrangements between the two phases (**a**–**c**) core/shell arrangement (Adapted from Palneedi et al. (2016) (MDPI) under the Creative Commons Attribution (CC-BY) license): (**a**) nanoparticles; (**b**) nanowires; and (**c**) nanotubes; (**d**) random arrangement; and (**e**) Janus-type arrangement

**Table 11.6** Classification of different ME devices (Palneedi et al. 2016)

| ME coupling | Physical mechanism | ME devices |
|---|---|---|
| Direct ME coupling | H control of electric polarization | Magnetic sensors, current sensors, transformers, gyrators, energy harvesters |
| Converse ME coupling | E control of magnetization switching | Spintronics, including random access memories, tunnel junctions |
| | E control of permeability μ | Voltage tunable inductors, tunable band-pass filters, phase shifters |
| | E control of spin wave | Voltage tunable filters, tunable resonators, phase shifters |

electrochemical deposition, and subsequent oxidization in anodized nanoporous alumina membranes. In addition, multiferroic nanofibers with core/shell, random, and Janus-type arrangements (Fig. 11.26c–e) have been fabricated by electrospinning. Nevertheless, some of the challenges in the practical implementation of these ME nanocomposites include forming isolated multiferroic particles that are free of agglomerates, substrate-free assembling of nanofibers into ordered structures, and difficulties in accessing their ME properties. Further, in some cases, these nanostructured ME composites will have to be consolidated into a dense form for device applications which may affect the stability of nanostructures (Andrew et al. 2014, Palneedi et al. 2016).

### 11.5.3 Magnetoelectric Devices and Applications

Based on the type of ME coupling and the mechanisms used to control the order parameters, a variety of applications have been proposed, including magnetic sensors, high-frequency inductors, memory devices, and high-frequency signal processing devices, as shown in Table 11.6 (Palneedi et al. 2016).

ME material-based sensor devices are considered to be promising alternatives for conventional Hall sensors and giant magnetoresistive (GMR) devices. Because of their passive nature and self-powered operation at room temperature, ME sensors

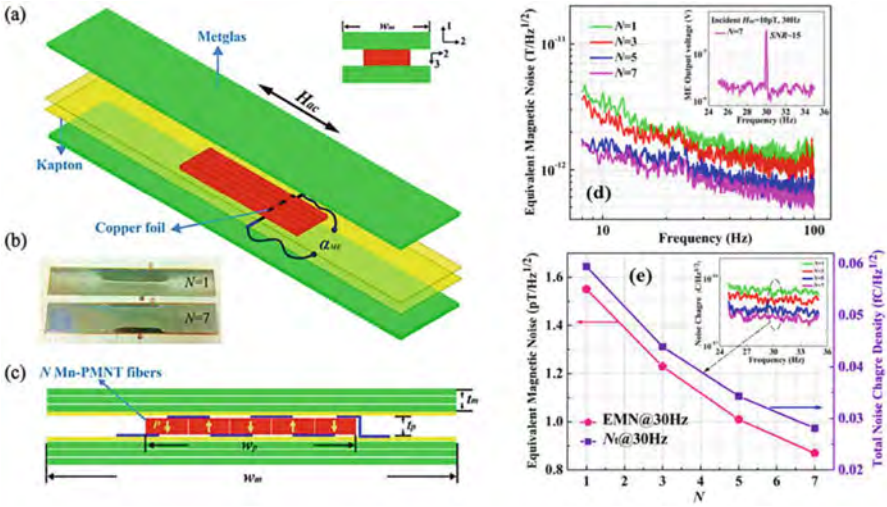


**Fig. 11.27** Metglas/Mn-PMNT composite sensor (Modified with permission from Fang et al. (2015) (IOP Publishing)): (**a**–**c**) 3D structure, photograph, cross-sectional schematic diagram, respectively; (**d**, **e**) equivalent magnetic noise level and total noise charge density of the ME magnetic sensors

may be able to replace bulky and expensive superconducting quantum interference devices (SQUIDs). ME sensors have the potential to perform biomagnetic measurements analogous to all of those performed by magnetic fields (MEG) and haemodynamics (fMRI). The key requirements for magnetic field sensors in this application are (i) sensitivity of ~pT to fT per $\sqrt{H_z}$ at low frequencies ($10^{-2}$ to $10^3$ Hz); and (ii) ambient temperature and wide bandwidth (0.1 to 100 Hz) operation. The direct ME coupling effect, where the ME voltage coefficient is dependent on AC and DC magnetic fields, would allow the ME composites to sense either an AC or DC magnetic field by monitoring the output electrical signals. Since a current passing through a wire generates a magnetic field in the surrounding space, the ME composite can also be used as a current probe for detecting current by monitoring the corresponding magnetic flux. Various ME laminate-based sensors with multi-push-pull configurations, multilayer configuration, and bimorphs, all of which exhibit an improved ME voltage coefficient, have demonstrated considerable potential for sensing low-frequency magnetic field variations. Figure 11.27 shows Metglas/Mn-PMNT laminate composite consisting of longitudinal magnetized Metglas layers and different numbers ($N$) of transversely polarized Mn-PMNT fibers connected in series. An ultralow magnetic field sensitivity of 0.87 pT/$\sqrt{H_z}$ at room temperature was reported for these Metglas/Mn-PMNT fiber laminate composites. In comparison, thin film-based ME sensors enable the fabrication of miniaturized low-cost sensor devices with high sensitivity and high spectral resolution. Thin film-based architecture also provides the capability for designing sensor arrays that can be integrated with other circuit components (Stephan et al. 2012; Fang et al. 2015).

Harvesting energy from ambient energy sources such as vibrations, sound, radio-frequency waves, light, temperature gradients, wind, and others is an area of focus for current and next-generation remote monitoring electronic devices and self-powered wireless sensor networks with the goal of improving device lifetime and addressing the limitations of conventional batteries. In addition, the ambient environment is filled with magnetic noise of 50–60 Hz almost everywhere these days. Harvesting this weak and low-frequency magnetic noise (<1 mT = 10 G) to develop a consistent electricity source remains a difficult challenge. Magneto-mechano-electric (MME) mechanism has been attempted to obtain optimum electricity from the tiny magnetic fields in the surroundings. The operation mechanism can be described as follows: When the ME composite is placed in an AC magnetic field, the magnetostrictive layer in the composite responds to the mechanical vibration (magneto-mechano coupling), thereby straining the piezoelectric layer, which results in an output voltage across the electrical load through the direct piezoelectric effect (mechano-electric coupling). Due to the existence of the piezoelectric phase in the ME composite, any mechanical oscillation applied to the composite directly creates electrical voltage. Consequently, the MME generator could be used to harvest energy from both the magnetic field and external vibrations at the same time. This sequential operating process is schematically depicted in Fig. 11.28a. By selecting high-performance piezoelectric and magnetostrictive materials and by optimizing the composite structure, it is expected that high electric power density can be obtained from a low-frequency magnetic field using the MME generator.

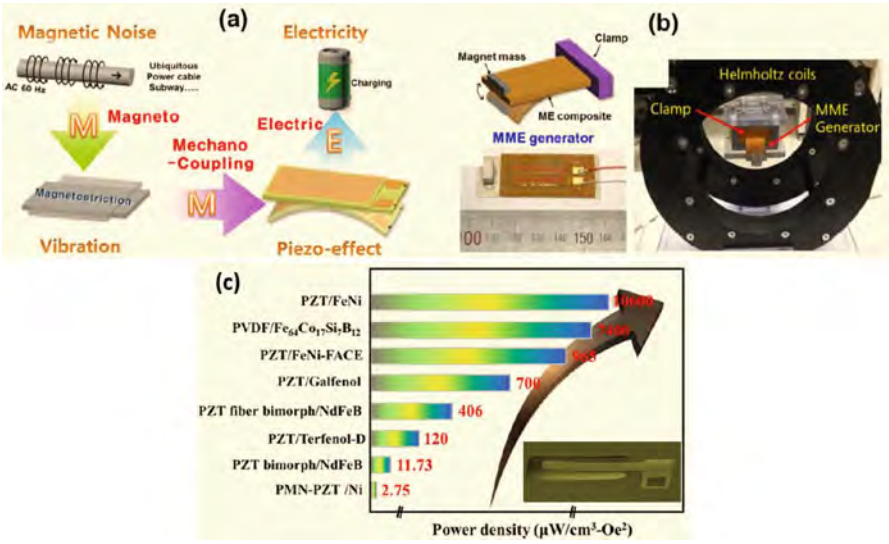


**Fig. 11.28** Magneto-Mechano-Electric (MME) energy harvesters (Modified with permission from Ryu et al. (2015) (Royal Society of Chemistry), and Palneedi et al. (2016) (MDPI)): (**a**) Schematic depicting the working principle; (**b**) schematic and photo of cantilever structured MME energy harvester; (**c**) power densities from the MME harvesters made with different composite systems

Figure 11.28b shows a ME generator constructed using an anisotropic and flexible piezoelectric $Pb(Mg_{1/3}Nb_{2/3})O_3$–$PbTiO_3$ (PMN–PT) single crystal fiber composite (SFC), a cost-effective magnetostrictive Ni plate and Nd permanent magnetic proof mass. The flexibility of the SFC ensures the high compliance of the sample, which is ideal for achieving low resonance frequency in a cantilever structure. The flexibility also increases device durability and enables the application of increased strain magnitudes. The Ni plate can be easily self-biased and generates a linear strain response in a low-level magnetic field environment. The performance of the MME generator containing an anisotropic <011> SFC with $d_{32}$ mode under a small noise level magnetic field is shown in Fig. 11.28b. At 60 Hz, and Hac $\sim$ 500 μT, the maximum generated voltage was $\sim$34 Vpp ($\sim$12.4Vrms). The power from the MME generator was high enough to fully charge a 220-μF electrolytic capacitor after rectifying for 3 min. Using the stored power in the charged capacitor, the device was able to turn on 35 commercial high-intensity LEDs with a turn on/off frequency of $\sim$1 Hz. Similarly, efforts have also been made to develop energy harvesters based on ME composite films. Seeking to improve the output power density, various MME harvesters have been developed using different combinations of magnetostrictive and piezoelectric materials, which represent significant advances towards next-generation remote monitoring electronic devices and self-powered wireless sensor networks (Ryu et al. 2015; Palneedi et al. 2016).

Motivated by the advances in multiferroics, ME composites have been suggested for biomedical applications such as wireless endoscopy, minimally invasive surgical tools, and stimulation of functions of living cells. The potential use of ME nanoparticles (MENs) as carriers for on-demand drug release and to artificially stimulate the neural activity deep in the brain has also been suggested. Wireless capsule endoscopes (WCEs) are often used to examine the gastrointestinal (GI) tract for clinical diagnosis (Fig. 11.29a). Though the WCEs are far less invasive compared to conventional endoscopes, the passive nature of WCEs makes it difficult to control their position and orientation as the capsule moves along the GI tract (Paluszek et al. 2015).

Controlling the function of biological macromolecules is of vital importance in health science studies. Approaches used to stimulate cell functions include the use of the heat generated by hysteresis losses in magnetic nanoparticles placed in a high-frequency magnetic field, and the mechanical agitation of magnetic nanoparticles attached to cells using external low-frequency magnetic fields. The interaction between electromagnetic fields and biological macromolecules can be understood by studying the ion channels which regulate several cellular processes, such as action potentials in neurons or muscle contraction. Figure 11.29b shows an innovative approach, based on the use of core/shell-structured MENs with a ferromagnetic core and a ferroelectric shell, that would allow the remote control of ion channel gating via externally applied magnetic fields. In this approach, electric fields in the vicinity of the cells generated by MENs introduced extra- or intracellularly can be locally modified to invoke appropriate conformational changes in the ion channels. The resulting local depolarization or hyperpolarization of the membrane will lead to opening or closing of the ion channels accordingly. Because of the remote way in

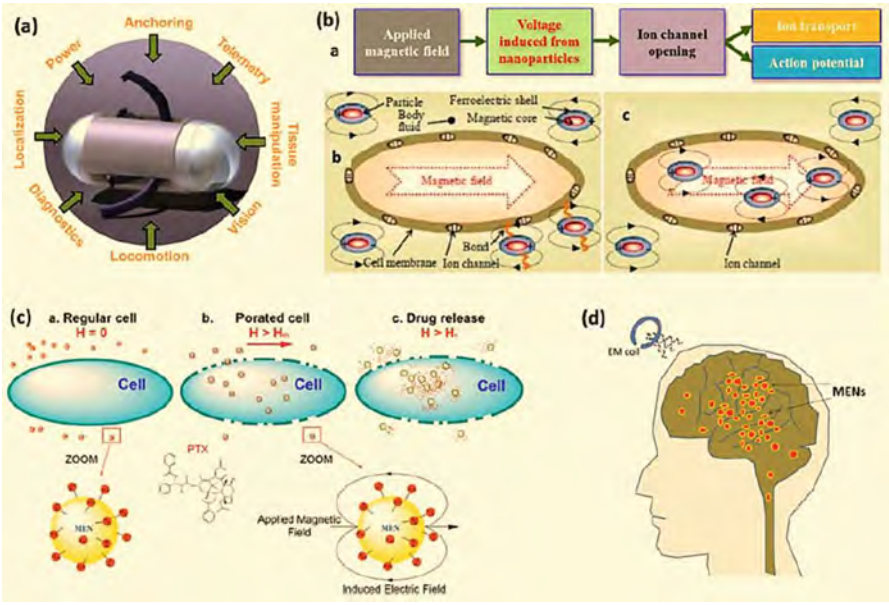


**Fig. 11.29** ME composites for biomedical applications (Adapted with permission from Palneedi et al. (2016) (MDPI)): (**a**) Key functionalities that complement the wireless capsule endoscopes; (**b**) illustration of possible mechanisms of stimulation of ion channels: a chain of actions triggered by the applied magnetic field pulses, external and internal stimulation by uptaken nanoparticles; (**c**) MENs as field-controlled nano-electroporation sites to let the drug through the cancer cell membranes; (**d**) illustration of the deep brain stimulation

which the stimulation will be performed, individual cells or selected groups of cells can be targeted, rather than whole tissues (Kargol et al. 2012).

Targeted drug delivery with adequate high specificity (to tumor cells) remains a formidable task in the treatment of cancer in general, particularly ovarian cancer. Although the survival rates have been improved by intraperitoneal (IP) delivery through a surgically implanted catheter, toxicity and catheter complications have precluded widespread adoption of this invasive means of delivery. By exploiting the dependence of the membrane's porosity on the electric field, electroporation can be utilized to trigger drug delivery into the cells, as shown in Fig. 11.29c. Above a threshold magnetic field ($H_{th}$), the MENs loaded with the drug and optionally with the biomarker-specific antibodies (for delivery to the tumor cells) can generate localized fields large enough to open up the membrane pores in their proximity and thus allow the delivery of the drug inside the tumor cells. The drug can be released off the MENs by further increasing the field above the second critical value, Hr, necessary for overcoming the drug-MEN binding energy. This hypothesis was testified through in vitro studies on human ovarian carcinoma cell (SKOV-3) and healthy cell (HOMEC) lines, where a 30-Oe DC bias was applied to trigger high specificity uptake of Paclitaxel (PTX) loaded on 30-nm $CoFe_2O_4/BaTiO_3$ core/shell

MENs. The drug penetrated through the membrane and completely eradicated the tumor within 24 h without affecting the normal cells (Guduru et al. 2013).

In the human neural network, chemical and electrical synapses transfer information between adjacent axons and dendrites directly or indirectly through electric field energy. The ability to efficiently control the network at micro- or even nano-scale can enable significant control over important brain functions. Existing noninvasive brain stimulation methods including repetitive transcranial magnetic stimulation (rTMS) and transcranial direct current stimulation (tDCS) are limited in their depth and locality. A potential solution would be to use MENs for noninvasive control of the neural network. In this approach, very low-intensity external magnetic field is required to stimulate brain activity at any depth in the brain and the field can be focused to act upon MENs in any particular region of the brain. The external magnetic field generates AC signals in ME nanoparticles that are correlated with the frequency spectrum of the neural activity, which in turn causes neurons in that region to fire at similar frequencies, as shown in Fig. 11.29d (Yue et al. 2012).

## 11.6 Triboelectric Materials

The triboelectric effect, also known as triboelectric charging, is a type of contact electrification in which certain materials become electrically charged after they come into frictional contact with a different material. The polarity and strength of the charges produced differ according to the materials, surface roughness, temperature, strain, and other properties. Triboelectric nanogenerators (TENGs), based on the triboelectric effect, provide an alternative approach to generating electricity from mechanical energy to operate small electronic devices. In the triboelectric effect, a material surface becomes electrically charged after it comes into contact with a different material through friction, owing to charge transfer between the two materials. These transferred charges remain for a long time on their respective surfaces. An electrostatically charged material causes a potential, and it drives induced electrons to flow between the electrodes by periodic contact and separation of the two materials. The generated electric potential V can be calculated with the following equation (Lee et al. 2016):

$$V = -\frac{\rho d}{\varepsilon_0} \tag{11.14}$$

where ρ is the triboelectric charge density, $\varepsilon_0$ is the vacuum permittivity, and $d$ is the interlayer distance in a given state. The current $I$ generated across an external load can be defined as (Lee et al. 2016):

$$I = C\frac{\partial V}{\partial t} + V\frac{\partial C}{\partial t} \tag{11.15}$$

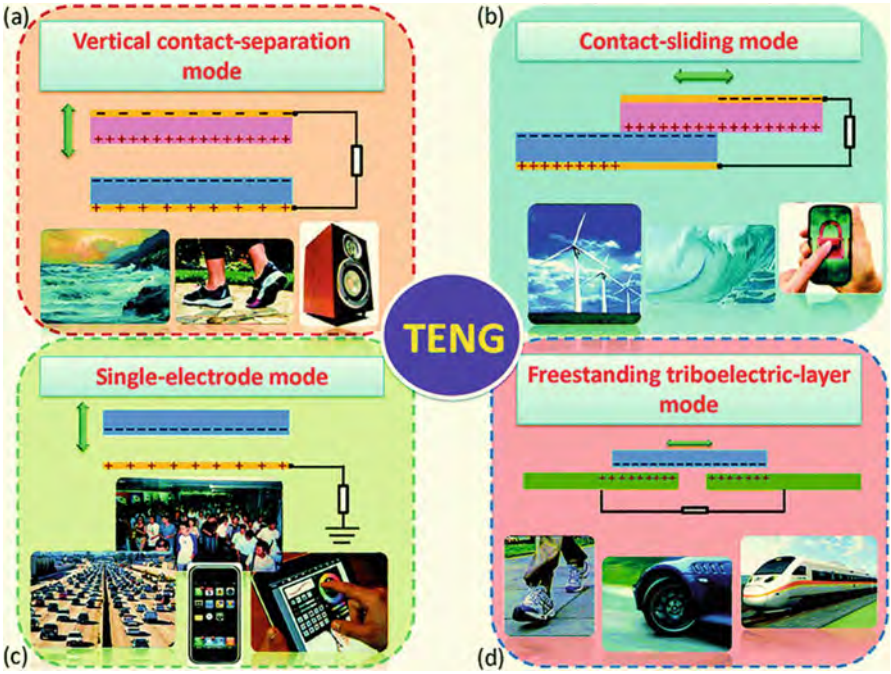


**Fig. 11.30** The four fundamental working modes of the triboelectric nanogenerators (Adapted with permission from Wang et al. (2015b) (Royal Society of Chemistry)): (**a**) The vertical contact–separation mode; (**b**) the lateral sliding mode; (**c**) the single-electrode mode; (**d**) the free-standing mode

where $C$ denotes the capacitance of the system and $V$ is the voltage across the two electrodes. The first term is the change in potential between the top and bottom electrodes due to the triboelectric charges. The second term is the variation in the capacitance of the system when the distance between two electrodes is changed due to the mechanical deformation. Numerous advantages of TENGs include superior power output performance, many material options, easy tailoring of device structures, cost-effectiveness, the facile fabrication of large areas for applications, and stability and robustness, as well as environmental friendliness. Depending on the configuration of the electrodes and the different ways in which the triboelectric layers can be arranged, as shown in Fig. 11.30, four operation modes of TENGs have been developed (Wang et al. 2015a, b): the vertical contact mode, the lateral sliding mode, the single electrode mode, and the free-standing mode. Their applications as various self-powered nanosystems, such as acceleration sensors, motion vector sensors, biomedical monitoring systems, electrochromic devices, sound recording systems, pressure sensors, angle measurement sensors, active tactile sensor systems, tactile imaging devices, electroluminescent systems, and mercury-ion detection systems, have been demonstrated. The triboelectric output can be further enhanced through control of electron affinity, as well as the work function, chemical structure, pressure, and surface roughness of the materials (Lee et al. 2016).

### 11.6.1 Triboelectric Nanogenerators as a Sustainable Power Source

The triboelectric nanogenerator offers a completely innovative approach for energy harvesting from the vast environment due to its high power density, light weight, small size, and so on. However, several output performances of the TENG should be improved such as output power, current, and energy conversion efficiency. Hence, many principles and mechanisms have been demonstrated to realize the enhancement of TENGs as a sustainable power source for electronics (Lin et al. 2016).

Enabled by an advanced structural design of two radial-arrayed fine electrodes that are complementary on the same plane, the planar-structured TENG generates periodically changing triboelectric potential that induces alternating currents between electrodes. The TENG has a multilayered structure, which consists of mainly two parts, i.e., a rotator and a stator, as sketched in Fig. 11.31a. A photograph of an as-fabricated device is demonstrated in Fig. 11.31b. For quantitative characterization, a programmable rotary motor was connected to the rotator that was in co-axial alignment with the stator. At a rotating rate of 500 r $min^{-1}$, the short circuit current ($I_{SC}$) has a continuous AC output with an average amplitude of 0.5 mA and a frequency of 500 Hz (Fig. 11.31c). For open-circuit voltage (VOC), it oscillates at the same frequency with a peak-to-peak value of 870 V (Fig. 11.31d). Furthermore, the matched load also has a variable value, exhibiting a reversely proportional relationship with the rotation rate, as shown in Fig. 11.31e. Consequently, linearly rising output power can be obtained at higher rotation rates (Zhu et al. 2014).

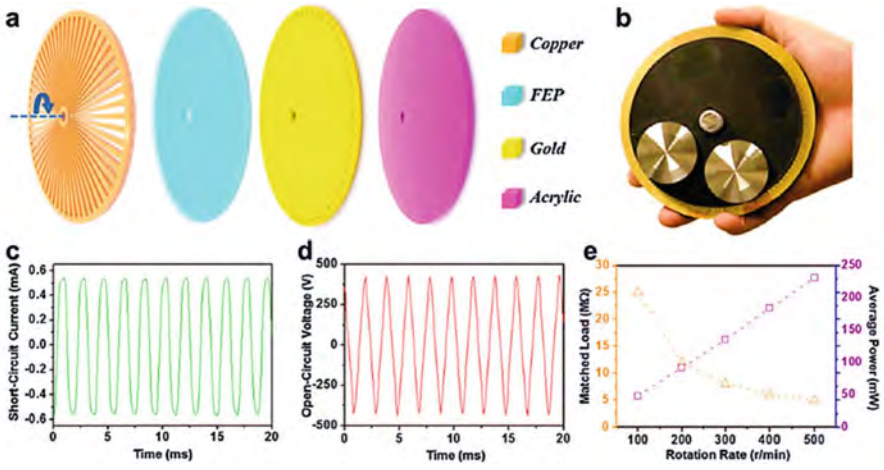


**Fig. 11.31** Radial arrayed triboelectric generator for high-performance mechanical energy harvesting (Modified with permission from Zhu et al. (2014) (Springer Nature): (**a**) Schematic illustrations of the triboelectric generator, which has two parts, that is, a rotator and a stator; (**b**) a photograph of an as-fabricated triboelectric generator. The short-circuit current; (**c**) and open-circuit voltage (**d**) of the triboelectric generator under a rotation rate of 500 r/min; (**e**) matched load resistance and average output power with increasing rotation rate

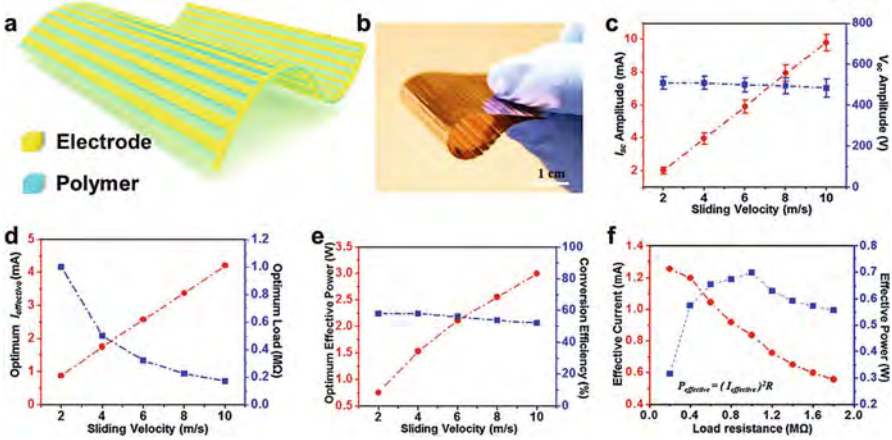


**Fig. 11.32** A thin-film-based micro-grating triboelectric nanogenerator (MG-TENG) for high-performance mechanical energy harvesting (Adapted with permission from Wang et al. (2015b) (Royal Society of Chemistry)): schematic illustration (**a**) and a photograph (**b**) of the MG-TENG. (**c**) The sliding velocity dependent current and voltage output of the MG-TENG. (**d**) The optimum effective current and corresponding load with varying sliding velocity. (**e**) The optimum effective power of the MG-TENG with varying sliding velocity. (**f**) Load matching test at a sliding velocity of 2 m/s. Maximum effective power is obtained at the matched load of 1 MΩ

Furthermore, a thin-film-based micro-grating triboelectric nanogenerator (MG-TENG) is also developed for high-efficiency power generation through conversion of mechanical energy. The shape-adaptive MG-TENG relies on sliding electrification between complementary micro-sized arrays of linear grating, which offers a unique and straightforward solution in harnessing energy from relative sliding motion between surfaces. Figure 11.32a is a schematic illustration of the MG-TENG, while Fig. 11.32b is a photograph of the as-fabricated device, which is extremely thin and flexible. And the sliding velocity-dependent electric output of the MG-TENG is characterized. As shown in Fig. 11.32c, a nearly linear relationship between the amplitude of short-circuit current ($I_{SC}$) and the sliding velocity can be obtained. While the open-circuit voltage ($V_{OC}$) is independent of the sliding velocity. In the meantime, as shown in Fig. 11.32d, the corresponding matched load is approximately reversely proportional to the sliding velocity. Thus, the optimum effective current is also linearly related to the sliding velocity, as demonstrated in Fig. 11.32e. To evaluate the capability of the MG-TENG for power generation, resistors were utilized as external loads for characterization. As displayed in Fig. 11.32f, the current amplitude drops with increasing load resistance owing to the ohmic loss, and the effective power is maximized to a value of 0.76 W at a load resistance of 1 MΩ and a sliding velocity of 2 m/s. And operating at a sliding velocity of 10 m/s, an MG-TENG of 60 $cm^2$ in overall area can deliver an average output power of 3 W and a power density of 50mW$cm^2$ at an overall conversion efficiency of 50%. Holding a collection of compelling features, including high electric output power, extremely light-weight, low cost, scalability, and adaptability,

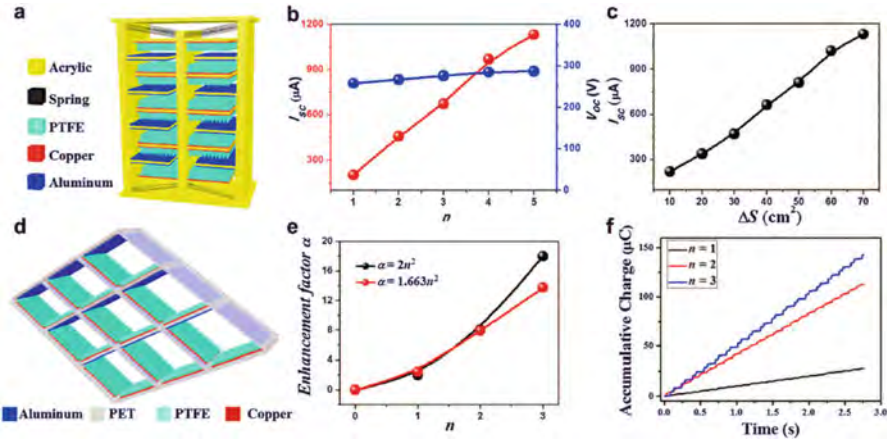


**Fig. 11.33** Enhancement of the output current of the TENG based on multilayer integrations (Adapted with permission from Wang et al. (2015b) (Royal Society of Chemistry)): (**a**) schematic illustration of the multilayered stacked TENG. (**b**) Dependence of electric output on the number of pinned fingers *n*. (**c**) Dependence of the short-circuit current on the effective contact area (DS) of the TENG with $n = 5$. (**d**) Sketch of an integrated rhombic gridding-based triboelectric nanogenerator. (**e**) The current's enhancement factor a is increasing as a function of number of unit cells along the edge length *n*. (**f**) Accumulative inductive charges generated by the TENG with $n = 1$, 2, and 3, respectively

the MG-TENG is another practically effective approach in harvesting ambient mechanical motions as well as possibly producing electricity at a large scale (Wang et al. 2015a, b).

The application of TENG for mechanical energy harvesting may be challenged by its low output current, and a possible solution is to synchronize the outputs of all multiple units so that the instantaneous output power can be maximized. In this regard, a multilayered stacked TENG was developed as a cost-effective, simple, and robust approach for harvesting ambient mechanical energy. The 3D-TENG has a multilayered structure with acrylic as supporting substrates, as schematically shown in Fig. 11.33a. Acrylic was selected as the structural material due to its decent strength, light weight, good machinability, and low cost. And the total number of the units in a 3D-TENG can be expressed as: $N = 4n$, where n is the number of pinned fingers of a TENG. Eight identical springs were employed to bridge the moveable and pinned fingers. As shown in Fig. 11.33b, the voltage output is almost constant for 3D-TENGs with $n = 1$–5, which is attributed to the electrically parallel connection among all of the units. However, the current output is a monotonically increasing function of n. Such a dramatic current enhancement is mainly owing to the operating synchronicity of all units. In the meanwhile, a monotonically increasing relationship was also observed between the current output and the effective contact area ΔS, as shown in Fig. 11.33c. To enhance the output current for the TENG-based mechanical energy harvesting, another rationally designed device with integrated rhombic gridding can also greatly improve the total current output owing to the multiple unit cells connected in parallel. The structure of integrated rhombic

gridding-based TENG is shown in Fig. 11.33d, in which, the total number of unit cells in one TENG can be expressed as: $N_{total} = 2n^2$, where n is the number of unit cells along the edge length. Each polyethylene terephthalate (PET) sheet with a thickness of 600 mm is cut half through and then locked into each other to form the framework of TENG. In each unit cell, an aluminum thin film with nanoporous modification plays dual roles as a contact electrode and a contact surface and PTFE with back-coated copper plays as another contact surface. As indicated in Fig. 11.33e, the current enhancement factor $\alpha$ is a function of the number of unit cells along the edge length, $\alpha = bn^2$. The fitting results render the coefficient $b$, a value of 1.66. Considering the nonideal experimental factors, such as humidity, particle contaminants in air, and other experimental imperfection, the observed results of enhancement factor are considerably approaching to the ideal value of $2n^2$, revealing the effectiveness of the integrated rhombic gridding structure for current enhancement. As illustrated in Fig. 11.33f, the accumulative induced charges also increase with n, which reach up to 142.68 μC within 2.75 s when $n = 3$, further indicating that the integrated rhombic gridding structure can dramatically enhance the electric output of the TENG. In addition, other TENGs have also been designed to enhance the power outputs, such as stacked triboelectric nanogenerator, self-powered flexible printed circuit (FPC) board with an integrated zigzag-shaped TENG, three-dimensional multilayered sliding TENG, as well as cylindrical TENG by segmentation design and multilayer integration (Wang et al. 2015a, b).

### 11.6.2 Triboelectric Nanogenerators as Self-Powered Active Sensors

The output performance of a TENG is greatly affected by magnitude/frequency of the external mechanical stimuli, and the pressure applied onto the device is among the most critical parameters. Hence, the most straightforward application for TENG-based active sensors would be the quantification of external pressure/touch. Figure 11.34a shows a self-powered tactile sensor based on flexible thin film materials, in which a layer of polyethylene terephthalate (PET) deposited with ITO electrodes on both sides formed the structural backbone of the triboelectric sensor (TES). Fluorinated ethylene propylene (FEP) thin film was applied on top as a triboelectric layer for contact electrification with a foreign object. Vertically aligned polymer nanowires (PNWs) were created on the FEP layer (Fig. 11.34b) to assist the generation of triboelectric charges. To evaluate the performance of the TES to a contact event, a square-shaped TES (Fig. 11.34c) was utilized to detect a piece of metal by cyclic contact and separation. As presented in Fig. 11.34d, at an applied pressure of 0.03 kPa, the TES produced a uniform output voltage with a maximum magnitude of 35 V. As the contact pressure increased, the output voltage was raised to 50 V when the contact pressure approached 10 kPa (Fig. 11.34e). This increasing behavior was attributed to the increase of effective contact area between the metal object and the TES. To demonstrate the practical application of the tactile sensor, a complete wireless sensing system was developed through integrating the TES with a signal-processing circuit. The system relied on the output voltage from the TES to

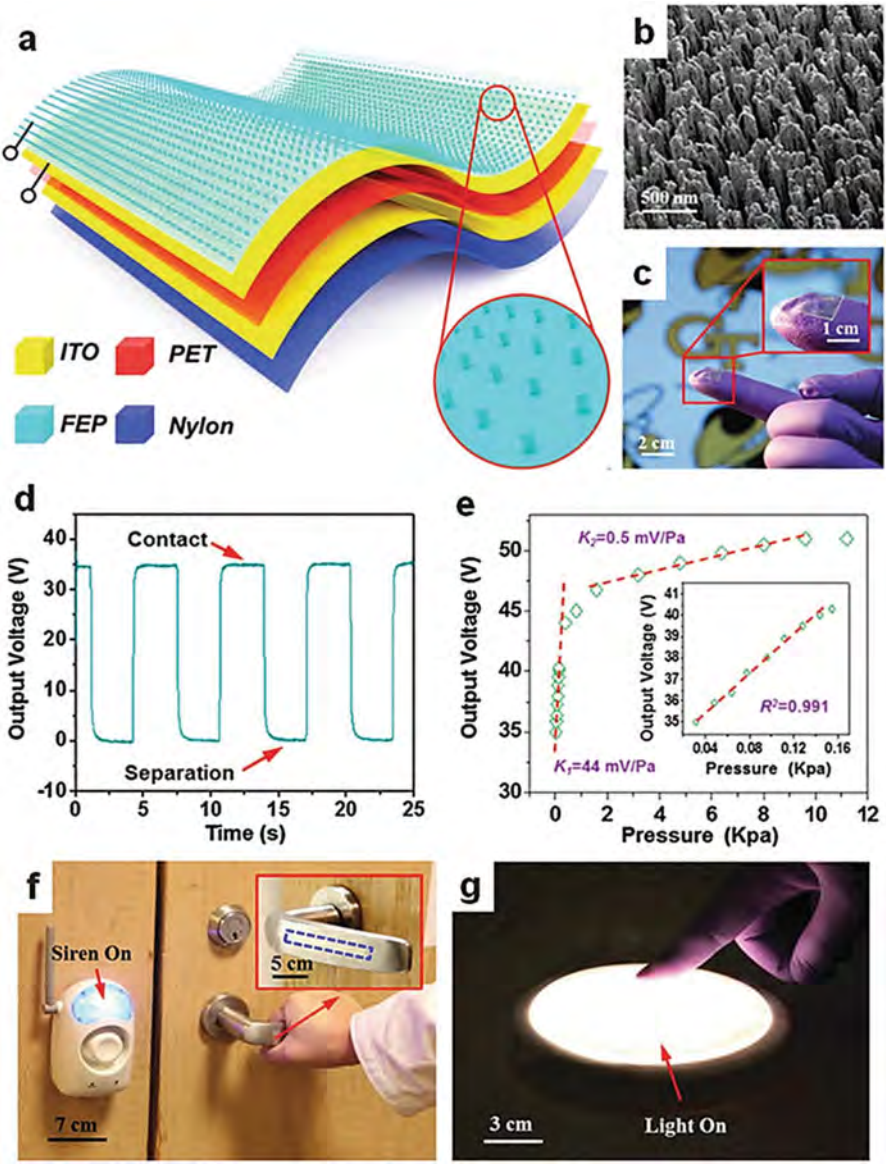


**Fig. 11.34** A self-powered, flexible, and ultrasensitive tactile sensor (Adapted with permission from Wang et al. (2015b) (Royal Society of Chemistry)): (**a**) The schematic structure of the tactile sensor. (**b**) The SEM image of the polymer nanowires created on the surface of the FEP thin film. (**c**) The photograph of the tactile sensor for measuring the contact event from a foreign object. (**d**) The measurement of open-circuit voltage with a cyclic contact force of 20 mN. (**e**) The output voltage under different contact pressures. Inset: an enlarged view of the summarized results at a low-pressure region. (**f**) A photograph showing that the TES was integrated with a signal processing circuit to turn on the siren alarm when a human hand touched the door handle. (**g**) A photograph showing that the TES was integrated with another signal processing circuit to turn on light when it was contacted by human fingers

trigger an IC timer that controlled a wireless transmitter for remotely switching a siren alarm. As indicated in Fig. 11.34f, the sensing system immediately started operation once a human hand touched the door handle. Through substituting other functional electronics for the wireless transmitter in the circuit, the sensing system could be adopted for more purposes. For example, a touch-enabled switch for a panel light was successfully developed and is shown in Fig. 11.34g. The TES in this work had a number of other unique advantages, including ultrahigh sensitivity, self-generated output, location independence, and outstanding robustness. In addition, the TES was generally applicable to objects made from various materials, indicating the widespread adaptability of the TES in a variety of circumstances. Therefore, TENG-based self-powered pressure/touch sensors can be utilized for a variety of applications, such as healthcare and security. Several typical examples include a membrane-based triboelectric sensor for health monitoring, a skin-friendly human–machine interfacing, and a paper-based anti-theft sensor (Wang et al. 2015a, b).

A mechanical motion can be described with a series of parameters, like displacement, velocity, acceleration, etc. Sensors for detection of these parameters are vitally important for mechanical systems with moving parts. TENGs have been developed to generate electricity from different types of mechanical motions, such as linear sliding, rotation, and rolling. Since the frequencies and amplitudes of the generated electrical signals are all directly related to the parameters of the input mechanical motions, TENGs can play the role of self-powered active motion sensors. Even if such motions are located in concealed locations, TENGs can be utilized to track the trajectory and detect the instantaneous parameters of the motions. Figure 11.35a shows a self-powered, one-dimensional displacement and speed sensor with high spatial resolution, large dynamic range, and long detecting distance. The motion sensor consisted of two micro-grating layers with identical patterns. The bottom layer was an etched silicon wafer coated with aluminum as the bottom electrode and silicon dioxide as one of the triboelectric material to generate positive charges; the top layer was a patterned SU-8 film on a glass slide as a supporting substrate, which was subsequently coated with ITO and Parylene film as the top electrode and the other triboelectric material to generate negative charges, respectively. The detailed structure of the as-fabricated devices can be found in the SEM images shown in Fig. 11.35b, c, respectively. The relative motion between two gratings results in periodic separation of two micro-grated triboelectric materials that are oppositely charged through triboelectrification. As a result, an alternating electric signal between the two electrodes placed was detected due to electrostatic induction. During the movement, $V_{OC}$ measured between the two electrodes (Fig. 11.35d) alternated between 0 and ~160 mV periodically, and the real time displacement could be calculated by counting the number of voltage peaks and multiplying the number with the width of each grating (200 mm). As presented in Fig. 11.35e, the detected displacement increased linearly with time, and the real time motion speed could also be calculated by dividing the grating width by the time interval between two adjacent peaks. Starting from a status with complete overlap, a step motion test with each step of 5 mm was performed to investigate the resolution of the displacement sensor. The sensitive region was found to be from 10 to 190 mm, where each

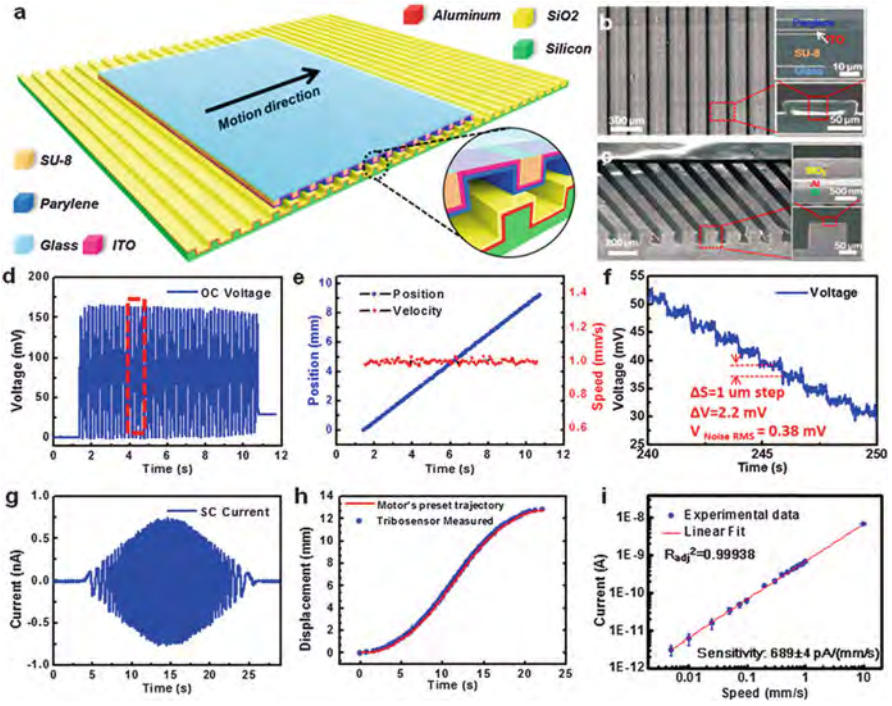


**Fig. 11.35** Micro-grated triboelectric nanogenerator as a nanometer resolution self-powered linear displacement sensor (Modified with permission from Zhou et al. (2014) (Wiley—VCH Verlag GMBH & Co.): (**a**) The structure of a TENG-based self-powered displacement sensor, with a pair of micrograting, the inset illustrates the detailed information on layers. (**b**) SEM images of the top micrograting with a glass slide substrate. The insets show the cross section: the ITO layer on top of the patterned SU-8 photoresist serves as the top electrode, and the outmost layer is Parylene film serving as an electronegative triboelectric layer. (**c**) SEM images of the bottom micrograting. The insets show the cross section profile: the etched Silicon is coated with Al as a bottom electrode and SiO2 as an electropositive triboelectric layer. (**d**) The OC voltage signals acquired from a displacement of 9.2 mm at a preset speed of 1 mm/s. (**e**) The real time displacement and speed derived from the measured voltage signal. (**f**) Step motion with 1 mm per step in the sensitive region (10–190 mm) can be clearly resolved through the OC voltage signal. Given the RMS value of noise (0.38 mV), and the voltage change corresponding to 1 mm step motion (2.2 mV), the resolution can be calculated to be 173 nm. (**g**) The SC current signals acquired from a non-uniform motion (decelerate–uniform speed–deceleration). (**h**) The preset motor's trajectory and the real time displacement detected by the motion sensor. (**i**) A plot of SC current as a function of motion speed from 5 to 10 mm/s with a fitted sensitivity of $689 \pm 4$ pA (mm/s)

step motion of 1 mm could be clearly identified from the voltage variation, as displayed in Fig. 11.35f. The change in the voltage for each step was about 2.2 mV, and the root mean square (RMS) of the noise $V_{noise}$ at 1 Hz is 0.38 mV. Consequently, the displacement resolution at a bandwidth of 1 Hz was determined to be 173 nm. The measured $I_{SC}$ could also serve as the sensing signal for the displacement and speed, as shown in Fig. 11.35g. The real time displacement could be derived by counting the number of zero-crossings, and the measurement

results matched very well with the preset trajectory (Fig. 11.35h). On the other hand, the amplitude of $I_{SC}$ also helped to quantitatively determine the real time speed, given a small aspect ratio of the dielectric layer. Figure 11.35i shows the plot of the magnitude of the output current with motion speed from 5 to 10 mm/s, and a linear fitting indicated its sensitivity of 679 pA $(mm/s)^{-1}$. The resolution in dynamic speed detection was 1.2 mm/s given the RMS value (0.8 pA) of the noise. The resolution for both displacement and speed sensing can be further improved by reducing the grating period. This approach of self-powered displacement/speed sensing distinguishes itself from the existing technologies by nanometer resolution, long detecting range, and nonoptical compacted structure, showing extensive potential applications in automation, manufacturing, process control, etc. (Zhou et al. 2014, Wang et al. 2015a, b).

Based on the triboelectric effect between human fingers and keys, the intelligent keyboard (IKB) could convert typing motions into localized electric signals that could be identified as personalized physiological information. The core part of the IKB was composed of multilayered transparent thin film materials to form a typical single-electrode TENG. A layer of polyethylene terephthalate (PET) was deposited with ITO electrodes on both sides, and the top ITO was laminated by a layer of FEP as the triboelectric material for contact electrification with bare human fingers (Fig. 11.36a). A nanowire structure was created on the FEP surface to enhance the effective contact area (Fig. 11.36b), which also introduced a self-cleaning surface. Figure 11.36c shows a photograph of a fully assembled IKB with the same size as a commercial keyboard. The working principle of the IKB as an energy harvester was similar to the single-electrode TENG. The contact of human skin with the FEP surface would leave the finger positively charged, and the FEP negatively charged. The finger movement during typing would then induce change in the potential difference between the pair of ITO electrodes, driving electrons to flow through the external load or data collection system. A typical output profile is presented in Fig. 11.36d, in which the channel located on the key struck by the finger exhibited an instantaneous voltage peak of about 10 V, which was much larger than that in the rest of the channels. The recognition of key striking could even be recognized by screening the data using a Pauta Criterion Method, and simultaneously visualized on the display without noticeable delay (Fig. 11.36e). The performance of the authentication biometrics was characterized through two error rates: False Rejection Rate (FRR) and False Acceptance Rate (FAR). Here, the FRR is the probability that the system incorrectly rejects access of an authorized person, due to failing to match the user template. While FRR is the percentage of valid inputs, which are incorrectly rejected. And the Pearson correlation coefficient was selected as the classification threshold to evaluate the behavioral biometric authentication system, as shown in Fig. 11.36f. The FRR was increasing with the elevated threshold, while FAR follows a reverse trend, and their intersection indicated the Equal Error Rate (EER) point. In the meanwhile, the Receiver Operating Characteristic (ROC) curve is demonstrated in Fig. 11.36g. Given its exceptional authentication capability, the IKB was able to identify the individual typing characteristics, making it practical as a highly secured

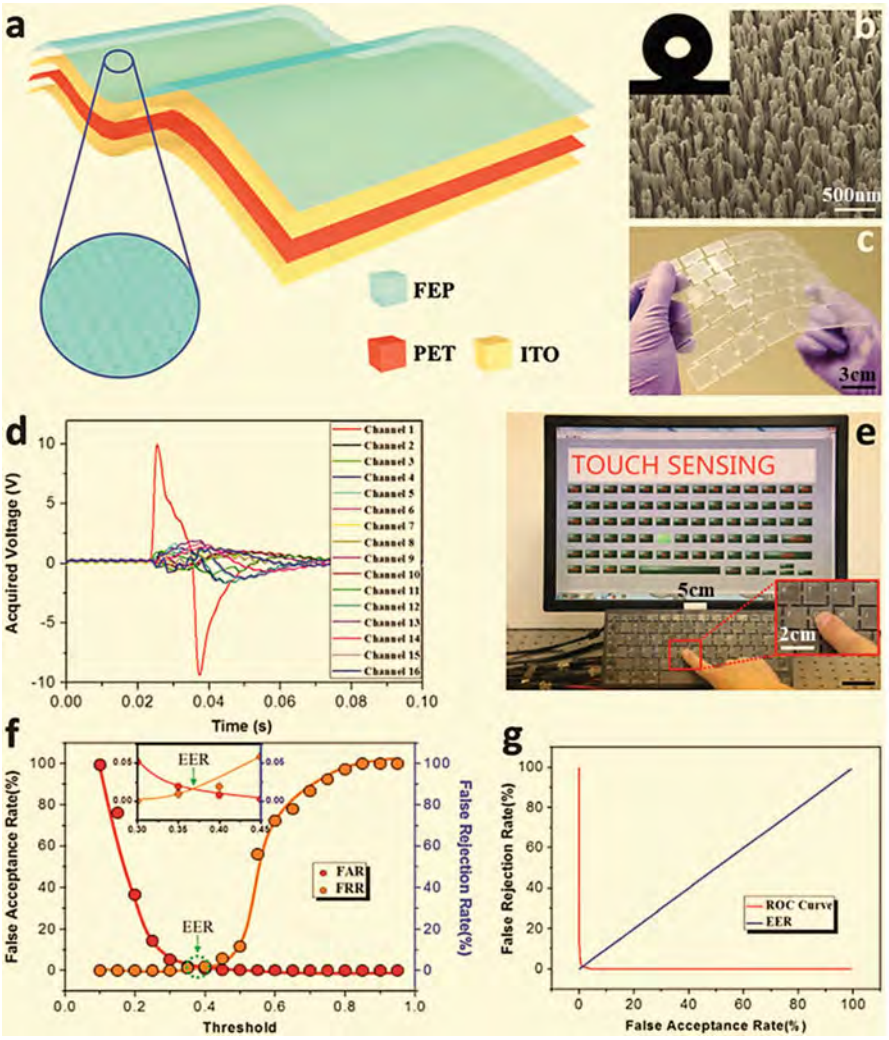


**Fig. 11.36** Personalized keystroke dynamics for self-powered human–machine interfacing (Adapted with permission from Wang et al. (2015b) (Royal Society of Chemistry)): (**a**) Schematic illustrations of the KFE. Inset: an enlarged schematic of FEP nanowires on the top surface. (**b**) SEM image of FEP nanowires. Inset: contour of the resting droplet for surface static contact angle measurement. (**c**) Photograph of a flexible and transparent KFE. (**d**) The system acquired output voltage signals when the key "T" was stroked. (**e**) A photograph demonstrating the IKB for real-time keystroke tracing and recording. A continuously typing string "TOUCH SENSING" was recorded in real time without uncomfortable delay. Inset: an enlarged view of the key "G" being stroked. (**f**) Evaluation of the performance of the biometric authentication system using triboelectrification enabled keystroke dynamics. The variation of FAR and FRR is related to the threshold. Inset: an enlarged view of the EER point, which indicates a remarkably low EER value of 1.34% at the threshold of 0.37. (**g**) Receiver operating characteristic (ROC) curve of the biometric authentication system using triboelectrification enabled keystroke dynamics. The false rejection curve is plotted as a function of the false acceptance curve

authentication system based on behavioral biometrics TENG has further been improved and extended into a bionic membrane sensor (BMS) with both security authentication and healthcare monitoring functionalities (Chen et al. 2015; Wang et al. 2015a, b).

### 11.6.3 Triboelectric Nanogenerators for Blue Energy Applications

Many approaches of triboelectric nanogenerators have been explored to effectively collect various types of water-based power sources, namely blue energy harvesting. Figure 11.37 summarizes several unique prototypes to achieve high output power, low cost, convenient fabrication, good flexibility, excellent stability and robustness, and possibility to scale up. Despite the state-of-the-art progress, more endeavors are still highly desired to further investigate in this field to improve the performance of the water-TENG towards practical applications in blue energy harvesting (Wang et al. 2015a, b).

The concept of water–solid contact electrification was first employed for energy harvesting; the device structure of this water-TENG is schematically illustrated in

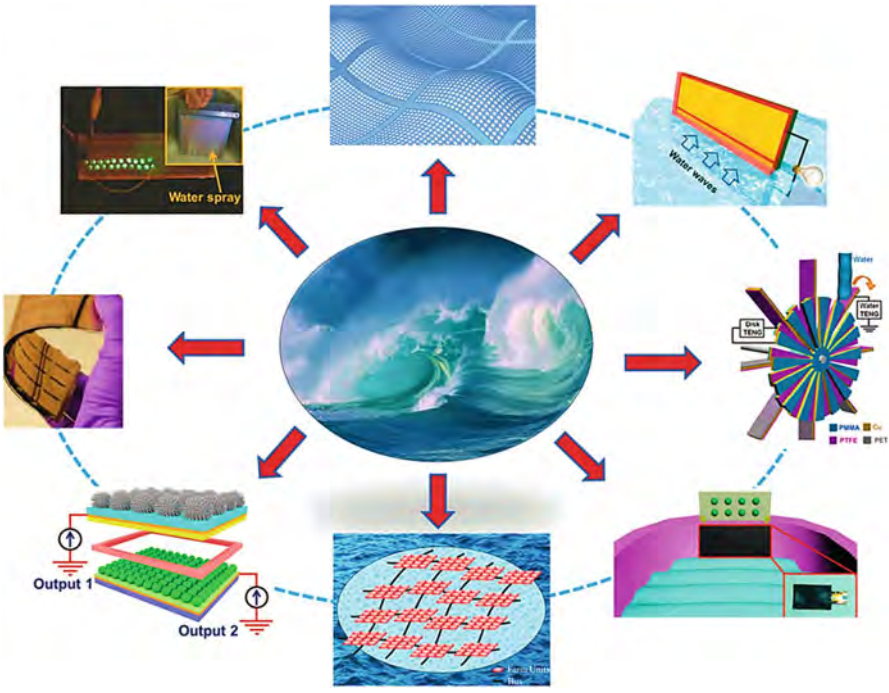


**Fig. 11.37** A schematic diagram exhibiting the state-of-the-art progress of TENGs for harvesting blue energy (Adapted with permission from Wang et al. (2015b) (Royal Society of Chemistry))

Fig. 11.38a, in which one dielectric layer of a typical contact-mode TENG was replaced with water. The cyclic contact between the PDMS layer and water surface would generate negative charges on the PDMS layer and positive charges on the water surface, and the periodical separation of the two charged surfaces resulted in change in potential difference between the two copper electrodes under OC conditions, and external electrons flow under SC conditions. Micropatterned pyramid array was created on the inner surface of the PDMS layer to enhance the effective contact area (Fig. 11.38b), and this approach should be extraordinarily applicable in this case owing to high ductility of water. Driven by a linear motor at a frequency of 2 Hz and a magnitude of 1.5 cm, the water-TENG was enabled to produce a $V_{OC}$ and $J_{SC}$ of 82 V and 1.05 mA/m$^2$, respectively. The optimized output power density reached up to 50 mW/m$^2$ at 5 Hz. The frequency response of the water-TENG was significantly different from that of the solid material-based TENG, in that the movement of the PDMS film contacting and separating from water would generate a water wave, which would disturb the contact area with the PDMS film. Figure 11.38c, d shows the frequency response of the measured $J_{SC}$ and $V_{OC}$, respectively. Both of them decreased first from 2 to 3 Hz and then increased with frequency from 3 to 5 Hz. On the contrary, for solid-material-based TENG, $J_{SC}$ would keep increasing with the frequency and $V_{OC}$ would remain almost unchanged. The difference of frequency response implied a unique feature of the water-TENG. It was further demonstrated that the water-TENG could serve as a self-powered temperature and ethanol sensor, through real time measurement of its output performance. Another basic prototype of water-TENG was based on asymmetric screening of the triboelectric charges on a nanostructured hydrophobic thin film surface, as exhibited in Fig. 11.38e. Two parallel strip-shaped electrodes were deposited on one side of a FEP thin film, and they were separated with a fine gap in between. The other side of the FEP thin film was modified with nanowire structures for improving the effective contact area. The operation of the water-TENG relied on a repetitive emerging–submerging process with traveling water waves, in which the coupling between triboelectrification and electrostatic induction drove alternating flows of electrons between electrodes. Quantitative assessment of the output performance was also stimulated by a linear motor, and the generated $V_{OC}$ and $I_{SC}$ were 160 V and 3 mA, respectively, with an optimum output power of 0.12 mW at a velocity of 0.5 m/s (Fig. 11.38f).

A higher velocity, finer electrode features, and lower ion concentration are all favorable for the overall output performance, though further systematic investigations on the charge generation process were still desirable to provide in-depth insights. To demonstrate the applicability of the water-TENG in real-world situations, an integrated TENG with a scaled-up design was further tested in a normal environment where energy from ambient water motions was harvested. The integrated water-TENG consisted of six strip-shaped electrodes and a total of five basic units were formed by any pair of adjacent electrodes. The electric output of each pair was first rectified and then constructively superimposed through a parallel connection. It was then inserted into a traveling wave created by a large container, or placed beneath a sprinkler head with sprayed water droplets. The generated output

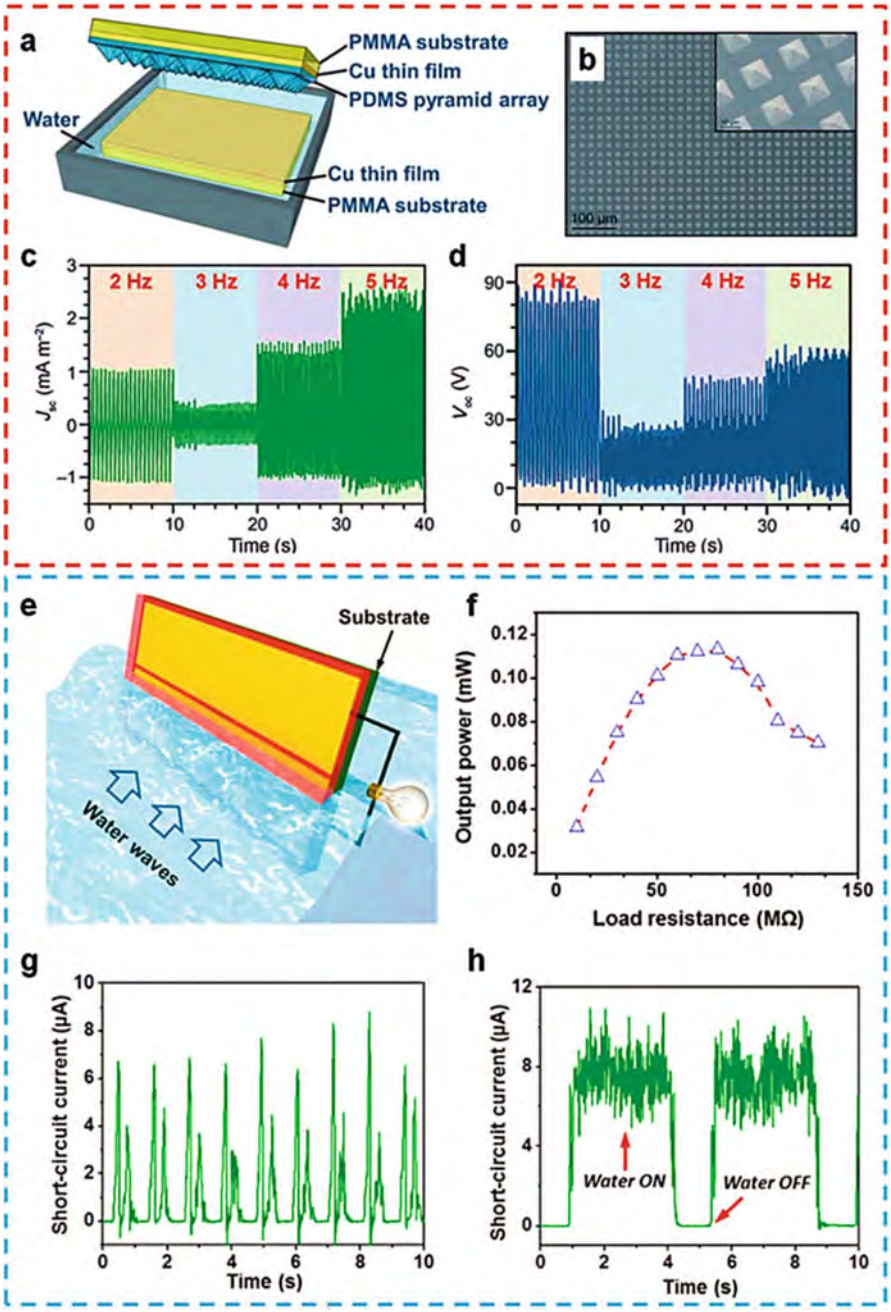


**Fig. 11.38** TENGs for harvesting water wave energy (Adapted with permission from Wang et al. (2015b) (Royal Society of Chemistry)): (**a**) Schematic diagram of the water-TENG based on contact electrification between water and micropatterned PDMS. (**b**) SEM image of patterned PDMS

current from both cases is shown in Fig. 11.38g and h, respectively. The rectified current from water droplets (Fig. 11.38h) showed almost continuous DC behavior, which was attributed to numerous droplets and the merging of the large number of current peaks. In addition to these two fundamental structural designs, a lot of other prototypes were also proposed for high-performance blue energy harvesting, such as dual-mode TENG fabricated based on the superhydrophobic $TiO_2$ layer and polymer thin films to collect both the electrostatic and mechanical energy from flowing water; hybrid water-TENG relied on the coupling of contact separation and single-electrode operation modes (Lin et al. 2013; Wang et al. 2015a, b).

Besides water wave energy, wind energy is also a type of widely existing power source from the natural environment. A flutter-driven TENG was developed for effective wind energy harvesting to sustainably drive electronic devices in outdoor environments. The structure of the TENG was composed of a fluttering flexible flag and a rigid plate, as shown in Fig. 11.39a. The flag was a gold-coated conductive fabric that served as the fluttering body, and PTFE with a counter electrode was attached onto the rigid plate to form a contact-mode TENG. Natural wind would introduce the contact–separation behavior between the flag and the rigid plate to generate electricity. As shown in Fig. 11.39b, a flexible woven flag exhibited oscillations with a node. From the top to the node, the oscillation amplitude was very small, but it was subject to increase as a traveling wave propagated towards the trailing edge below the node. To bring up a self-sustained contact-propagation-separation between two triboelectric layers through high-frequency flag fluttering, the counter plate was simply placed next to the flag flutter within a critical distance, and the coupled interaction between the two surfaces was systematically investigated by varying their dimensions. The stability boundary could be characterized by a regime map shown in Fig. 11.39c, and two distinct contact–separation modes were observed in the plot. The transition from the single-contact mode in region A to the double-contact mode in region B occurred as the dimensionless mass decreased, which could be tuned by adjusting the length of the flag. The flutter-driven TENG produced a high output of 200 V and 60 mA at a wind speed of 15 m/s, with an average power density of 0.86 mW. To demonstrate its wind energy-harvesting capability in outdoor environments, a robust packaging module of the flutter-driven TENG was integrated (Fig. 11.39d) and securely mounted onto the roof of a moving vehicle. The TENG was enabled to charge a 1000 mF capacitor to 30 V in 25 min when the vehicle was traveling at 70 km/h (Fig. 11.39e), thus demonstrating its

**Fig. 11.38** (continued) pyramid array. The inset is an SEM image with higher magnification. (**c**, **d**) Influence of contact frequency between patterned PDMS pyramid array and deionized water on the (**c**) JSC and (**d**) VOC generated by the water-TENG. (**e**) Schematic of a substrate-supported TENG positioned in water waves. The up-and-down movement of the surrounding water body induces electricity generated between the two electrodes. 135 (**f**) Average output power of the water-TENG with increasing load resistance between electrodes. (**g**) Rectified short-circuit current of the integrated water-TENG when it interacts with water waves at a frequency of ~0.7 Hz. (**h**) Rectified short-circuit current of the integrated water-TENG when it interacts with falling water drops

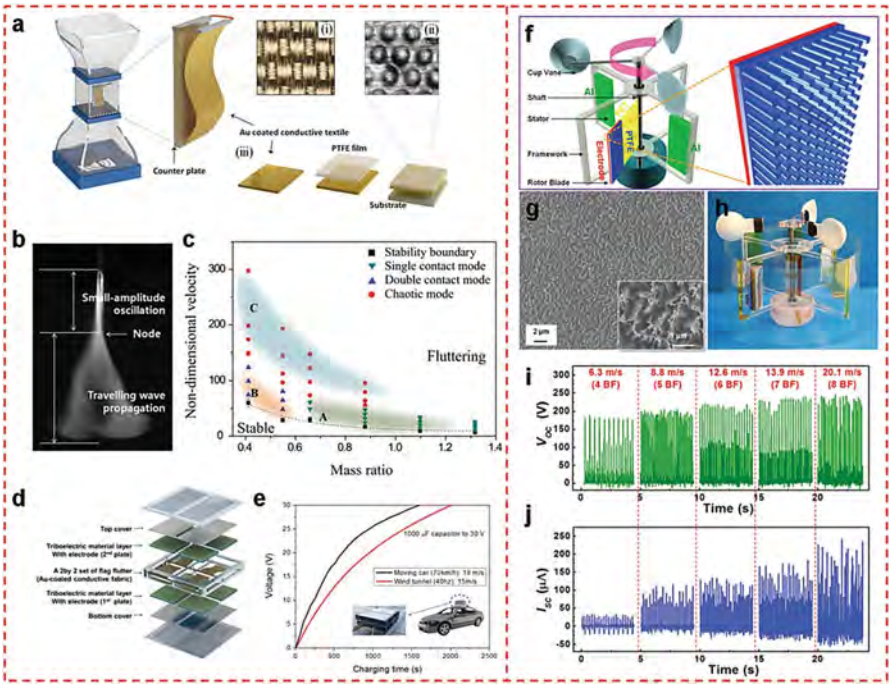


**Fig. 11.39** TENGs for harvesting the ambient wind energy (Modified with permission from Wang et al. (2015b) (Royal Society of Chemistry)): (**a**) Schematic diagrams of a wind tunnel and the structural design of a flutter-driven triboelectric generator including surface characteristics of (*i*) a highly flexible flag and (*ii*) a counter plate and (*iii*) the fabrication of the counter plate. (**b**) Fluttering images of a stand-alone configuration of dimensions 7.5 × 5 cm as captured using a high-speed camera. (**c**) The regime map of the dynamic interaction between a flag and a plate. (**d**) Schematic of the stacked TENG-packaging module with total eight units. (**e**) Comparison of the charging times of a 1000 mF capacitor using a stacked flutter-driven TENG system when charging on the moving vehicle and when charging in the wind tunnel system. (**f**) The schematic diagram showing the structural design of the rotary TENG, with the enlarged picture showing nanowire structures on the surface of PTFE. (**g**) The SEM image of the PTFE surface with etched nanowire structures. The inset is an SEM image at high magnification. (**h**) A photograph of the fabricated rotary TENG. (i, j) Influence of the wind speed on the electrical outputs. (**d**) *V*OC and (**e**) *I*SC under different wind speeds from 6.3 m/s (4BF) to 20.1 m/s (8BF)

operation in an open environment under various wind conditions. A rotary TENG was also developed to harvest wind energy assisted by the wind-driven rotation of cup vanes, as shown in Fig. 11.39f. The continuous shaft rotation introduced cyclic contact and consecutive sliding between Al foils and nanostructured PTFE film (Fig. 11.39g, h). Hence, the working principle of this rotary TENG relied on coupling of vertical contact–separation and lateral sliding modes. With a wind speed of ~15 m/s, its $V_{OC}$ and $I_{SC}$ were up to 250 V and 0.25 mA, respectively, corresponding to a maximum power density of ~39 W/m$^2$. Additionally, the rotary TENG could serve as a self-powered wind speed sensor (Fig. 11.39i, j). As expected,

$I_{SC}$ increased drastically with rising wind speeds, but $V_{OC}$ also showed slight elevation as the wind speed went up. This result could be explained by the change in the surface charge density. With higher wind speed, the polymer thin films would obtain higher rotational torque and thus a larger contacting force, which led to more intimate contact between two surfaces, resulting in a higher surface charge density (Bae et al. 2014; Wang et al. 2015a, b).

## 11.7 Hybridization and Integration of Energy Harvesters

Hybrid energy harvesters for simultaneously harvesting multiple types of environmental energy have been developed because of their synergetic output performances. Some hybrid cells have been accordingly demonstrated for harvesting mechanical and solar energy, mechanical and thermal energy, thermal and solar energy, and mechanical, thermal, and solar energy. For integrated energy harvesters of two or more such sources, electric circuit design should be considered, because solar cells and thermoelectric generators generate direct current (DC) electricity, while piezoelectric, triboelectric, and pyroelectric generators usually generate alternating current (AC) electricity. In the case of AC electricity, a rectification diode is required to convert AC into DC electricity. Moreover, impedance matching depending on materials and operation frequencies using resistive load to the piezoelectric generators, pyroelectric generators, and triboelectric generators is important to achieve maximum power output (Lee et al. 2016).

### 11.7.1 Mechanical and Solar Energy

Multi-type energy harvesters using both mechanical and solar energy have been especially intensively developed based on piezoelectric, pyroelectric, triboelectric, and PV effects. Figure 11.40a, b shows a hybrid energy harvester fabricated by infiltrating CdS/CdTe quantum dots into vertically aligned ZnO nanowires driven by sound in the frequency range of 35–1000 Hz and solar energy. Similar hybrid energy harvesters were also demonstrated using acoustic waves and pressure for the piezoelectric effect, based on PVDF and ZnO, with various kinds of solar cells such as DSSCs, quantum dot solar cells, silicon (Si) solar cells, and organic–inorganic hybrid solar cells. TENG-based multi-type energy harvesters have also received great attention because of their high output power and easy hybridization with other energy harvesters. Figure 11.40c, d shows a hybrid energy harvester based on the triboelectric effect and the PV effect. Micropyramid Si solar cells were fabricated with a protective layer consisting of a thin film of polydimethylsiloxane (PDMS) nanowires, which not only worked as a protective layer, but also as a triboelectric layer for harvesting mechanical energy. The hybrid energy harvester can be used for self-powered electrodegradation of rhodamine B and can also charge lithium (Li) ion batteries for operating small electronic devices (Lee et al. 2010, 2016).

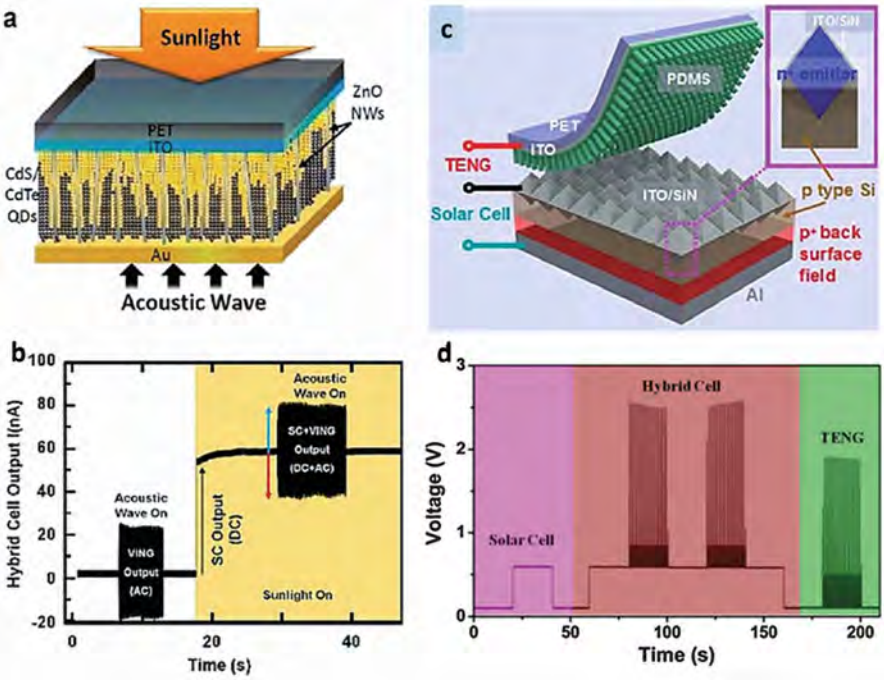


**Fig. 11.40** Mechanical and solar energy hybrid harvesters (Modified with permission from Lee et al. (2016) (Royal Society of Chemistry)): (**a**) Schematic diagram depicting a hybrid device with two different incoming energy sources, and (**b**) short-circuit current output signal of the hybrid cell. (**c**) Schematic diagram of the fabricated hybrid energy cell and scanning electron microscope (SEM) image of the fabricated Si pyramids, and (**d**) output voltage of the hybrid solar cell and TENG (after rectification) for harvesting both solar and mechanical energy

### 11.7.2 Mechanical and Thermal Energy

In some situations, mechanical vibrations or friction, and temperature fluctuations or a temperature gradient coexist, such as on the human body, during air flow, and in working engines/machines. As shown in Fig. 11.18, a stretchable piezoelectric–pyroelectric hybrid energy harvester was fabricated based on a micropatterned ferroelectric polymer P(VDF-TrFE) thin film, a PDMS-CNT composite, and graphene electrodes. The working mechanism for achieving the total output voltage was based on coupling of the piezoelectric and pyroelectric effects in terms of polarization and oscillation of the electric dipoles of P(VDF–TrFE). Stable pyroelectric output performance of the hybrid energy harvester for various stretchable modes showed the stretchability, mechanical durability, and robustness of the device owing to the micropatterned design. A Seebeck effect-based hybrid energy harvester to harvest both mechanical and thermal energy was also developed to convert wasted temperature gradient energy into electrical energy, by integration of the piezoelectric

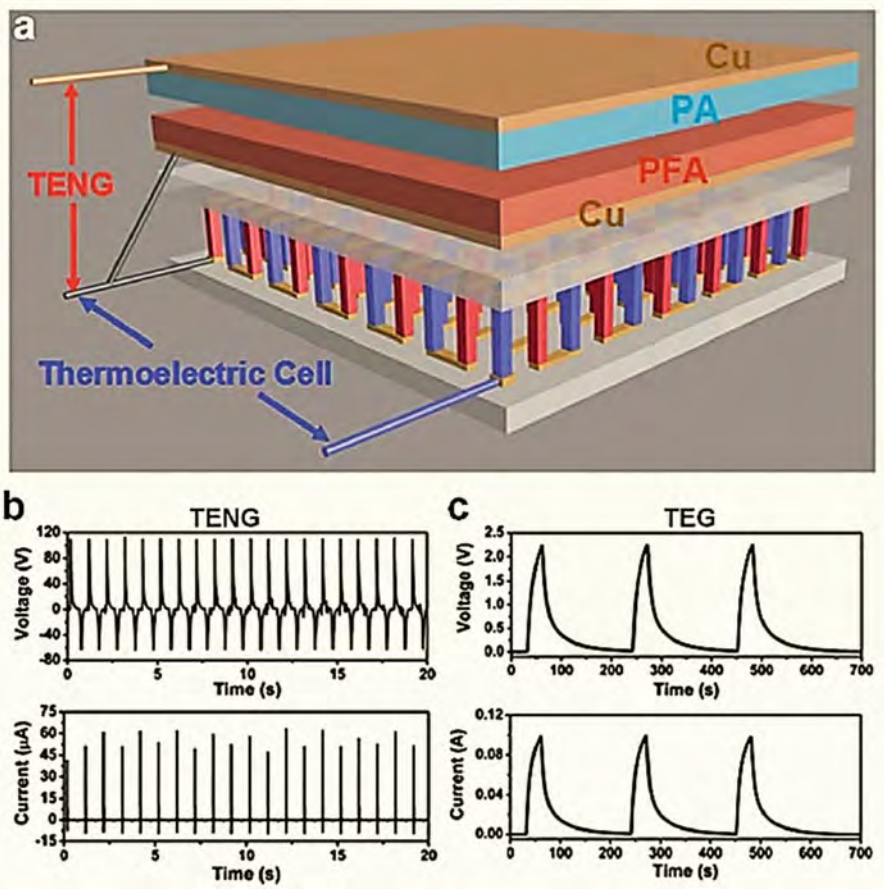


**Fig. 11.41** Mechanical and thermal energy hybrid harvester (Modified with permission from Yang et al. (2013) (Royal Society of Chemistry)): (**a**) Schematic diagram of the fabricated hybrid energy cell consisting of a triboelectric generator and a thermoelectric cell, (**b**) output voltage and current of the triboelectric generator, and (**c**) output voltage and current of the thermoelectric generator

and thermoelectric component devices, which were mounted on a flexible substrate. Furthermore, the energy-harvesting device can simultaneously harvest using both thermal and mechanical energy from the human body temperature gradient and mechanical movement. Figure 11.41 shows a hybrid generator that consisted of a TENG and a TEG, which could be used for self-powered water splitting to generate hydrogen (Fig. 11.41a). The hybrid energy harvester consisted of a polyamide (PA)-perfluoroalkoxy (PFA) polymer film-based TENG and a $Bi_2Te_3$-based TEG. The fabricated TENG generated output voltage and current of 110 V and 60 mA, and the TEG generated output voltage and current were 2.2 V and 0.1 A, respectively (Fig. 11.41b, c). This strategy provides a highly promising platform for harvesting both mechanical and thermal energy simultaneously and individually, and utilizing it

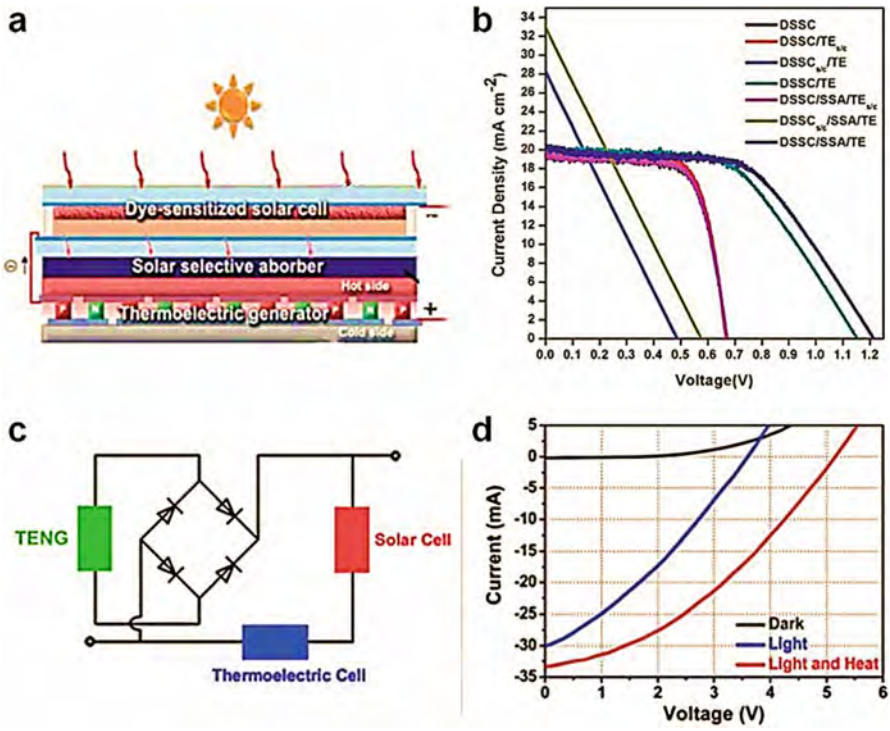


**Fig. 11.42** Solar and thermal energy hybrid harvester (Modified with permission from Lee et al. (2016) (Royal Society of Chemistry)): (**a**) Schematic illustration of a solar-thermoelectric hybrid device and (**b**) photocurrent density–voltage (J–V) characteristic curves of the DSSC/TEG hybrid device and of the component devices with the other component short-circuited. (**c**) Schematic diagram of the hybrid energy cell and (**d**) current–voltage characteristics of the hybrid energy cell under different conditions

for wireless sensors, temperature imaging, medical diagnostics, power sources for biomedical applications, personal electronics, sensor networks, and micro-/nano-systems (Yang et al. 2013; Lee et al. 2016).

### 11.7.3 Thermal and Solar Energy

Hybrid cells for harvesting thermal and solar energy are also the most conventional energy-harvesting technology, such as thermoelectric-solar hybrid generator made with Si or DSSC solar cell and TEG. Figure 11.42 shows a thermoelectric solar hybrid energy-harvesting system with a series connected DSSC, a solar selective absorber (SSA), and a TEG. The conversion efficiency of the solar cell was greatly increased by using the SSA and the TEG to utilize residual sunlight transmitted through the DSSC. The hybrid device, comprising a DSSC for high-energy photons and an SSA-coated thermoelectric generator for low-energy photons, yielded overall

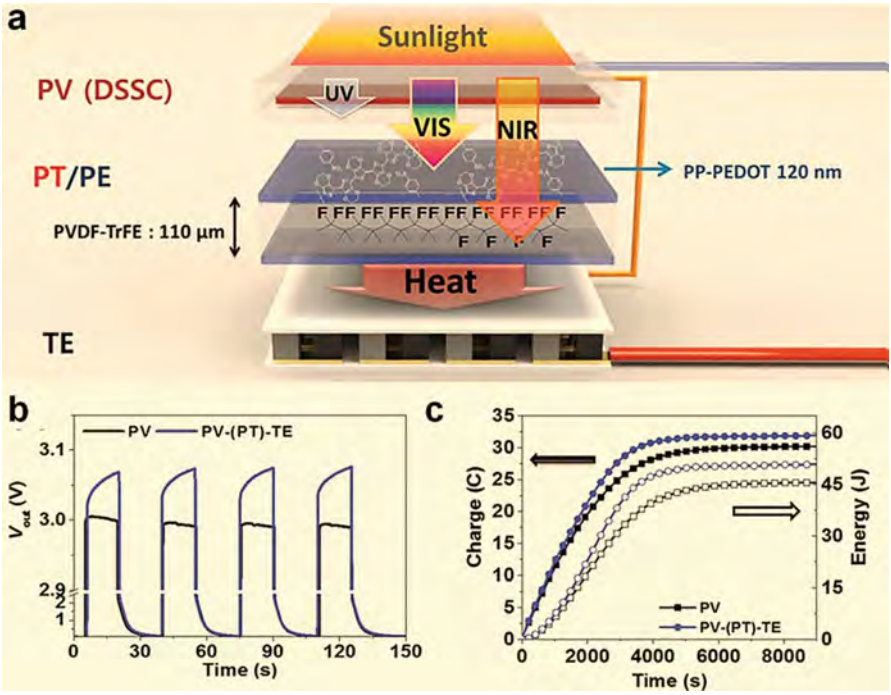


**Fig. 11.43** Solar and pyroelectric energy hybrid harvester (Modified with permission from Park et al. (2015). Copyright © 2015 American Chemical Society): (**a**) Illustration of a photovoltaic and photothermal pyro-thermoelectric device. (**b**) Output voltage of a PV and PV–TE series connected device. (**c**) Output and accumulated energy of a capacitor (10 F, 5.4 V) charged by PV and by the PV–TE series connected device in the hybrid system (filled circles and squares, charge; open circles and squares, energy)

conversion efficiency higher than 13% (Fig. 11.42b). Figure 11.42c shows a hybrid cell that was composed of a $Bi_2Te_3$-based TEG and a Si solar cell, which could be used to simultaneously and individually harvest thermal and solar energy. Under light illumination, the output voltage of the hybrid energy cell is about 3.5 V, and the output current is about 30 mA, based on the integration of six solar cells (Fig. 11.42d). Under light illumination on the solar cells and heat applied at the bottom of the thermoelectric cell, the total peak output voltage and current of these two components of the energy harvester reached 5.2 V and 34 mA, respectively. Figure 11.43 shows a hybrid cell based on a DSSC solar cell with a pyroelectric and thermoelectric device operated by photothermally generated heat (Fig. 11.43a). The photoconversion efficiency (PCE) was increased up to 20% under sunlight irradiation (AM 1.5G) using the transmitted light through the DSSC as a heat source that was converted into electricity by the pyroelectric and thermoelectric effects simultaneously by the photothermal poly(3,4-ethylenedioxythiophene) (PEDOT) electrodes. Interestingly, as PV works under sunlight, the output voltage from the PV device continuously decreased because of the fast recombination phenomenon during the PV operation (Fig. 11.43b). When the PV was combined with a TEG,

however, the total output voltage increased, due to thermoelectric power generation. Consequently, the reduced PV output performance was enhanced by the output of the thermoelectric generator in the hybrid device. This result was also confirmed by the charging of the capacitor. The plot (Fig. 11.43c) of the cumulative charges and energies in the capacitors demonstrates the enhanced performance of the PV–TE hybrid system (Park et al. 2015; Lee et al. 2016).

### 11.7.4 Coupling of Multiple Energy Sources

On the basis of nanomaterials in the wurtzite semiconductors, such as ZnO and GaN, electronics fabricated by using a piezopotential as a gate voltage are called piezotronics, with applications in strain/force/pressure-triggered/controlled electronic devices, sensors, and logic gates. The piezophototronic effect is a result of three-way coupling among piezoelectricity, photonic excitation, and semiconductor transport, which allows tuning and controlling of electro-optical processes by a strain-induced piezopotential (Wang 2010). In addition, the piezotronic effect—the coupling between the piezoelectric and semiconducting properties of nanowires, combines piezoelectric polarization with semiconductor properties and allows the direct and active interaction between devices and stimuli. This phenomenon inspires novel device applications and has led to an emerging field called piezotronics (Jenkins et al. 2015).

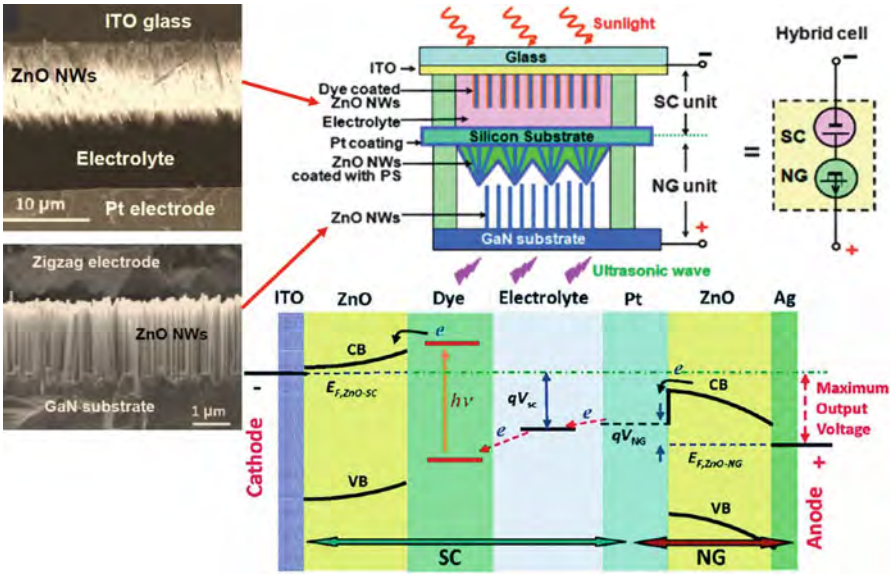


**Fig. 11.44** Electron energy band diagram of the solar-piezo hybrid cell, showing that the maximum output voltage is the sum of the voltages produced by the solar cell and the PENG (Modified with permission from Xu et al. (2009). Copyright © 2009, American Chemical Society). The abbreviations are as follows: conduction band (CB), valence band (VB), Fermi level (EF)

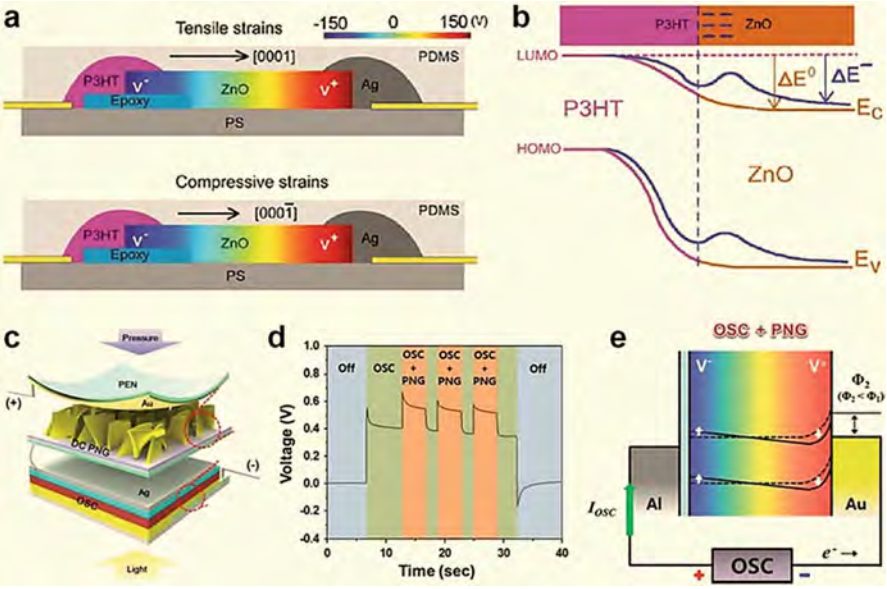


**Fig. 11.45** The coupling based on piezotronic effect (Modified with permission from Lee et al. (2016) (Royal Society of Chemistry)): (**a**) Piezopotential distributions in the stretched device of [0001] type and compressed device of [0001], and (**b**) schematic energy band diagram of P3HT/ZnO in the presence of negative piezoelectric charges. The blue line indicates the energy band diagram modified by the piezoelectric potential in ZnO. The negative piezoelectric charges can lift the energy band, resulting in a peak in the energy band. (**c**) Schematic illustration of the solar-piezo hybrid cell, (**d**) output voltage of the solar-piezo hybrid cell when pressure is applied periodically at intervals of 3.0 s for a period of 1.0 s, and (**e**) when pressure is applied to the PENG, the ZnO nanosheets exhibited a new band diagram: dashed and solid lines represent the band diagrams before and after applying the pressure on the PENG

A hybrid generator made with a piezoelectric potential enhanced PV cell has been developed based on piezophototronic effect. Its working principle is explained using the electron energy band diagram, as shown in Fig. 11.44. The maximum achievable output voltage is the difference between the Fermi level of the ZnO nanowires (NWs) in the DSSC and that of the ZnO NWs in the NG. The maximum output voltage is an integration of the output voltages of the NG and DSSC. The piezotronic effect was also demonstrated on the output voltage of flexible solar cells using poly (3-hexylthiophene-2,5-diyl) (P3HT)–ZnO microwire p-n heterojunctions on a flexible polystyrene (PS) substrate (Fig. 11.45a). The open circuit voltage $V_{oc}$ of the solar cell was characterized by tuning the strain-induced polarization charges at the interface between ZnO and P3HT. Figure 11.45b shows the mechanism of the piezotronic effect on solar cell performance under strain. The strain-induced piezoelectric potential is created under an externally applied strain, which modifies the energy band diagram at the interface of the p-n heterojunction, consequently modulating the performance of the device. The output power of solar cells could be enhanced by tuning the band profile under strain. Moreover, a hybrid system

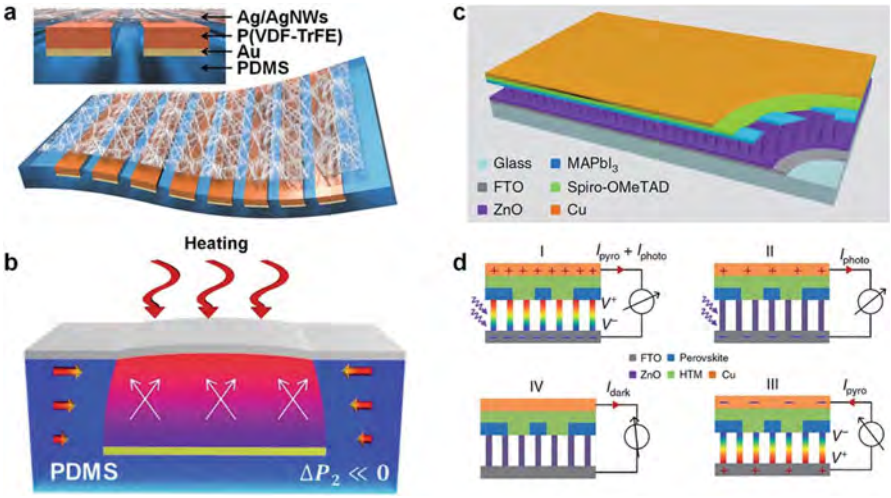


**Fig. 11.46** PNG enhanced by piezoelectric potential driven by thermally induced strain (Modified with permission from Lee et al. (2016) (Royal Society of Chemistry)): (**a**) Schematic illustration of the piezo–pyro coupling NG, and (**b**) piezoelectric and pyroelectric coupled potential-generating mechanism of the patterned P(VDF–TrFE) on a PDMS substrate. (**c**) Schematic illustration of the structure of self-powered ZnO/perovskite-heterostructured photodetectors (ZPH PDs), with FTO acting as the transparent electrode, and (**d**) schematic illustration of the working mechanism of the pyroelectric effect-combined with photoexcitation processes

consisting of a DC type PENG based on a two-dimensional (2D) ZnO nanosheet and an organic solar cell based on P3HT/[6,6]-phenylC61 butyric acid methyl ester (PCBM) is shown in Fig. 11.45c. The power generation performance of the serially integrated hybrid cell is synergistically enhanced by the help of a PENG, compared with the output power generated independently from the solar cell component under illumination (Fig. 11.45d). Figure 11.45e exhibits the mechanisms of power generation from the piezoelectric potential of the ZnO nanosheets. The energy band diagram in the ZnO nanosheet is modified under the influence of applied force and light. The photogenerated electrons from the organic solar cell can effectively flow through the PENG, owing to the reduced Schottky barrier height between the ZnO nanosheets and the Au electrode. Consequentially, Jsc from the solar-piezo hybrid cell also increases under application of pressure. Moreover, coupling of thermal/mechanical energy and thermal/solar energy-based energy harvesters and self-powered photocurrent were also explored. A PNG enhanced by piezoelectric potential driven by thermally induced strain is shown in Fig. 11.46a. Dramatic enhancement of the piezoelectric coupled PNG performance was observed, based on coupling of the piezoelectric and pyroelectric effects using different thermal expansion coefficients and micropatterned architectures (Fig. 11.46b). Using the light-self-induced pyroelectric effect in ZnO to modulate the optoelectronic processes, the performance of ultraviolet sensors can be enhanced (Fig. 11.46c, d). Thus, the coupling effect between mechanical, thermal, and light energy in an enhanced synergetic energy-harvesting system is not just simple multi-type energy harvesting,

such devices will also offer a promising approach for effectively harvesting multi-type energy for realizing multifunctional energy devices (Yoon et al. 2015; Lee et al. 2016).

### 11.7.5 Integration of Energy Harvesting and Storage Devices

Because of the naturally uncontrollable and unstable features of environmental mechanical, thermal, and solar energy sources, the converted electrical energy from energy harvesters is unstable and difficult to use as a direct power source for electronic devices. Usually, storage elements such as either capacitors or batteries are needed to stabilize and control the power output for direct applications (Lee et al. 2016).

Figure 11.47a shows a self-charging power cell using a Li-ion battery consisting of a $LiCoO_3$ cathode, $TiO_2$ nanotube anode, and PVDF piezoelectric polymer film as

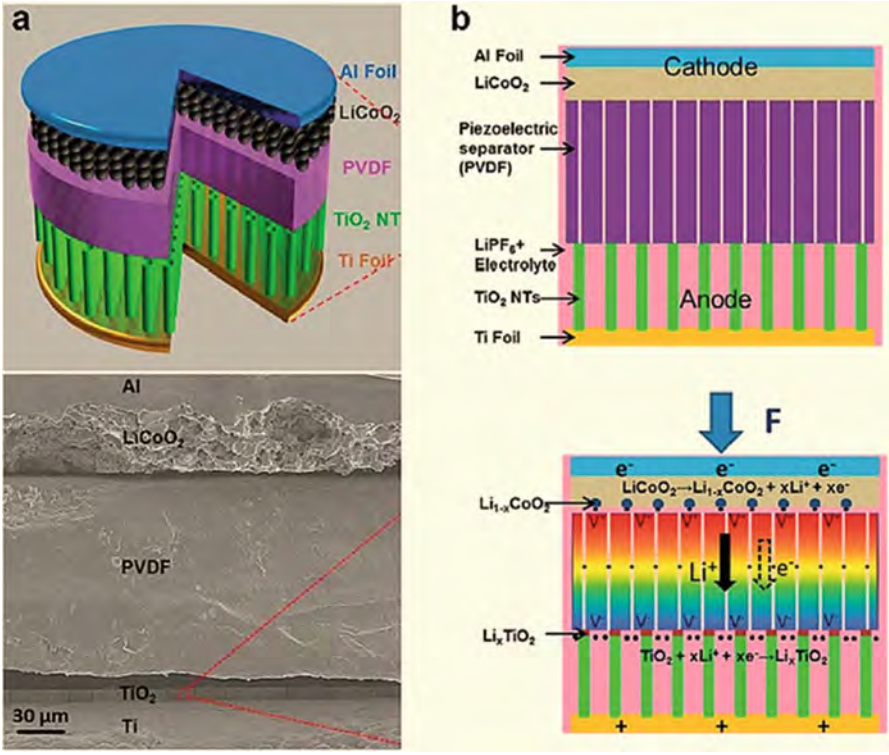


**Fig. 11.47** Integration of energy harvesting and Li-ion battery (Modified with permission from Lee et al. (2016) (Royal Society of Chemistry)): (**a**) Design of a self-charging power cell by hybridizing a PENG and a Li-ion battery, and (**b**) the working mechanism of the self-charging power cell driven by compressive strain

the separator. The strain-induced piezoelectric potential from the PVDF film acts as a charge pump to drive Li ions to migrate from the $LiCoO_3$ cathode to the $TiO_2$ nanotube anode with accompanying charging reactions at the electrodes, which can be defined as a piezo-electrochemical process. The fundamental mechanism that directly hybridizes the two processes into one, in which the mechanical energy is directly converted into electrochemical energy, without any intermediate step of first converting piezoelectric potential into electricity, is also proposed. Figure 11.47b shows the charging mechanism in detail, in which the polarized PVDF film creates a positive piezoelectric potential on the cathode side and a negative piezoelectric potential on the anode side under a compressive stress on the device. Li ions in the electrolyte drift from the cathode to the anode along the pores within the PVDF film in order to screen the piezoelectric field. The decreased concentration of $Li^+$ around the cathode will break the chemical equilibrium at the cathode ($LiCoO_2 \leftrightarrow Li_{1-x}CoO_2 + xLi^+ + xe^-$), so that $Li^+$ deintercalates from $LiCoO_2$ to form $Li_{1-x}$ $CoO_2$. Likewise, with increasing concentration of $Li^+$ around the anode, the chemical equilibrium at the anode ($TiO_2 + xLi^+ + xe^- \leftrightarrow Li_xTiO_2$) is also broken, and the Li ions will move in the opposite direction, where $Li^+$ will react with $TiO_2$ to form $Li_xTiO_2$. During this process, Li ions migrate from the cathode to the anode continuously, and the Li-ion battery is partially charged. When the distribution of $Li^+$ can balance the piezoelectric field, a new equilibrium is achieved, and the self-charging process is completed (Xue et al. 2012).

Figure 11.48a illustrates a piezoelectricity-driven self-charging supercapacitor power cell with functionalized carbon cloth as the supercapacitor electrode, which shows the potential for wearable applications of hybrid cells. The working mechanism of the piezoelectric-supercapacitor hybrid cell is slightly different from that of the piezoelectric-battery hybrid cell (Fig. 11.48b). When the external stress is applied to the piezoelectric-supercapacitor hybrid device, the remnant polarization of the PVDF film is changed. In order to balance the changed remnant polarization, charge carriers will migrate towards the electrode of the supercapacitor. Two factors are considered for the charging process. First, the increased bound charge density of the PVDF surface affects the distribution of the positive ions and negative ions in the electrolyte. The piezoelectric potential causes the redistribution of the ions and causes charges to accumulate on the surface of the supercapacitor electrode. Second, the piezoelectric potential drives the migration of hydrogen ions ($H^+$) and $SO_4^{2-}$ along the direction of the potential across the porous PVDF film. As the piezoelectric potential increases between the positive and negative electrodes due to an increasing external applied force, more electricity is stored on the electrodes in the form of electrochemical energy. The nonfaradaic and faradaic forces of the two electrodes reach a new equilibrium after the $H^+$ ions and $SO_4^{2-}$ ions are redistributed in the electrolyte and balance the piezoelectric field in the PVDF film. This technology directly converts mechanical energy into electrochemical energy without energy being wasted on the outer circuitry and decreases energy conversion loss. Importantly, the development of both high-performance energy storage devices and the materials used in the devices is essential for the fabrication of highly effective hybridized "all-in-one energy harvesting and storage devices" in the future (Song et al. 2015; Lee et al. 2016).

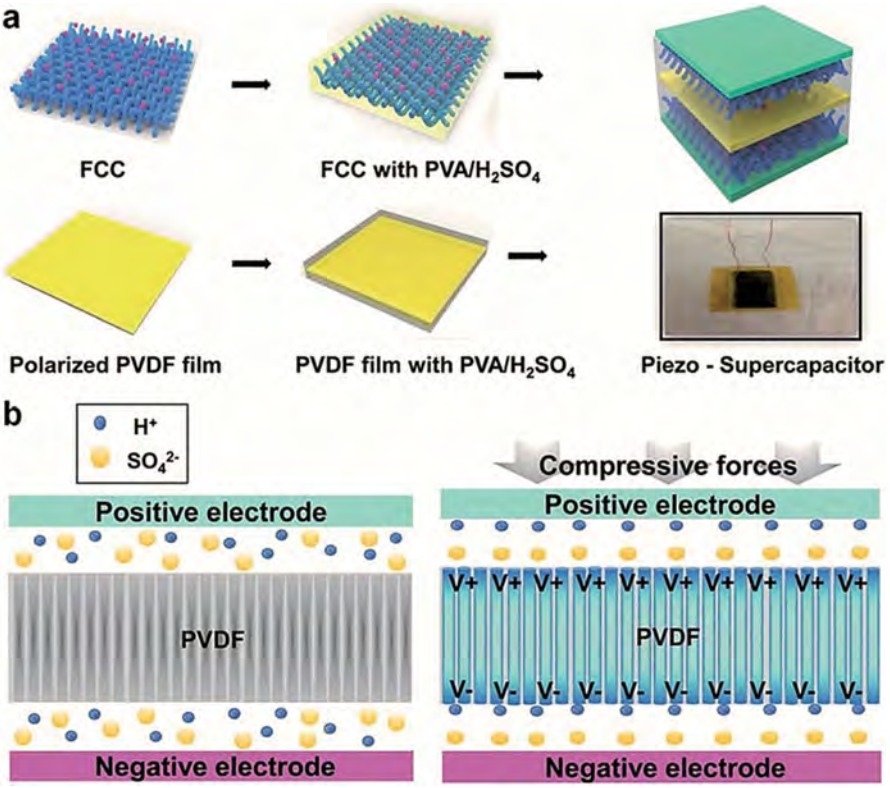


**Fig. 11.48** Integration of energy harvesting and supercapacitor (Modified with permission from Song et al. (2015) (Royal Society of Chemistry)): (**a**) Schematic illustration of the process flow of hybrid piezosupercapacitor fabrication, and (**b**) proposed working mechanism of the hybrid piezo-supercapacitor

**INDEPTH: Nanogenerator-Driven Self-Powered Systems**

As human beings are seeking for intelligent life, devices with high functionality are the fundamental components. A bottleneck for the sustainable operation of these devices is the electric power, although the power level for each is small but the number of units can be huge. Searching for a self-powered system is a major drive in the field of nanoenergy. For example, TENG has been an exciting technology because of its high performance, high efficiency, low cost, easy fabrication, diverse choices of materials, and easy scalability. TENG can also be a high-sensitive self-powered sensor for detecting mechanical triggering, stimulation, and movement. The electric current and voltage signals generated by TENG represent the dynamic and static information, respectively, regarding a mechanical action. Such a sensor tip does not need

(continued)

a power to drive it, which is a major difference in comparison to conventional sensors. Applications can be found in areas of microelectromechanical systems, human–machine interfacing, touch-pad technology, security systems, and motion sensing. Therefore, integrating the TENG and the similar nanogenerators with a sensor to form a self-powered system considering the practical environment in which the system will be employed. The following "tree" idea regarding the development of nanogenerators starts from fundamental materials and physics effects, tiny mechanical energy can be effectively converted into electricity using nanogenerators, which can be a fundamental approach for intelligent earth with applications in internet of things, mobile/wearable electronics, fabric electronics, environmental protection, healthcare, infrastructure monitoring, and national security (Wang et al. 2015a, b).

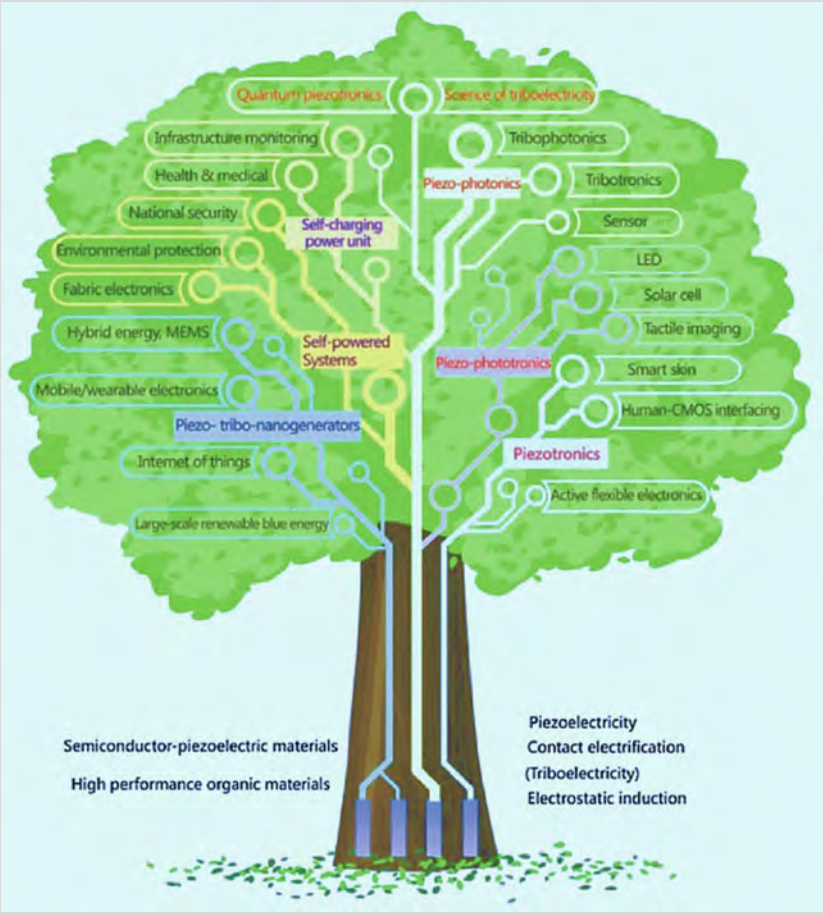

## Exercises

### Part I: General Questions

11.1. Define the energy-harvesting (also known as power harvesting or energy scavenging or ambient power) concept and take an example to explain a generic energy system.
11.2. Address thermoelectric materials characterizations, types, and main applications.
11.3. How to distinguish oxide and ceramic thermoelectric materials? Address their structure characterization and application differences.
11.4. Explain piezoelectric effect, and list piezoelectric materials types and their applications for energy harvesting.
11.5. Explain pyroelectric effect, and list pyroelectric materials types and their applications for energy harvesting.
11.6. List magnetostrictive and multiferroic magnetoelectric materials, and explain their differences and applications for energy harvesting.
11.7. Explain triboelectric effect, and list triboelectric materials types and their applications for energy harvesting.
11.8. Address principle of triboelectric nanogenerators, and list their types and applications.

### Part II: Through-Provoking Questions

11.9. List types of hybrid energy harvesters, and their status and future trends.
11.10. Explain piezotronic and piezophototronic effects and their differences, and address their applications for energy harvesting.
11.11. Describe the scope of piezotronics and piezophototronics, and explain their differences. How do they inspire novel device applications?
11.12. Give examples to explain integration of energy harvesting and storage devices.

## References

Ahn, C.-W., Maurya, D., Park, C.-S., Nahm, S., Priya, S.: A generalized rule for large piezoelectric response in perovskite oxide ceramics and its application for design of lead-free compositions. J. Appl. Phys. **105**, 114108 (2009)

Andrew, J.S., Starr, J.D., Budi, M.A.K.: Prospects for nanostructured multiferroic composite materials. Scripta Mater. **74**, 38–43 (2014)

Andosca, R.A., McDonald, T.G., Genova, V., Rosenberg, S., Keating, J., Benedixen, C., Wu, J.: Experimental and theoretical studies on mems piezoelectric vibrational energy harvesters with mass loading. Sens. Actuat. A: Phys. **178**, 76–87 (2012)

Apo, D.J.: Low frequency microscale energy harvesting. Ph.D. Disseration. Virginia Tech, Blacksburg (2014)

Aswal, D.K., Basu, R., Singh, A.: Key issues in development of thermoelectric power generators: high figure-of-merit materials and their highly conducting interfaces with metallic interconnects. Energy Convers. Manag. **114**, 50–67 (2016)

Bae, J., Lee, J., Kim, S., Ha, J., Lee, B.-S., Park, Y., Choong, C., Kim, J.-B., Wang, Z.L., Kim, H.-Y., Park, J.-J., UI, C.: Flutter-driven triboelectrification for harvesting wind energy. Nat. Commun. **5**, 4929 (2014)

Biswas, K., He, J., Zhang, Q., Wang, G., Uher, C., Dravid, V.P., Kanatzidis, M.G.: Strained endotaxial nanostructure with high thermoelectric figure of merit. Nat. Chem. **3**(2), 160–166 (2011)

Bowen, C.R., Taylor, J., LeBoulbar, E., Zabek, D., Chauhanc, A., Vaishc, R.: Pyroelectric materials and devices for energy harvesting applications. Energy Environ. Sci. **7**, 3836–3856 (2014)

Bykhovski A., Kaminski V., Shur M., Chen Q., Khan M.: Pyroelectricity in gallium nitride thin films. Appl. Phys. Lett. **69**, 3254–3256 (1996)

Casian, A.I., Sanduleac, I.I.: Organic thermoelectric materials: new opportunities. J. Thermoelectr. **3**, 11–20 (2013)

Chen, J., Zhu, G., Yang, J., Jing, Q., Bai, P., Yang, W., Qi, X., Su, Y., Wang, Z.L.: Personalized keystroke dynamics for self-powered human–machine interfacing. ACS Nano. **9**, 105–116 (2015)

Dagdeviren, C., Joe, P., Tuzmanc, O.L., Park, K.-I., Lee, K.J., Shi, Y., Huangh, Y., Rogers, J.A.: Recent progress in flexible and stretchable piezoelectric devices for mechanical energy harvesting, sensing and actuation. Extr. Mechan. Lett. **9**, 269–281 (2016)

Deterre, M., Lefeuvre, E., Zhu, Y., Woytasik, M., Bosseboeuf, A., Boutaud, B., Dal Molin, R.: Micromachined piezoelectric spirals and ultra-compliant packaging for blood pressure energy harvesters powering medical implants. IEEE 26th International Conference on Micro Electro Mechanical Systems (MEMS), pp. 249–252. IEEE, New York (2013)

Dineva, P.S., Cross, D., Müller, R., Rangelov, T.: Dynamic fracture of piezoelectric materials-solid mechanics and its applications, pp. 7–32. Springer International Publishing, Switzerland (2014)

Elsheikh, M.H., et al.: A review on thermoelectric renewable energy: principle parameters that affect their performance. Renew. Sust. Energ. Rev. **30**, 337–355 (2014)

Falconi, C., Mantini, G., D'Amico, A., Ferrari, V.: Modeling of piezoelectric nanodevices. In: Piezoelectric nanomaterials for biomedical applications. In: Ciofani, G., Menciassi, A. (eds.) Nanomedicine and nanotoxicology, pp. 93–133. Springer, Berlin, Germany (2012)

Fang, C., Jiao, J., Ma, J., Lin, D., Xu, H., Zhao, X., Luo, H.: Significant reduction of equivalent magnetic noise by in-plane series connection in magnetoelectric Metglas/Mn-doped Pb (Mg1/3Nb2/3)O3-PbTiO3 laminate composites. J. Phys. D: Appl. Phy. **48**, 465002 (2015)

Geuther, J. A., Danon, Y.: Electron and positive ion acceleration with pyroelectric crystals. Journal of Applied Physics **97**, 074109 (2005)

Gillette, S.M., Fitchorov, T., Obi, O., Jiang, L., Hao, H., Wu, S., Chen, Y., Harris, V.G.: Effects of intrinsic magnetostriction on tube-topology magnetoelectric sensors with high magnetic field sensitivity. J. Appl. Phys. **115**, 17C734 (2014)

Guduru, R., Liang, P., Runowicz, C., Nair, M., Atluri, V., Khizroev, S.: Magneto-electric nanoparticles to enable field-controlled high-specificity drug delivery to eradicate ovarian cancer cells. Sci. Rep. **3**, 2953 (2013)

Hajati, A., Kim, S.-G.: Ultra-wide bandwidth piezoelectric energy harvesting. Appl. Phys. Lett. **99**, 083105 (2011)

Han, G., Ryu, J., Yoon, W.-H., Choi, J.-J., Hahn, B.D., Kim, J.-W., Park, D.-S., Ahn, C.-W., Priya, S., Jeong, D.-Y.: Stress-controlled $Pb(Zr_{0.52}Ti_{0.48})O_3$ thick films by thermal expansion mismatch between substrate and $Pb(Zr_{0.52}Ti_{0.48})O_3$ film. J. Appl. Phys. **110**, 124101 (2011)

He, J., Liu, Y., Funahashi, R.: Oxide thermoelectrics: the challenges, progress, and outlook. J. Mater. Res. **26**(15), 1762–1772 (2011)

Hossain, M.S., Al-Dirini, F., Hossain, F.M., Skafidas, E.: High performance graphene nano-ribbon thermoelectric devices by incorporation and dimensional tuning of nanopores. Sci. Rep. **5**, 11297 (2015)

Hunter, S.R., Lavrik, N.V., Bannuru, T., Mostafa, S., Rajic, S., Datskos, P.G.: Development of MEMS based pyroelectric thermal energy harvesters. Proc. SPIE. **8035**, 80350V (2011)

Jagadish, C., Pearton, S.J.: Zinc oxide bulk, thin films and nanostructures: processing, properties, and applications. Elsevier, Amsterdam (2011)

Jenkins, K., Nguyen, V., Zhu, R., Yang, R.: Piezotronic effect: an emerging mechanism for sensing applications. Sensors. **15**, 22914–22940 (2015)

Joshi, G., et al.: Enhanced thermoelectric figure-of-merit in nanostructured p-type silicon germanium bulk alloys. Nano Lett. **8**, 4670 (2008)

Kargol, A., Malkinski, L., Caruntu, G.: Biomedical applications of multiferroic nanoparticles. In: Malkinski, L. (ed.) Advanced magnetic materials, pp. 89–118. InTech, Rijeka, Croatia (2012)

Kim, S.-G., Priya, S., Kanno, I.: Piezoelectric MEMS for energy harvesting. MRS Bull. **37**(11), 1039–1050 (2012)

Koumoto, K., et al.: Thermoelectric ceramics for energy harvesting. J. Am. Ceram. Soc. **96**, 1–23 (2013)

Lang, S.B.: Pyroelectricity: from ancient curiosity to modern imaging tool. Phys. Today. **58**, 31–36 (2005)

Lee, M., Yang, R., Li, C., Wang, Z.L.: Nanowire−quantum dot hybridized cell for harvesting sound and solar energies. J. Phys. Chem. Lett. **1**, 2929–2935 (2010)

Lee, J.H., Lee, K.Y., Gupta, M.K., Kim, T.Y., Lee, D.Y., Oh, J., Ryu, C., Yoo, W.J., Kang, C.Y., Yoon, S.J., Yoo, J.B., Kim, S.W.: Highly stretchable piezoelectric-pyroelectric hybrid nanogenerator. Adv. Mater. **26**, 765–769 (2014)

Lee, J., Kim, J., Kim, T., Hossain, M.A., Kim, S., Kim, J.: All-in-one energy harvesting and storage devices. J. Mater. Chem. A. **4**(21), 7983–7999 (2016)

Leonov, V.: Energy harvesting for self-powered wearable devices. In: Bonfiglio, A., De Rossi, D. (eds.) Wearable monitoring systems. Springer, New York (2011)

Lin, Z.-H., Cheng, G., Lin, L., Lee, S., Wang, Z.L.: Angew. Chem. Int. Ed. **125**, 12777–12781 (2013)

Lin, Z., Chen, J., Yang, J.: Recent progress in triboelectric nanogenerators as a renewable and sustainable power source. J. Nanomater. **2016**, 5651613 (2016)

Lingam, D., Parikha, A.R., Huanga, J., Jainb, A., Minary-Jolandana, M.: Nano/microscale pyroelectric energy harvesting: challenges and opportunities. Int. J. Smart. Nano Mater. **4**(4), 229–245 (2013)

Morimoto, K., Kanno, I., Wasa, K., Kotera, H.: High-efficiency piezoelectric energy harvesters of c-axis-oriented epitaxial PZT films transferred onto stainless steel cantilevers. Sens. Actuat. A: Phys. **163**, 428–432 (2010)

Music, D., Geyer, R.W., Hans, M.: High-throughput exploration of thermoelectric and mechanical properties of amorphous $NbO_2$ with transition metal additions. J. Appl. Phys. **120**, 045104 (2016)

Narita, F., Fox, M.: A review on piezoelectric, magnetostrictive, and magnetoelectric materials and device technologies for energy harvesting applications. Adv. Eng. Mater. **20**(5), 1700743 (1–22) (2018)

Newnham, R.E.: Properties of materials: anisotropy, symmetry, structure. Oxford University Press, Oxford (2005)

Palneedi, H., Annapureddy, V., Priya, S., Ryu, J.: Status and perspectives of multiferroic magnetoelectric composite materials and applications. Actuators **5**(1), 9 (2016)

Paluszek, M., Avirovik, D., Zhou, Y., Kundu, S., Chopra, A., Montague, R., Priya, S.: Magnetoelectric composites for medical application. In: Srinivasan, G., Priya, S., Sun, N.X. (eds.) Composite magnetoelectrics, pp. 297–327. Woodhead Publishing, Cambridge, UK (2015)

Park, K.-I., Son, J.H., Hwang, G.-T., Jeong, C.K., Ryu, J., Koo, M., Choi, I., Lee, S.H., Byun, M., Wang, Z.L., Lee, K.J.: Highly-efficient, flexible piezoelectric PZT thin film nanogenerator on plastic substrates. Adv. Mater. **26**(16), 2514–2520 (2014)

Park, T., Na, J., Kim, B., Kim, Y., Shin, H., Kim, E.: Photothermally activated pyroelectric polymer films for harvesting of solar heat with a hybrid energy cell structure. ACS Nano. **9**(12), 11830–11839 (2015)

Pillatsch, P.: Piezoelectric energy harvesting from low frequency and random excitation using frequency up-conversion. Ph.D. thesis. Imperial College, London (2013)

Priya, S., Song, H.-C., Zhou, Y., Varghese, R., Chopra, A., Kim, S.-G., Kanno, I., Wu, L., Ha, D.S., Ryu, J., Polcawich, R.G.: A review on piezoelectric energy harvesting: materials, methods, and circuits. Energ Harvest Syst. **4**(1), 3–39 (2017)

Qi, Y., Kim, J., Nguyen, T.D., Lisko, B., Purohit, P.K., McAlpine, M.C.: Enhanced piezoelectricity and stretchability in energy harvesting devices fabricated from buckled PZT ribbons. Nano Lett. **11**(3), 1331–1336 (2011)

Radousky, H.B., Liang, H.: Energy harvesting—an integrated view of materials, devices and applications. Nanotechnology. **23**(50), 502001 (2012)

Rowe, D.M.: Thermoelectrics handbook: macro to nano. CRC Press, Boca Raton, FL (2005). ISBN 978-1-4200-3890-3

Ryu, J., Kang, J.-E., Zhou, Y., Choi, S.-Y., Yoon, W.-H., Park, D.-S., Choi, J.-J., Hahn, B.-D., Ahn, C.-W., Kim, J.-W., et al.: Ubiquitous magneto-mechano-electric generator. Energy Environ. Sci. **8**, 2402–2408 (2015)

Sahraoui, A.H., Longuemart, S., Dadarlat, D., Delenclos, S., Kolinsky, C., Buisine, J.: Analysis of the photopyroelectric signal for investigating thermal parameters of pyroelectric materials. Rev. Sci. Instrum. **74**, 618–620 (2003)

Shah, Y.T.: Thermal energy: sources, recovery, and applications. CRC Press, Boca Raton, FL (2018)

Shibata, K., Suenaga, K., Watanabe, K., Horikiri, F., Nomoto, A., Mishima, T.: Improvement of piezoelectric properties of (K, Na)$NbO_3$ films deposited by sputtering. Jpn. J. Appl. Phys. **50**, 041503 (2011)

Snyder, J., Toberer, E.S.: Complex thermoelectric materials. Nat. Mater. **7**(2), 105–114 (2008)

Sohn, J.I., Hong, W.-K., Choi, S.S., Coles, H.J., Welland, M.E., Cha, S.N., Kim, J.M.: Emerging applications of liquid crystals based on nanotechnology. Materials. **7**, 2044–2061 (2014)

Song, R., Jin, H., Li, X., Fei, L., Zhao, Y., Huang, H., Chan, H.L.W., Wang, Y., Chai, Y.: A rectification-free piezo-supercapacitor with a polyvinylidene fluoride separator and functionalized carbon cloth electrodes. J. Mater. Chem. A. **3**, 14963–14970 (2015)

Stephan, M., Robert, J., Henry, G., Eckhard, Q., Reinhard, K., Bernhard, W.: MEMS magnetic field sensor based on magnetoelectric composites. J. Micromech. Microeng. **22**, 065024 (2012)

Szczech, J.R., Higginsa, J.M., Jin, S.: Enhancement of the thermoelectric properties in nanoscale and nanostructured materials. J. Mater. Chem. **21**, 4037–4055 (2011)

Ting-Ta, Y., Hirasawa, T., Wright, P., Pisano, A., Liwei, L.: Corrugated aluminum nitride energy harvesters for high energy conversion 26. Effectiveness. J. Micromech. Microeng. **21**, 085037 (2011)

Varghese, R.P.: MEMS technologies for energy harvesting and sensing. Ph.D. Disseration. Virginia Tech, Blacksburg (2013)

Wang, Z.L.: Toward self-powered nanosystems: from nanogenerators to nanopiezotronics. Adv. Funct. Mater. **18**(22), 3553–3567 (2008)

Wang, Z.L.: Piezotronic and piezophototronic effects. J. Phys. Chem. Lett. **1**(9), 1388–1393 (2010)

Wang, Z.L., Zhu, G., Yang, Y., Wang, S., Pan, C.: Progress in nanogenerators for portable electronics. Mater. Today. **15**(12), 532–543 (2012)

Wang, J.-J., Su, H.-J., Hsu, C.-I., Su, Y.-C.: Composite piezoelectric rubber band for energy harvesting from breathing and limb motion. J. Phys. Conf. Ser. **557**, 012022 (2014)

Wang, Z., Pan, X., He, Y., Hu, Y., Gu, H., Wang, Y.: Piezoelectric nanowires in energy harvesting applications. Adv. Mater. Sci. Eng. **2015**, 1–21 (2015a)

Wang, Z.L., Chen, J., Lin, L.: Progress in triboelectric nanogenerators as a new energy technology and self-powered sensors. Energy Environ. Sci. **8**, 2250–2282 (2015b)

Whatmore, R.: Pyroelectric devices and materials. Rep. Prog. Phys. **49**, 1335 (1986)

Wooldridge, J., Blackburn, J.F., McCartney, N.L., Stewart, M., Weaver, P., Cain, M.G.: Small scale piezoelectric devices: pyroelectric contributions to the piezoelectric response. J. Appl. Phys. **107**, 104118–104118-6 (2010)

Xu, R.: Energy harvesting for microsystems. Ph.D. dissertation. Technical University of Denmark (DTU), Denmark (2012)

Xu, R., Kim, S.-G.: Low-frequency, low-G MEMS piezoelectric energy harvester. J. Phys. Conf. Ser. **660**, 012013 (2015)

Xu, C., Wang, X., Wang, Z.L.: Nanowire structured hybrid cell for concurrently scavenging solar and mechanical energies. J. Am. Chem. Soc. **131**(16), 5866–5872 (2009)

Xue, X., Wang, S., Guo, W., Zhang, Y., Wang, Z.L.: Hybridizing energy conversion and storage in a mechanical-to-electrochemical process for self-charging power cell. Nano Lett. **12**, 5048–5054 (2012)

Yan, Y., Priya, S.: Multiferroic magnetoelectric composites/hybrids. In: Kim, C.-S., Randow, C., Sano, T. (eds.) Hybrid and hierarchical composite materials, pp. 95–160. Springer International Publishing, Cham, Switzerland (2015)

Yang, Y., Wang, Z.L.: Hybrid energy cells for simultaneously harvesting multi-types of energies. Nano Energy. **14**, 245–256 (2015)

Yang, Y., Guo, W., Pradel, K.C., Zhu, G., Zhou, Y., Zhang, Y., Hu, Y., Lin, L., ZL, W.: Pyroelectric nanogenerators for harvesting thermoelectric energy. Nano Lett. **12**, 2833–2838 (2012a)

Yang, Y., Jung, J.H., Yun, B.K., Zhang, F., Pradel, K.C., Guo, W., Wang, Z.L.: Flexible pyroelectric nanogenerators using a composite structure of lead-free $KNbO_3$ nanowires. Adv. Mater. **24**, 5357–5362 (2012b)

Yang, Y., Zhang, H., Lin, Z.-H., Liu, Y., Chen, J., Lin, Z., Zhou, Y.S., Wong, C.P., Wang, Z.L.: A hybrid energy cell for self-powered water splitting. Energy Environ. Sci. **6**, 2429–2434 (2013)

Yoon, G.C., Shin, K.-S., Gupta, M.K., Lee, K.Y., Lee, J.-H., Wang, Z.L., Kim, S.-W.: High-performance hybrid cell based on an organic photovoltaic device and a direct current piezoelectric nanogenerator. Nano Energy. **12**, 547–555 (2015)

Yu H., Kang B., Park C., Pi U., Lee C., Choi S.-Y.: The fabrication technique and electrical properties of a free-standing GaN nanowire. Appl. Phys. A **81**, 245–247 (2005)

Yue, K., Guduru, R., Hong, J., Liang, P., Nair, M., Khizroev, S.: Magneto-electric nano-particles for non-invasive brain stimulation. PLoS One. **7**, e44040 (2012)

Zhang, X., Zhao, L.D.: Thermoelectric materials: energy conversion between heat and electricity. J. Mater. **1**, 92–105 (2015)

Zhang, Y., Mehta, R.J., Belley, M., Han, L., Ramanath, G., Borca-Tasciuc, T.: Lattice thermal conductivity diminution and high thermoelectric power factor retention in nanoporous macroassemblies of sulfur-doped bismuth telluride nanocrystals. Appl. Phys. Lett. **100**, 1193113 (2012)

Zhou Y., Apo D. J., Priya S.: Dual-phase self-biased magnetoelectric energy harvester. Appl. Phys. Lett. **103**, 192909 (2013)

Zhou, Q., Lau, S., Wu, D., Shung, K.K.: Piezoelectric films for high frequency ultrasonic transducers in biomedical applications. Prog. Mater. Sci. **56**, 139–174 (2011)

Zhou, Y.S., Zhu, G., Niu, S., Liu, Y., Bai, P., Jing, Q., Wang, Z.L.: Nanometer resolution self-powered static and dynamic motion sensor based on micro-grated triboelectrification. Adv. Mater. **26**(11), 1719–1724 (2014)

Zhu, T., Ertekin, E.: Phonon transport on two-dimensional graphene/boron nitride superlattices. Phys. Rev. B. **90**, 195209 (2014)

Zhu, G., Chen, J., Zhang, T., Jing, Q., Wang, Z.L.: Radial-arrayed rotary electrification for high performance triboelectric generator. Nat. Commun. **5**, 3426 (2014)